

#### Department of Physics

Institute of Experimental Physics



#### Accelerator Technology & Applied Physics Division

Berkeley Lab Laser Accelerator

# Development of a reliable platform for Laser-Plasma Accelerator driven Free-Electron Laser studies

Dissertation zur Erlangung des Doktorgrades im Fachbereich Physik an der Fakultät für Mathematik, Informatik und Naturwissenschaften der Universität Hamburg

vorgelegt von

FINN DAVID KOHRELL

Berkeley, October 2, 2025

#### **Betreuer**

Dr. Sam K. Barber

Dr. Jeroen van Tilborg

Prof. Dr. Carl B. Schroeder

Prof. Dr. Florian Grüner

## **Gutachter der Dissertation**

Prof. Dr. Florian Grüner

Prof. Dr. Carl B. Schroeder

## Zusammensetzung der Prüfungskommission

Dr. Jeroen van Tilborg

Prof. Dr. Carl B. Schroeder

Prof. Dr. Florian Grüner

Prof. Dr. Wolfgang Hillert

Prof. Dr. Günter Sigl

## Vorsitzender der Prüfungskommission

Prof. Dr. Günter Sigl

## **Datum der Disputation**

13.10.2025

## Vorsitzender des Fach-Promotionsausschusses PHYSIK

Prof. Dr. Wolfgang J. Parak

## Leiter des Fachbereichs PHYSIK

Prof. Dr. Markus Drescher

## Dekan der Fakultät MIN

Prof. Dr.-Ing. Norbert Ritter

- "The only difference between science and screwing around is writing it down."
- Adam Savage
- "Allzu oft erfreuen wir uns an der Annehmlichkeit der eigenen Meinung, ohne uns der Unannehmlichkeit des Nachdenkens unterzogen zu haben."
- Justus Jonas
- "So I've started out for God knows where, I guess I'll know when I get there."
- Tom Petty and the Heartbreakers
- "Do, or do not. There is no try."
- Master Yoda

# **Abstract**

Free-Electron Lasers (FELs) based on start-of-the-art radio-frequency (RF) accelerator facilities have been established as a reliable source of coherent, high-brightness x-ray beams, advancing and pushing the boundaries of a broad range of scientific applications. Their capabilities would unlock significant improvements to applications in medical imaging and semiconductor manufacturing, among others, but to make this technology available to a larger community, significant steps to reduce the cost and footprint of the accelerator facilities are required.

With the emergence of laser-plasma accelerators (LPAs) as powerful, compact alternatives to RF machines, leveraging these sources to drive FELs immediately arose as a promising application. First results of LPA-driven FEL radiation have been achieved by the community over the last few years, but reliable high-gain FEL operation, required to prove the potential of serving as a capable platform for future light source facilities, has yet to be demonstrated.

This dissertation was carried out at the Hundred TeraWatt Undulator (HTU) system, part of the Berkeley Lab Laser Accelerator (BELLA) group at Lawrence Berkeley National Laboratory (LBNL), and driven by the goal to demonstrate reliable operation of an LPA-driven FEL. The work presented here aims to achieve a more repeatable and stable LPA interaction, to enable a first demonstration of LPA-driven FEL lasing on the HTU system, and to develop an experimental platform for subsequent investigations of the LPA-driven FEL performance.

To achieve this goal, a large part of the work conducted as a part of this thesis project went towards improvements of the diagnostic capabilities of the experiment, to obtain new insights into the key parameters of the LPA interaction. These results were used to inform the need for additional stabilization systems to improve system performance, and their subsequent development, installation, and characterization are discussed as well.

The setup and commissioning of new, as well as the upgrade of existing diagnostics enabled the discovery of systematic instabilities of the laser system. Specifically variations of the laser pulse duration and energy, uncovered as part of this work, were shown to significantly impact the LPA performance. Implementing new stabilization capabilities targeted towards these variations, in combination with extensive efforts to further increase long-term reliability of the LPA interaction, yielded successful demonstration and characterization of LPA-driven FEL lasing at 420 nm. Through subsequent improvements to the laser system and operational procedures, first results exceeding 1000-fold gain from an LPA-driven FEL, with higher than 90% reliability, were achieved. During a dedicated follow-up campaign, continuous operation of the LPA-driven FEL over more than eight hours was demonstrated, while maintaining the performance of more than 90% of all shots exhibiting FEL gain.

These results represent an unprecedented level of both shot-to-shot and long-term stability, as well as overall performance for LPA-driven FELs, and serve as a crucial step towards the demonstration of the technology as a viable platform for future compact FEL facilities.



# Zusammenfassung

Freie Elektronen Laser (FELs) basierend auf klassischen Radio Frequenz (RF) Beschleunigern haben sich als verlässliche Quellen für kohärente Röntgenstrahlung mit hoher Intensität etabliert, und die Grenzen einer Vielzahl von wissenschaftlichen Anwendungen erweitert. Diese Technologie birgt grosses Potential für die Verbesserung von, unter anderem, bildgebenden Verfahren für medizinische Anwendungen und die Herstellung von Halbleiterchips. Aber um diese Lichtquellen einem breiteren Publikum zugänglich zu machen sind eine signifikante Reduzierung der Grösse und Kosten der Beschleuniger notwendig.

Mit dem Aufkommen von Laser-Plasma Beschleunigern (LPAs) als kraftvolle und kompakte Alternative zu RF Maschinen, erregte ihre potentielle Anwendung als Quellen für den Betrieb von FELs sofort Aufmerksamkeit. Erste LPA-FEL Ergebnisse wurden in den letzten Jahren erfolgreich von der wissenschaftlichen Gemeinschaft demonstriert. Verlässlicher Betrieb eines FELs mit hoher Signalstärke wurde noch nicht erreicht, repräsentiert jedoch einen kritischen Schritt um das Potential der Technologie zu bestätigen.

Diese Dissertation wurde am Hundred TeraWatt Undulator (HTU) Experiment durchgeführt, welches ein Teil der Berkeley Lab Laser Accelerator (BELLA) Gruppe am Lawrence Berkeley National Laboratory (LBNL) ist, mit dem Ziel den stabilen Betrieb eines FELs mit einer LPA Quelle zu demonstrieren. Die hier präsentierte Arbeit zielte drauf ab, eine stabilere und reproduzierbarere LPA Interaktion zu erreichen, um zum ersten Mal LPA betriebene FEL Strahlung am HTU Experiment zu generieren und eine Plattform für nachfolgende Studien der Leistung des LPA-FEL Systems zu erstellen.

Um dieses Ziel zu erreichen fokussiert sich ein Grossteil der präsentierten Experimente auf die Verbesserung der experimentellen Diagnostiken, um neue Einblicke in die kritischen Parameter des LPA Prozesses zu ermöglichen. Diese Ergebnisse wurden wiederum genutzt, um die Notwendigkeit für weitere Systeme zur Stabilisierung des HTU Experiments zu untersuchen, deren Installation und Charakterisierung ebenfalls im Folgenden beschrieben werden.

Sowohl der Aufbau und die Inbetriebnahme neuer, als auch die Verbesserung existierender Diagnostiken, ermöglichte die Entdeckung systematischer Instabilitäten des Laser Systems. Insbesondere Variationen der Laser Puls Dauer und Energie, die im Rahmen der Arbeit an dieser Dissertation gefunden wurden, zeigen nachweislich einen grossen Einfluss auf den LPA Prozess. Gezielte Stabilisation jener Variationen, kombiniert mit umfangreichen Massnahmen um die Langzeit Stabilität der LPA Interaktion zu verbessern, ermöglichte die erfolgreiche Demonstration und Charakterisierung von 420 nm FEL Strahlung. Durch nachfolgende Optimierungen des Laser Systems und der Prozesse zum Betrieb des Beschleunigers, wurden zum ersten Mal mehr als tausendfache Verstärkung eines LPA-FEL Signals gezeigt, mit einer Verlässlichkeit von mehr als 90%. Eine nachfolgende Kampagne konnte dieses Level an Stabilität reproduzieren, über einen Zeitraum von mehr als acht Stunden.

Die Ergebnisse die im Rahmen dieser Dissertation erreicht wurden, repräsentieren eine nicht zuvor gezeigte Stabilität und allgemeine Leistung für LPA-betriebene FELs. Sie zeigen somit

einen kritischen Fortschritt um diese Technologie als geeignete Plattform für zukünftige kompakte FELs zu etablieren.

# **List of Publications**

Some of the work conducted for and described in the scope of this thesis has been published either as first- or co-authored articles.

The first part of this dissertation, focused on the description of the HTU system, and important improvements to its diagnostic and stabilization capabilities, are referenced in the three supporting publications listed below. The second part, which discusses the resulting demonstrations of LPA-driven FEL gain and long-term performance and forms the backbone of the results, is represented in the two core publications.

#### Core publications:

- F. Kohrell, S. K. Barber, C. E. Doss, K. Jensen, S. Schröder, C. Berger, Z. Eisentraut, K. Nakamura, A. J. Gonsalves, F. Isono, G. R. Plateau, R. A. van Mourik, M. Gracia-Linares, L. Labun, B. M. Hegelich, S. V. Milton, C. G. R. Geddes, J. Osterhoff, C. B. Schroeder, F. Grüner and J. van Tilborg, Over 8 hours of continuous operation of a free-electron laser driven by a laser-plasma accelerator, Phys. Rev. Accel. Beams in review
- S. K. Barber, F. Kohrell, C. Doss., K. Jensen, C. Berger, F. Isono, Z. Eisentraut, S. Schröder, A. J. Gonsalves, K. Nakamura, G. R. Plateau, R. A. van Mourik, M. Gracia-Linares, L. Labun, B. M. Hegelich, S. V. Milton, C. G. R. Geddes, J. Osterhoff, C. B. Schroeder, E. H. Esarey and J. van Tilborg, Greater than 1000-fold gain in a free-electron laser driven by a laser plasma accelerator with >90% reliability, Phys. Rev. Lett. 135, 055001 (2025)

#### Supporting publications:

- F. Kohrell, S. K. Barber, K. Jensen, C. Doss, C. Berger, C. B. Schroeder, E. H. Esarey, F. Grüner and J. van Tilborg, *Investigation of correlations between spectral phase fluctuations of the laser pulse and the performance of an LPA*, Nucl. Instrum. Methods Phys. Res., A 1073 (2025)
- F. Kohrell, S. K. Barber, K. Jensen, C. Berger, C. B. Schroeder, E. H. Esarey and J. van Tilborg, Optimizing Down-Ramp Injection to Generate Stable and Tunable Electron Bunches for an LPA Driven FEL, 2022 IEEE Advanced Accelerator Concepts Workshop (AAC), Long Island, NY, USA, 2022, pp. 1-4
- K. Jensen, S. K. Barber, C. Berger, C. Doss, **F. Kohrell**, S. Coleman, N. Cook, J. Edelen, J. Einstein-Curtis, and J. van Tilborg, *Improved laser-plasma accelerator stability via high-bandwidth longitudinal focal position stabilization of 100 TW-class laser system*, Phys. Rev. Accel. Beams in review



# **Contents**

1	Las	Laser-Plasma Acceleration of Electrons 1					
	1.1	Motivation					
	1.2	Method					
		1.2.1 Excitation of Plasma Waves					
		1.2.2 Electron Injection					
		1.2.3 Laser-Plasma Interaction					
	1.3	Physics of ultra-short, high-Intensity Laser Pulses					
		1.3.1 Creation of bandwidth-limited Pulses					
		1.3.2 Measurement of Pulse Properties					
<b>2</b>	Dyr	namics of Electron Beams					
	2.1	Properties of Electron Bunches					
	2.2	Magnetic Chicane					
3	Free	e-Electron Lasers 13					
	3.1	Overview					
	3.2	Fundamentals					
		3.2.1 Undulator Radiation					
		3.2.2 FEL Lasing and the SASE Regime					
4	The	e Hundred TeraWatt Undulator System 18					
	4.1	Laser System					
	4.2	Gas Jet Target and Electron Beamline					
	4.3	VISA Undulator					
5	Dev	velopment of Diagnostic Capabilities 26					
•	5.1	Magnetic Spectrometer					
	-	5.1.1 Longitudinal FoV Dependence					
		5.1.2 Camera Sensitivity					
		5.1.3 Longitudinal Sensitivity					
		5.1.4 Radial Sensitivity (Vignetting)					
		5.1.5 Full Calibration					
		5.1.6 Setup and Installation					
	5.2	On-shot, non-invasive Pulse Duration Diagnostic					
		5.2.1 Design					
		5.2.2 Setup					
		5.2.3 Commissioning					
		5.2.4 First Results					
		5.2.5 Linear Chirp Retrieval and Characterization					
		5.2.6 Correlation of Linear Chirp to LPA Parameters					
		5.2.7 Investigation of spectral effects					
	5.3	Undulator Radiation Diagnostics					
	-	5.3.1 UV Spectrometer					
		5 3 2 Emittance Spoiler 50					

## **Contents**

6	Effo	orts to stabilize the LPA Interaction	60		
	6.1	Laser Pulse Energy	60		
		6.1.1 Motivation	60		
		6.1.2 Stabilization System Setup	60		
		6.1.3 Results	62		
	6.2	Pulse Duration	65		
		6.2.1 Investigating the Source of the Instabilities			
		6.2.2 Summary			
	6.3	Combined Pulse Energy and Duration Stabilization Study			
		6.3.1 Results			
	6.4	Wavefront Stabilization			
		6.4.1 Motivation	75		
		6.4.2 Setup			
		6.4.3 Results			
	6.5	Summary			
7	Pro	gress towards reliable LPA-driven FEL Operation	<b>7</b> 9		
	7.1	First undulator radiation observed	79		
	7.2	Crucial Increase of Laser System Performance	81		
		7.2.1 Laser Front End Operation	81		
		7.2.2 Laser Alignment and Active Stabilization	81		
		7.2.3 Improvements of Laser Beam Quality	83		
	7.3	Confirmation of improved Electron Beam Stability and "Turn-Key" LPA Perfor-			
		mance	85		
	7.4	Demonstration of reliable, high-gain FEL operation	87		
		7.4.1 Experimental Conditions	87		
		7.4.2 Analysis of Gain Length	88		
		7.4.3 – Statistical Analysis of Electron Bunch and FEL Radiation Parameters	90		
	7.5	Stable, long-term operation of an LPA-driven FEL	93		
		7.5.1 Experimental Configuration	93		
		7.5.2 Results of Long-term Stability Campaign	94		
		7.5.3 Study of Parameter Correlations	97		
0	C		100		
8	Sun	nmary	102		
9	Out	clook	104		
A	knov	wledgment	105		
Li	st of	Acronyms	106		
Re	efere	nces	107		
10	Apr	pendix	115		
10	**				
10.1 GRENOUILLE Diagnostic: Linear Chirp Retrieval					
		athly Reports (for BELLA - TAU Systems Inc. CRADA)			
	MIOI	temy response (for DEDEAT - 1710 bystems me. ORADA)	199		
Ei	dessi	tattliche Erklärung / Declaration on Oath	135		

## 1.1 Motivation

Since Wolfgang Röntgens discovery of x-rays from the interaction of electrons with a solid anode target in 1895 [1], particle accelerators and light sources based on them have been at the forefront of medical imaging applications and fundamental scientific progress. The awarding of the very first Nobel Prize in Physics for his discovery foreshadowed the crucial impact these concepts have had on many aspects of modern science, which reached their full potential with the development of the first modern particle accelerator, the cyclotron, by Ernest O. Lawrence in 1932 at Berkeley [2]. Since then, an estimated 28% of all discoveries awarded with Nobel Prizes in Physics were enabled by particle accelerators [3].

Modern accelerator-based light source facilities, like the Advanced Light Source (ALS) at Lawrence Berkeley National Laboratory, the Linac Coherent Light Source (LCLS) at the Stanford Linear Accelerator (SLAC), and the European X-Ray Free-Electron Laser (Eu-XFEL) at the Deutsches Elektronen-Synchrotron (DESY) in Hamburg, represent the pinnacle of current technology in providing the brightest and highest quality x-rays to users from the global scientific community, and have made countless contributions to the progress of modern science.

These machines rely on conventional accelerator technology, the large electric fields necessary to accelerate the charged particles are created in radio-frequency (RF) cavities. The maximum field strengths achievable in such structures is fundamentally limited by material breakdown when exceeding about  $100\,\mathrm{MeV/m}$  [4], which in turn dictates the necessity for increased size of accelerator facilities when pushing for higher particle energies. With the above mentioned examples already in the hundreds of meters to kilometer scale, and building costs exceeding the billion dollar mark, alternative technologies for particle accelerators are becoming crucial to drive the next generation of light sources and colliders.

Laser-Plasma Accelerators (LPAs), first proposed by Tajima and Dawson in 1979 [5], utilize the orders of magnitude higher electric field strengths sustainable in electron-plasma waves. Driven by ultra-short, high-intensity laser pulses, these plasma waves have the potential to accelerate an injected electron bunch to hundreds of MeV, and even GeV energies, on millimeter to centimeter scales. This concept promised drastic reductions in size and cost of future accelerator facilities based on the LPA process, compared to conventional RF technology. Since then, many milestones of establishing LPAs as a compact and powerful source of electron bunches of high energy and quality have been achieved by the scientific community. From demonstrations of measuring electron bunches with durations in the femtosecond regime [6], hundreds of pico-Coulomb of charge [7], low emittance [8] and energy spread [9], as well as high long-term stability [10], to multi-GeV peak energies [11, 12], the field has seen rapid improvements in the capabilities of LPA systems over the last decade. This rapid growth, especially the improvements in beam quality, have led to the proposal [13, 14], and successful first demonstration of an LPA-driven undulator source [15], followed by free-electron lasing from an LPA source in the SASE [16] and seeded [17] operation. However, due to the strong coupling between the laser and plasma parameters, and the inherent instability of plasmas and optical high power laser systems, further efforts to improve and stabilize the LPA interaction are needed to demonstrate LPA-driven FELs as a competitive light sources technology.

## 1.2 Method

In this chapter, a brief overview of the fundamental concepts of laser-driven plasma acceleration (LPA) of electrons necessary to understand the work presented in this thesis will be given. A more detailed review, conducted by Esarey, Schroeder, and Leemans, can be found in Ref.[18].

#### 1.2.1 Excitation of Plasma Waves

On microscopic length scales, plasmas can support electric fields far exceeding the limits of solid materials used in RF cavities of classical accelerators. Driven by a disturbance of the charge equilibrium through separation of electrons from the positive ions, the restoring electrostatic forces cause an oscillation of the electrons around their initial position. This behavior can be described as an electron-plasma wave with the characteristic frequency

$$\omega_p = \sqrt{\frac{4\pi n_0 e^2}{m_e}} \tag{1.1}$$

which is defined only by the electron plasma density  $n_0$ . e and  $m_e$  are the electron charge and rest mass, respectively.

The maximum field strength achievable in this case of oscillating charge distribution can be estimated by the non-relativistic cold wave-breaking field

$$E_0 = \frac{\omega_p m_e c}{e} \propto \sqrt{n_0} \tag{1.2}$$

with c the speed of light. Evaluating this expression leads to

$$E_0[V/m] \simeq 96\sqrt{n_0[1/cm^3]}$$
 (1.3)

which, for an exemplary electron plasma density of  $n_0 = 10^{18} {\rm cm}^{-3}$ , returns a peak field strength of  $E_0 \simeq 96 \, {\rm GeV}$ . This represents an increase over the previously described limit of accelerating field strengths of classical RF accelerators by about three orders of magnitude.

Crucial to excite electron-plasma waves supporting such powerful fields is using an external driver of similar longitudinal and transverse scale. The characteristic length of the plasma wave is given by

$$\lambda_p = \frac{2\pi c}{\omega_p} \propto \frac{1}{\sqrt{n_0}} \tag{1.4}$$

which, for the case of  $n_0 = 10^{18} {\rm cm}^{-3}$  discussed above, yields  $\lambda_p \simeq 33 \, \mu {\rm m}$  and corresponds to a timescale  $\tau_p$  of less than 100 fs. This defines the limit for the width and length of the wave driver and the accelerated electron bunch, which have to be on the order of  $\frac{\lambda_p}{2}$  for most efficient acceleration.

Although the oscillation of charge carriers in the electron-plasma wave supports the exceptionally high field strengths necessary to realize this compact, novel acceleration scheme, the electrons in the plasma wave itself are not experiencing any net gain in average longitudinal momentum. The wave only represents an oscillation around the rest position, and no mass transport. To achieve net acceleration, particles need to be injected into the wave field (also referred to as the "wakefield").

## 1.2.2 Electron Injection

Plasma waves have the potential to create ultra-short electron bunches and accelerate them to hundreds of MeV over just millimeter-scale acceleration distances. However, a high degree of stability, quality, and tunability of the electron bunches is required for using plasma-based accelerators to drive light sources like free-electron lasers (FELs). [19]

Trapping electrons directly from the particles sustaining the plasma wave allows for the most simple and compact experimental setups, and an effective way to do so is by decreasing the plasma density over the propagation distance z. Such a density gradient  $\frac{dn_0}{dz} < 0$  is often referred to as a "density down-ramp" [20–22]. This technique will be discussed here in more detail, because it is employed on the HTU system and used for all experiments described in this work. Other common injection schemes are introduced and explained by Esarey at al. in Ref.[18].

Because the plasma wavelength  $\lambda_p$  scales inversely with the electron plasma density  $n_0$ , as described in Eq.1.4, a decrease in plasma density will cause the plasma wavelength to increase. This leads to a decrease in the local phase velocity of the plasma wave, and the wave slowing down lowers the threshold for electrons to be trapped and subsequently accelerated at the back of the wave.

Injecting electrons over a long distance (trapping length  $L_{tr} \gg \lambda_p$ ) creates beams with high energy spread. But density gradients on the order of  $L_{tr} \leq \lambda_p$  allow for near instantaneous trapping of the electrons at the peak of the electron density wave. Localized to a small region of the plasma wave with nearly the same phase, they all experience the same accelerating field. This allows for the generation of quasi-monoenergetic, low energy spread and emittance electron bunches. [18, 19, 22–24]

Such sharp density transitions on the scale of the plasma wavelength and the ability to generate high-quality electron beams from this technique have been demonstrated by placing a razor blade above a supersonic gas jet, creating a high density shock in the plasma profile. [19, 25]

#### 1.2.3 Laser-Plasma Interaction

Plasma waves with the characteristics described in the previous chapters can be driven by the strong, non-linear electric fields of high-intensity laser pulses. When interacting with a plasma, the laser pulse enacts a force on the charged particles based on the gradient of its electric field distribution  $\mathbf{E}$ .

The so-called "Ponderomotive Force"

$$F_p = -\frac{e^2}{4m_e\omega_L^2} \vec{\nabla} \mathbf{E}^2 \tag{1.5}$$

expels the electrons from the regions of high laser intensity, while the ions, due to their  $> 2000 \times$  higher mass, remain stationary on the relevant timescales. Here,  $\omega_L$  represents the laser frequency.

This creates the charge separation necessary to drive the strong fields in the plasma wave (Eq.1.2), as the displaced electrons are being pulled back by the ion background co-propagating with the laser pulse. They overshoot and start oscillating around their equilibrium position with the frequency  $\omega_p$  and the characteristic length of the formed, laser-driven plasma wave  $\lambda_p$ .

A key parameter to quantify if the instantaneous electric field of a laser pulse is strong enough to drive a plasma wave capable of accelerating electrons to relativistic speeds is the laser strength parameter  $a_0$ . It is defined as the peak amplitude of the laser fields normalized vector potential

$$\mathbf{a} = \frac{e\mathbf{A}}{m_e c^2} \tag{1.6}$$

and for a broad pulse  $(k_L w_L \gg 1)$ , with  $k_L = \frac{\omega_L}{c}$  the wave vector and  $w_L$  the beam radius, the quiver momentum of a plasma electron is given by the vector potential of the laser field  $\mathbf{a} = \mathbf{p}_{\perp}/m_e c$ . For the motion of the electrons in the plasma wave to become relativistic, it can immediately be seen that the laser pulse needs to fulfill the condition  $a_0 \geq 1$ .

For a linearly polarized Gaussian laser pulse,  $a_0$  can be expressed as a function of the laser wavelength  $\lambda_L$  and peak intensity  $I_0$  as follows

$$a_0^2 \simeq 7.3 \cdot 10^{-19} (\lambda_L [\mu \text{m}])^2 \cdot I_0 [\text{W/cm}^2]$$
 (1.7)

## 1.3 Physics of ultra-short, high-Intensity Laser Pulses

This section will give a short overview of the fundamental requirements to generate and characterize laser pulses capable of driving plasma waves for electron acceleration. An extensive overview of the entire field of laser physics and optics was written by Träger [26], and a detailed review specifically of ultra-short laser pulses was conducted by Kryukov [27].

Using the value for the electron plasma density from Sec.1.2 of  $n_0 = 10^{18} {\rm cm}^{-3}$ , a laser pulse duration on the order of  $\tau_L \simeq 50 \, {\rm fs}$  is required to resonantly drive the plasma wave (see Sec.1.2.1).

Furthermore, fulfilling the condition of  $a_0 \ge 1$  to accelerate electrons to relativistic speeds (Sec.1.2.3) requires a peak laser intensity of  $I_0 \ge 2.14 \cdot 10^{18} \text{W/cm}^2$  (using Eq.1.7), assuming the use of an  $\lambda_L = 800 \, \text{nm}$  titanium-sapphire laser.

A laser pulse of  $\tau_L \simeq 50$  fs, focused to a spot size  $A_L$  with diameter  $d_0 = 50 \,\mu\text{m}$  and with a peak power  $P_0$ , would have to exceed a pulse energy of

$$I_0 = \frac{P_0}{A_L} = \frac{E_P}{\tau_L \cdot \pi (d_0/2)^2}$$

$$\Longrightarrow E_P = I_0 \cdot \tau_L \cdot \pi (d_0/2)^2 = 2.1 \,\mathrm{J}$$

to reach such a high peak intensity at its focus.

Despite the scheme of laser-plasma acceleration first being proposed in 1979 by Tajima and Dawson [5], it took until 1985 for fundamental laser technology to enable the generation of laser pulses capable of reaching the required intensity levels, made possible by the invention of chirped-pulse amplification by Strickland and Mourou [28].

#### 1.3.1 Creation of bandwidth-limited Pulses

The creation of ultra-short laser pulses is fundamentally governed by the Fourier limit, which specifies the bandwidth-limited pulse duration  $\Delta \tau_0$  to be defined by the width of its frequency spectrum  $\Delta \nu$  via

$$\Delta \tau_0 \Delta \nu \ge K \tag{1.8}$$

with the value of K defined by the pulse shape. For a Gaussian pulse with a center wavelength of  $\lambda_0 = 800 \,\mathrm{nm}$  and spectral width of  $\Delta\lambda \simeq 19 \,\mathrm{nm}$ ,  $K = \frac{2 \,\mathrm{ln} \, 2}{\pi} \,[26, \, 29]$  leads to a shortest possible pulse duration of  $\tau_0 = 50 \,\mathrm{fs}$ . This fundamental limit of ultra-short laser pulse generation creates the need to use laser active media able to support high gain over such broad spectral bandwidths.

Generation of bandwidth-limited laser pulses can be achieved through "mode locking" between the different components of the laser spectrum. By introducing artificial losses in the cavity via a nonlinear medium, the pulses created through statistical coupling of the phase between adjacent modes experience a strong discrimination based on their intensity. Only the shortest pulses, which represent the phases of all modes in the cavity being locked, experience net amplification. This technique, referred to as passive mode locking, enables the generation of up to bandwidth-limited pulses. [30–32]

Passive mode-locking is employed to generate the  $\sim 38\,\mathrm{fs}$ , nano-Joule pulses from the oscillator in the HTU laser system front end. To reach the  $> 2\,\mathrm{J}$  pulse energy necessary for driving relativistic electron motion (see Sec.1.2.3 and 1.3), further amplification is required. But due to the damage threshold of optics in the laser system and multi-pass amplifier, the intensity of the laser pulse needs to be kept below about  $10\,\mathrm{GW/cm^2}$  [33], limiting the pulse energy of a beam of the above discussed parameters and a beam radius of  $w=1\,\mathrm{cm}$  to about  $E_p=1.5\,\mathrm{mJ}$ . The necessary increase of pulse energy by over three orders of magnitude would exceed the damage threshold of critical optics in the system by the same amount, prohibiting operation in the regime required for LPA operation.

The invention of chirped-pulse amplification (CPA) [28] allowed to surpass this strict pulse energy limit in amplifying femtosecond pulses and lead to the realization of peak powers up to petawatts. The principle of CPA is based on stretching the bandwidth-limited femtosecond pulse, which has an electric field distribution that can be described as a superposition of its individual spectral components:

$$E(t) = \frac{1}{2\pi} \int_{-\infty}^{\infty} \tilde{E}(\omega) e^{i\omega t} d\omega$$
 (1.9)

Through Fourier inversion, its complex spectrum follows as

$$\tilde{E}(\omega) = \int_{-\infty}^{\infty} E(t)e^{-i\omega t} dt$$
(1.10)

with the positive part of the spectrum defined by  $\tilde{E}^+(\omega) = \tilde{E}(\omega)$  for  $\omega \geq 0$  and  $\tilde{E}^+(\omega) = 0$  for  $\omega < 0$ , which can be separated into amplitude and phase

$$\tilde{E}^{+}(\omega) = |\tilde{E}^{+}(\omega)|e^{-i\Phi(\omega)} \tag{1.11}$$

$$= \sqrt{\frac{\pi}{\varepsilon_0 c n} I(\omega)} e^{-i\Phi(\omega)} \tag{1.12}$$

Here,  $I(\omega)$  is the spectral intensity,  $\Phi(\omega)$  the spectral phase, n the refractive index of the material, and  $\varepsilon_0 = 8.85 \cdot 10^{-12} \text{F/m}$  the vacuum permittivity. The spectral phase  $\Phi(\omega)$  can be used to define the group delay  $T_g(\omega) = \frac{\mathrm{d}\Phi(\omega)}{\mathrm{d}\omega}$ , describing the relative temporal delay of a certain spectral component.

The group delay dispersion (GDD), or second order dispersion

$$D2(\omega) = \frac{\mathrm{d}T_g}{\mathrm{d}\omega} = \frac{\mathrm{d}^2\Phi(\omega)}{\mathrm{d}\omega^2}$$
 (1.13)

describes how the laser pulse is affected when acted upon by a medium that causes different spectral components to travel with different group velocities, leading to a time-dependent component of the instantaneous frequency, or "linear chirp".

This effect is utilized in CPA systems through prisms or gratings, to deliberately delay the different spectral components of a broad-band laser pulse with respect to each other, and stretch the temporal duration to hundreds of picoseconds to reduce the pulse peak intensity. [26]

In addition to the CPA technique, the HTU laser system utilizes multiple stages of beam expansion, to further reduce the fluence incident on critical optics.

After the final amplification stage the linear chirp introduced in the stretcher is compensated

by adding negative GDD, compressing the now high-energy laser pulses back down to their bandwidth-limited duration of  $\sim 38$  fs. This finally delivers ultra-short, high-intensity pulses, exceeding the  $a_0 \geq 1$  condition for relativistic electron motion from Sec.1.2.3, to the LPA target.

## 1.3.2 Measurement of Pulse Properties

The effective application of ultra-short laser pulses requires their precise characterization. For the laser-driven generation of plasma waves to accelerate electrons, parameters such as the duration, shape and linear chirp (GDD) of the laser pulse have been shown to be of high significance to the interaction. [34–36]

To fully characterize a laser pulse, its amplitude and phase need to be measured, either in the temporal or spectral domain (their connection by Fourier transformation allows calculation of one through the other). Most classical techniques to measure the spectral amplitude lack the ability to record phase information, and electronic devices to measure temporal pulse shapes are limited to picosecond resolution. The "Frequency-Resolved Optical Gating" (FROG) technique, enabling the measurement of both spectral amplitude and phase, was developed by Trebino and is introduced and described extensively in his textbook [37].

The diagnostic built and characterized as a part of this work is based specifically on a version of the second-harmonic generation (SHG) FROG process, the "GRating-Eliminated No-nonsense Observation of Ultrafast Incident Laser Light E-fields" (GRENOUILLE). It represents a simplified design compared to the basic FROG setup, less sensitive to alignment and allowing full single-shot characterization of the spectral amplitude and phase (and even spatial chirp). [38, 39]

A schematic of the setup and working principle can be seen in Fig.1.

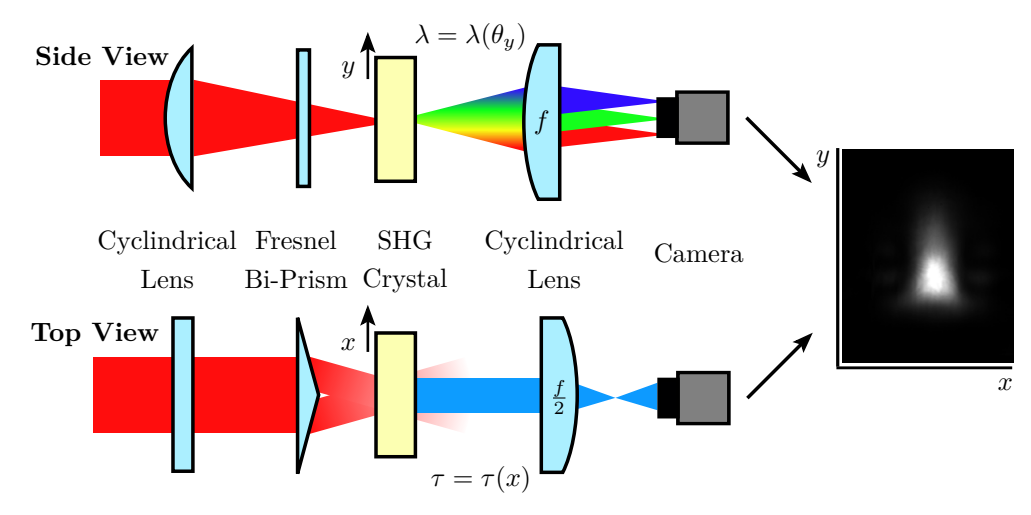


Figure 1: Schematic display of the GRENOUILLE process. Focusing the beam onto a thick SHG crystal using a cylindrical lens, the spectral components  $\lambda$  of the pulse get separated spatially in the vertical plane. A Fresnel bi-prism allows to overlap two copies of the beam at an angle in the same crystal, mapping the relative delay  $\tau$  onto the horizontal crystal position. A cylindrical lens with focal length  $f_y = f$ , and  $f_x = \frac{f}{2}$ , images spectral and temporal information onto the two axes of the camera chip. Schematic adapted from Ref.[37].

Because the individual spectral components of the laser pulse can only generate SHG under

different angles, due to the phase-matching condition, and the cylindrical lens is placed one focal length f away from the crystal, it turns the broad SHG pulse into a vertically dispersed spectrum. From this, the original spectrum of the laser pulse can be calculated.

The Fresnel bi-prism in the horizontal plane creates two copies of the beam with a fixed angular offset, interacting with each other in the SHG crystal. The interference of parts of the pulse with different temporal phase gets mapped onto different horizontal positions of the crystal, but the second order non-linear process causes ambiguity in the direction of time. The complex amplitude of the laser pulse E(t) and its complex-conjugate, time-reversed copy  $E^*(-t)$  both lead to the same detected SHG FROG trace, causing a fully symmetric trace in the temporal axis.

However, due to its compactness, simplicity and sensitivity (among other reasons), *GRENOUILLE* is widely used as a highly capable tool to gain the full pulse intensity and phase from a single shot, for ultra-short laser pulses down to the few femtosecond level. [26, 37–40]

This chapter will introduce the concepts and parameters necessary for the discussion of electron beam properties, which are crucial to the experiments conducted as a part of this work. A much more comprehensive description of electron beam physics can be found in the textbooks written by Rosenzweig [41] and Humphries [42].

## 2.1 Properties of Electron Bunches

To discuss the parameters of electron beam transport, it is helpful to introduce the concept of the "trace space".

The transverse offset x and angle  $\theta_x$  of a particle can be used to describe its trajectory. In terms of its momenta, the angle  $\theta_x$  is defined through

$$\theta_x = \tan^{-1} \left( \frac{p_x}{p_z} \right) \tag{2.1}$$

(analogous for transverse offset and angle in y).

Assuming that the transverse momentum  $p_x$  is much smaller than the longitudinal momentum  $p_z$ , a reasonable assumption in most cases when analyzing electron beams which are defined by particle trajectories close to the design orbit, using Eq.2.1 this "paraxial approximation" (PA) then leads to the description of the derivative of the transverse offset x'

$$x' = \frac{\mathrm{d}x}{\mathrm{d}z} = \tan \theta_x = \frac{p_x}{p_z}$$

$$\stackrel{\mathrm{PA}}{\simeq} \theta_x$$

In the trace space description of an electron bunch, characterized by the particles horizontal offset and angle (x,x'), the rms beam size  $\sigma_x = \sqrt{\langle x^2 \rangle}$  and angular spread  $\sigma_{x'} = \sqrt{\langle x'^2 \rangle}$  can be defined. This allows to represent the trace space area occupied by the particles contained in a particle bunch as an ellipse, as can be seen in Fig.2. The outline of this ellipse represents a defined level of constant beam intensity  $f_x$ , and most commonly the level  $f = f_x e^{-\frac{1}{2}}$  is used, quantifying the "rms trace space ellipse", see Fig.2 below.

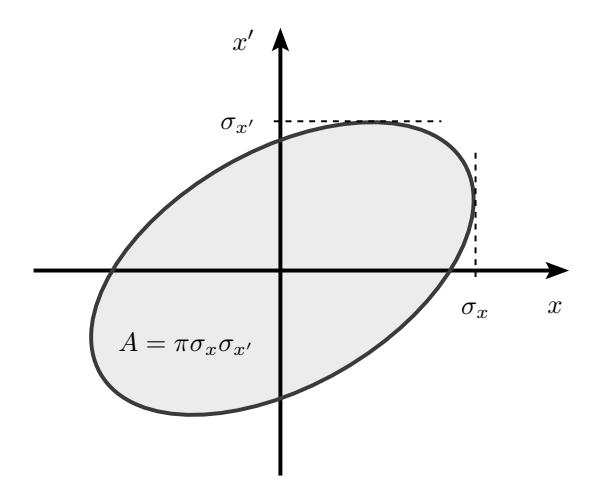


**Figure 2:** Rms trace space representation of an electron beam, as a function of the particles transverse offset x and angle x' from the design trajectory.

The area of the trace space ellipse can be expressed using the "rms beam emittance"  $\varepsilon_x$  through

$$A = \pi \sigma_x \sigma_{x'} \equiv \pi \varepsilon_x \tag{2.2}$$

The area is conserved under beam transport and linear focusing, and the fraction of the beam contained within it is constant (equivalent conditions apply to the longitudinal emittance). The emittance of an electron beam is directly connected to the smallest diameter to which the beam can be focused, making it critical to control emittance growth to achieve a tight focus, required for many applications. [41]

An important metric for the quality of electron beams, especially for their application in light sources, is the beam "brightness". It is a measure of the current density  $j_b$  per unit solid angle in the z direction. Using the above introduced expressions for the rms beam size and angular spread, the brightness B can be expressed through

$$B = \frac{j_b}{\pi \sigma_x^{\prime 2}} = \frac{I}{\pi \sigma_x^2 \cdot \pi \sigma_x^{\prime 2}} = \frac{Q_b}{\tau_b} \frac{1}{\pi^2 \varepsilon_x^2}$$
 (2.3)

which is also determined by the charge Q and length  $\tau_b$  of the electron bunch. [42] To increase the beam brightness, it is therefore imperative to maximize the bunch charge and minimize its duration, transverse size, and divergence. The space charge effect, resulting in a radial force  $F_r$  between electrons in the bunch separated by a distance r

$$F_r = \frac{1}{4\pi\varepsilon_0 \gamma} \frac{q}{r^2} \tag{2.4}$$

fundamentally limits the maximum achievable brightness. Due to the inverse scaling of the space charge effect with the electron energy  $\gamma$ , plasma-accelerators are uniquely suited to generate high-brightness beams. Their accelerating fields, which are orders of magnitude higher than in classical RF accelerators (see Sec.1.2.1), allow for much smaller transverse beam sizes by reducing  $F_r$  and in turn the beam divergence shortly after the electron source. Aided by the uniquely short femtosecond bunch duration, and associated kA peak currents, this enables the production of electron beams with order of magnitudes higher brightness from plasma-accelerators, a key reason for their potential to drive future light source facilities. [43–45] Nonetheless, especially when using LPAs to drive FELs, considering space charge effects can become relevant [46].

Another important parameter of the electron bunch for light source applications is the beam energy spread. Similar to transmissive lenses and optical pulses with a broad spectrum, the "chromaticity" plays a significant role when focusing electron bunches with a large energy spread using quadrupole lenses. The magnetic focusing effect scales inversely with the electron energy, leading to different electron energies being focused at different z positions, causing a larger, more smeared focus with higher energy spread [42]. In combination with the required brightness, this effect sets a strict limit on the acceptable electron beam energy spread for a given light source machine. For example, the Linear Coherent Light Source (LCLS) X-ray free-electron laser (XFEL) operates at an energy spread  $\frac{\sigma_E}{E} \simeq 0.1\%$  [47], over an order of magnitude lower than the energy spread observed in the highest quality electron beams produced on the HTU beamline during the work presented in this thesis. This motivates the introduction of a magnetic chicane into the electron beamline before the undulator, to stretch the bunch and reduce its slice energy spread.

## 2.2 Magnetic Chicane

To discuss the concept of the magnetic chicane for the reduction of electron bunch slice energy spread, it is crucial to first introduce the relevant parameters of longitudinal motion and momentum dispersion.

When discussing the dynamics of a particle bunch travelling along a trajectory z during time t, it is useful to describe their parameters relative to a design particle. The arrival time  $\tau$  of a certain particle can be defined through  $\tau = t - t_0$ , with  $t_0$  the arrival time of the design particle. A particle with a momentum  $p \neq p_0$  (off-momentum particle) will require the time

$$\tau(p) = \frac{L(p)}{v(p)} \tag{2.5}$$

to reach a certain point along the design trajectory, with L the distance traveled and v the particle velocity, dependent on its momentum p. In the paraxial case, the first-order expansion can be expressed as

$$\frac{\delta \tau}{t_0} = \frac{\delta L}{L_0} - \frac{\delta v_z}{v_0} \tag{2.6}$$

Using this equation enables the definition of the temporal dispersion

$$\eta_{\tau} = \frac{\partial(\delta\tau/t_0)}{\partial(\delta p/p_0)} \tag{2.7}$$

as a measure of how much delay an off-momentum particle experiences, compared to the reference particle.

A magnetic chicane has, by design, a large temporal dispersion (or *momentum compaction*) factor. For that reason, it is typically employed to compress stretched, chirped electron bunches in classical accelerator machines, to increase the peak current. However, in the case of sending through an ultra-short, non-dispersed electron bunch from an LPA source, as on the HTU system, the magnetic chicane allows to stretch the bunch duration very effectively.

To quantify the actual impact on the electron bunch, it is helpful to introduce the matrix element

$$R_{56} = -\eta_{\tau} \cdot \Delta s \tag{2.8}$$

with  $\Delta s$  the total path length of the design trajectory through the chicane. The  $R_{56}$  then can be understood as the additional path length through the chicane, as experienced by an off-momentum particle with momentum p. [41]

The concept of magnetic chicane can now be described as the electron beam equivalent to the optical stretcher used in CPA laser systems (discussed in Sec.1.3.1), creating a stretched and chirped electron bunch. As can be seen schematically in Fig.3 (bottom), the first dipole pair introduces a momentum dependent path length difference to the electron beam, which manifests in the form of temporal and transverse energy spread. Higher momentum  $(p > p_0)$  electrons experience a shorter path s through the chicane than the design trajectory ( $s < \Delta s$ ), the opposite is true for lower momentum  $(p < p_0)$  particles. The second pair of dipoles reverses the transverse energy separation and the electron beam after the chicane regains its transverse beam size, but has accumulated twice the amount of longitudinal dispersion picked up after the

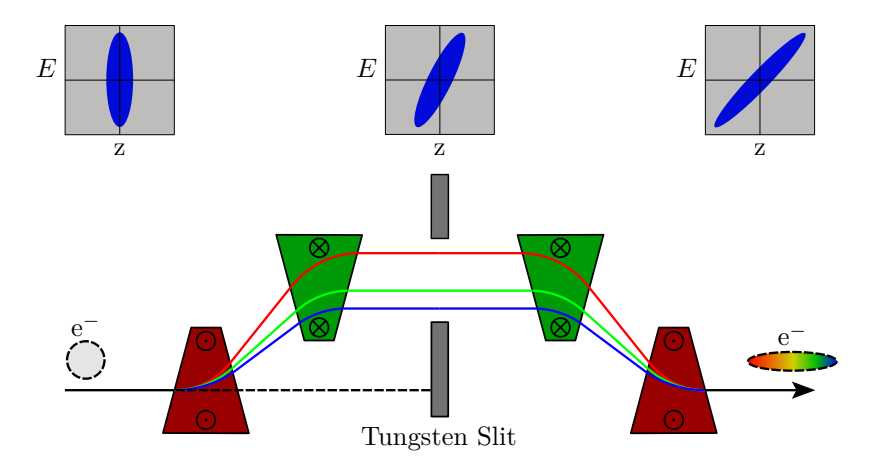


Figure 3: Schematic display of longitudinal stretching of a relativistic electron bunch. The top row shows the correlation between the longitudinal position **z** of an electron inside the bunch and its energy **E**, along the axis of propagation. It qualitatively describes the bunch phase space before (left), halfway through (center), and after the chicane. The figure at the bottom shows the working principle of a magnetic chicane, as used on the HTU beamline. The electron bunch enters the chicane from the left, during the first half of the chicane it gets dispersed transversely and stretched longitudinally. A tungsten slit is used to block the laser on the main axis (dashed line), and by adjusting the slit gap, the energy spectrum of the transmitted bunch can be manipulated. The second half of the chicane reverses the transverse separation of the different electron energies, but introduces further longitudinal dispersion. The stretched and chirped electron bunch exits the chicane on the main z-axis.

first set of dipoles. Accordingly, the rms bunch length has been increased and the peak current decreased. Because the area of the beams trace-space ellipse is invariant under these operations (as described in the previous section), but the total energy spread is maintained, increasing the bunch length in turn causes a reduction in slice energy spread (see Fig.3, top). By changing the field strength of the dipole magnets, the  $R_{56}$  value of the chicane can be manipulated, which changes the amount of longitudinal dispersion and therefor the reduction of slice energy spread experienced by the electron beam. [48–50]

The magnetic chicane used for the experiments discussed in this thesis was custom designed for the HTU system, as described by Majernik et al. in Ref.[50], with the main purpose to reduce the slice energy spread to improve FEL performance. To accommodate for different sets of experimental parameters, the chicane is capable of producing an  $R_{56}$  of up to 1 mm for bunch mean energies of up to 300 MeV. As can be seen in Fig.3 (bottom), it has an additional component to the general setup described above. The set of independently adjustable tungsten pieces functioning as a slit with variable gap size allows to control the central energy and energy spread of the transmitted electron bunch, in addition to blocking the laser beam on the main axis.

This section will motivate and introduce the concept of free-electron lasers (FELs) and give a brief overview of their history. Furthermore, the fundamentals of undulator radiation and SASE FEL theory, required to interpret and discuss the results included in this work, are described. More extensive reviews of free-electron lasers were conducted by Pellegrini et al. [51] and Bostedt et al. [52], and the theory is covered in-depth by Wille [53] and Schmüser [48] in their respective textbooks.

### 3.1 Overview

The development of the first optical light sources based on the stimulated emission of photons from an active medium (lasers) in the 1960s [54], which produced beams of extremely high intensity and coherence, immediately sparked interest to extend their wavelength range into the ultra-violet and x-ray regime. However, due to the inverse scaling of the lifetime of atomic energy levels with their excitation energy, realizing an x-ray laser based on atomic transitions requires pump energies that render this approach highly cumbersome and ineffective. [26, 51, 55]

The concept of using a relativistic electron beam as the active medium, and achieving energy transfer to the radiation field as the particles are transmitted through a periodic magnetic structure (or "undulator") was introduced first in 1971 by Madey et al. [56], and offered a path towards viable x-ray lasing. In 1980, Kondratenko and Saldin proposed utilizing the self-modulation of electron beam density ("microbunching") in a single pass through an undulator, to achieve exponential gain of the radiation arising from spontaneous FEL emission and eliminate the need for optical cavities. [57]

This scheme of self-amplified spontaneous emission (SASE) was demonstrated successfully first in the ultraviolet to infrared regime by the LEUTL [58], VUV-FEL [59] and VISA [60] SASE FELs, the latter machine being re-purposed for the demonstration of LPA-driven FEL lasing described in this work.

These results ultimately led to the proposal [61], construction, and experimental demonstration [62] of the first x-ray free-electron laser (XFEL) at the Linear Coherent Light Source (LCLS), part of the Stanford Linear Accelerator (SLAC).

Since then, the the field of XFELs has expanded to include facilities in Japan (SACLA), Germany (Eu-XFEL), South Korea (PAL-XFEL) and Switzerland (Swiss-FEL). Through their ultra-fast, ultra-high brightness, and ultra-short wavelength beams they have enabled a new scientific frontier of investigating atomic and molecular structures and dynamics on the femtosecond time- and Ångstrom length-scales, accessible through no other current light source technology. [51, 52]

However, due to the fundamental barriers faced by classical accelerators based on RF technology described in Sec.1.1, the current XFELs require kilometer-scale facilities and multi-billion dollar investments, heavily restricting access to their groundbreaking scientific potential by limiting the number of facilities available to the community. Thus, the motivation for using LPAs to drive the next generation of XFELs was born. The work presented in this thesis represents part of the effort conducted on the BELLA Centers HTU beamline to demonstrate reliable operation of a compact, LPA-driven SASE FEL.

## 3.2 Fundamentals

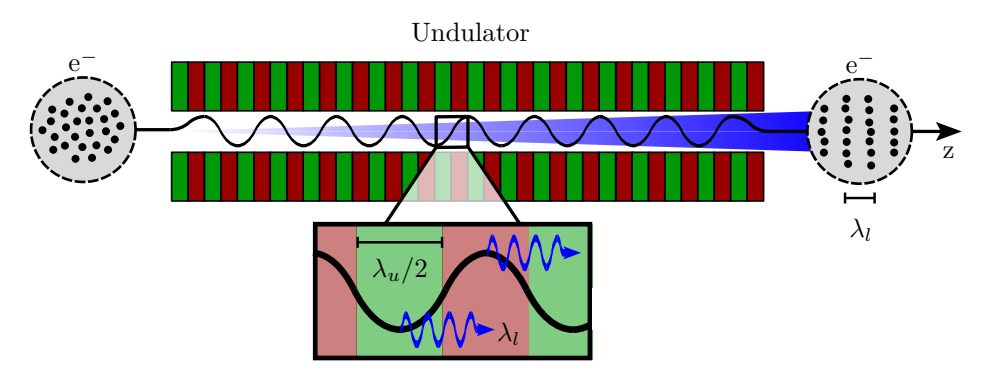


Figure 4: Schematic of the SASE FEL process. An electron bunch is transmitted through the magnetic structure of an undulator with period  $\lambda_u$ , on the magnetic axis z. It transfers energy to the radiation field of wavelength  $\lambda_l$  and experiences microbunching.

#### 3.2.1 Undulator Radiation

When an electron beam of energy  $m_e c^2 \gamma$  travels through the periodic structure of a planar undulator, the transverse acceleration it experiences by the alternating magnetic field causes the charged particles to emit Bremsstrahlung photons, as can be seen schematically in Fig.4. The energy of the photons created through this process is proportional to the particle energy and undulator period  $\lambda_u$  through  $\lambda_u/\gamma^2$ , and the radiation is mostly contained in a narrow cone of aperture  $\theta = 1/\gamma$  around their trajectory in the forward (+z) direction.

Assuming the transverse displacement of the electron beam in an undulator with total length  $L_u$  and peak field strength  $B_0$  to be small enough to neglect in first order, and a detector placed in the far field at  $z_{\text{detector}} \gg L_u$ . The difference in arrival time  $\Delta T$  at the detector of two photons emitted from different locations  $N \cdot \lambda_u$  along the undulator, with  $N \in \{0, N_u\}$  ( $N_u$  the total number of undulator segments), is then given by

$$c \cdot \Delta T = \frac{N\lambda_u}{2\gamma^2} \left( 1 + \frac{K^2}{2} \right) \tag{3.1}$$

with  $K = eB_0\lambda_u/2\pi m_e c$  the dimensionless undulator strength parameter.

Constructive interference is observed when the photons traveling at c slip ahead of the slightly slower electrons by an integer of their own wavelength  $\lambda$  within one undulator period:  $c \cdot \Delta T \stackrel{!}{=} N \cdot \lambda$ . This "coherence condition" defines the peak in the undulator radiation spectrum to be located at the wavelength

$$\lambda_{l,0} = \frac{\lambda_u}{2\gamma^2} \left( 1 + \frac{K^2}{2} \right) \tag{3.2}$$

in addition to higher harmonics of the fundamental wavelength  $N \cdot \lambda_{l,0}$  at reduced intensities.

When considering photons emitted at an angle  $\theta$  with respect to the undulator axis, the coherence conditions changes. To achieve coherent interference, the photon wavelength needs to increase with larger values of  $\theta$ , causing an additional angular dependence term in the coherence condition.

$$\lambda_l(\theta) = \frac{\lambda_u}{2\gamma^2} \left( 1 + \frac{K^2}{2} + (\gamma \theta)^2 \right)$$
 (3.3)

For the on-axis case of  $\theta = 0$ , this leads to the equation for the peak undulator wavelength  $\lambda_{l,0}$ . The total distance a photon emitted at the undulator entrance moves ahead of the electron which emitted it is called the "slippage"  $S = N_u \cdot \lambda_l$ . [26, 48, 51, 52]

## 3.2.2 FEL Lasing and the SASE Regime

Under resonant conditions, a free-electron laser allows the net energy transfer from a relativistic electron bunch to a co-propagating electromagnetic radiation field (or "laser field"), in which case the freely moving electron in the particle bunch acts as the active medium and the transfer process of energy to the laser field can be described analogously to the "stimulated emission" in a classic optical laser system, giving the FEL its name.

Energy transfer between the electrons and radiation field is only possible when the electron velocity has a component parallel to the transverse electric field of the laser, which is enabled by the undulator. To achieve *net* energy transfer, the sinusoidal trajectory of the electrons must always be in phase with the laser field, such that the charged particle is constantly decelerated (or accelerated, which corresponds to net energy transfer from the radiation field to the electron bunch, making it possible to use an FEL as a particle accelerator, suggested first by R.B. Palmer in 1972 [63]).

This requirement to the phase difference between electron and electromagnetic wave  $\Delta\Phi$  leads to the "coherence condition" discussed in the previous section. If fulfilled, an electron with the resonance energy (which follows directly from Eq.3.2)

$$\gamma_r^2 = \frac{\lambda_u}{2\lambda_l} \left( 1 + \frac{K^2}{2} \right) \tag{3.4}$$

loses energy in the presence of a laser with the wavelength  $\lambda_l$  in an undulator of period  $\lambda_u$ . The energy lost by the particle is in turn transferred to the radiation field. This process repeats twice per undulator period, every time the electron changes its transverse direction synchronously with the electric field of the laser. Because the amount of energy transferred from an electron at the resonance energy to the laser field  $\frac{d\gamma_r}{dz}$  is proportional to the laser field strength  $E_{l,0}$ , the coherent interaction allows for exponential gain of the laser field strength, equivalent to a classical laser amplifier.

It is therefor desirable to operate the FEL close to this resonance energy  $\gamma_r$ , and by introducing the difference  $\Delta \gamma$  from the resonance energy, the change in phase between electron trajectory and laser field (as discussed above) can be expressed as a function of the particle energy

$$\frac{\mathrm{d}\Phi}{\mathrm{d}z} = \frac{4\pi}{\gamma_r \lambda_u} \Delta \gamma(z) \tag{3.5}$$

which can be used to define the stable particle orbits around the resonance energy and phase, and corresponds to the "separatrix" for synchrotron oscillations. [53]

Considering a particle bunch close to the resonance energy  $\gamma_r$ , but with a duration of tens of femtoseconds (as to be expected from an LPA source as used on the HTU system [18]), the corresponding transverse length is much longer than the central undulator wavelength  $\lambda_l$ . This immediately poses an issue, seeing how only particles at a well-defined, constant phase  $\Delta\Phi$  with respect to the laser field fulfill the resonance condition necessary for net energy transfer between the two. However, because the phase of particles at a different transverse position  $\Delta\Phi' \neq \Delta\Phi$  is not matching the resonance condition, they experience less deceleration or even

get accelerated by the laser field. This reduces the transverse amplitude of their sinusoidal trajectory in the undulator with respect to the resonant particles, and modulates their longitudinal velocity. Starting from statistical fluctuations in electron density, this effect ultimately causes the electrons to arrange themselves in small bunches shorter than the radiation wavelength  $\lambda_l$ . These so-called "microbunches" are centered around the resonant phase position, spaced at distances  $\lambda_l$  apart (as can be seen schematically in Fig.4), and lead to more and more particles N interacting coherently with the laser field. The growth in radiation field strength scales with  $N^2$  and further enhances the microbunching effect.

There are different techniques to achieve FEL lasing. In the SASE regime, which the VISA undulator on the HTU beamline is operating, the initial radiation field required for coherent amplification arises from spontaneous emission by the electrons based on Bremsstrahlung, as described in Sec.3.2.1. The coupling of the statistical electron bunch density distribution to the external radiation field then leads to the emergence of microbunching, causing the exponential growth of the laser field through "Self Amplification of Spontaneous Emission" or SASE. [48, 52, 53]

The scaling of the exponential increase in FEL signal, described as a high-gain FEL in the 1D limit, can be quantified by the Pierce parameter [64]

$$\rho_{\text{FEL}} = \left[ \frac{1}{64\pi^2} \frac{I_p}{I_A} \frac{K^2 [JJ]^2 \lambda_u^2}{\gamma^3 \sigma_x^2} \right]^{\frac{1}{3}}$$
 (3.6)

which can be seen as a measure of the FEL efficiency based on the electron beam power. In Eq.3.6,  $I_p$  is the electron peak current,  $I_A \approx 17\,\mathrm{kA}$  the Alfvén current,  $[JJ] = [J_0(\xi) - J_1(\xi)]$  the Bessel function factor (for a planar undulator  $\xi = K^2/(4+2K^2)$ ) and  $\sigma_x$  the rms transverse size of the electron beam (see Sec.2.1).

The overall power of the laser field  $P_l$  increases exponentially with the distance through the undulator z

$$P_l(z) \propto \exp\frac{z}{L_q}$$
 (3.7)

with the power gain length

$$L_g \approx \frac{1}{\sqrt{3}} \frac{\lambda_u}{4\pi \rho_{\rm FEL}} \tag{3.8}$$

Because a higher peak current and a smaller transverse size of the electron beam increase the Pierce parameter (see Eq.3.6), they lead to a shorter gain length. An increased emittance increases the beam spot size, reducing the electron density and increasing  $\rho_{\rm FEL}$ . Higher energy spread and divergence of the beam, due to their impact on the emittance (see Sec.2.1 and Eq.2.2) will also lead to a longer gain length  $L_g$ . This effect motivates the use of a magnetic chicane to reduce the slice energy spread, as discussed in Sec.2.2, to reduce the gain length and increase FEL performance.

However, this exponential gain of radiation power can not be sustained indefinitely. After reaching micro-bunching and coherently radiating in phase, the particles eventually lose enough energy to violate the coherence condition, and start to get accelerated again by extracting energy from the radiation field. This point in the SASE FEL process is described by the so-called

"saturation power" which can be estimated through

$$P_{sat} \approx \rho_{\text{FEL}} \cdot P_{beam} \tag{3.9}$$

with  $P_{beam} = \frac{\gamma m_e c^2 I_0}{e}$  the power of the electron beam, and  $I_0$  the electron beam current [48]. Due to the coherence condition and the accordingly narrow spectral bandwidth, the temporal coherence of the SASE FEL radiation is limited. The coherence length

$$L_{\rm coh} \approx \frac{\sqrt{\pi}c}{\sigma_{\omega}}$$
 (3.10)

is a measure of the spatial distance over which light emitted from the electrons contained within it can be amplified coherently.  $\sigma_{\omega}$  represents the rms bandwidth of the SASE FEL radiation. [65, 66]

If the bunch length  $L_b$  is much larger than the coherence length  $L_{\rm coh}$ , this causes separate parts of the electron bunch to behave as independent lasing sources. The number of longitudinal modes  $M = L_b/L_{\rm coh}$  is a measure of the average number of temporal spikes contained in a SASE FEL pulse, arising from independently radiating parts of the bunch. The rms fluctuation of measured pulse energies from a SASE FEL therefore scales with  $1/\sqrt{M}$  [52]. These theoretical expectations were experimentally verified as a part of the work presented here, and discussed in detail in Sec.7.4.3.

This section will give a detailed overview of the full experimental setup on the Hundred TeraWatt Undulator (HTU) system. From the oscillator, amplifiers and pump laser, to active stabilization systems and diagnostics, the entire laser system is discussed in Sec.4.1. The parameters of the electron source and optics, for delivery and control of the bunches, are presented in Sec.4.2. Finally, the VISA undulator and all relevant diagnostics and controls for FEL gain optimization and characterization can be found in Sec.4.3.

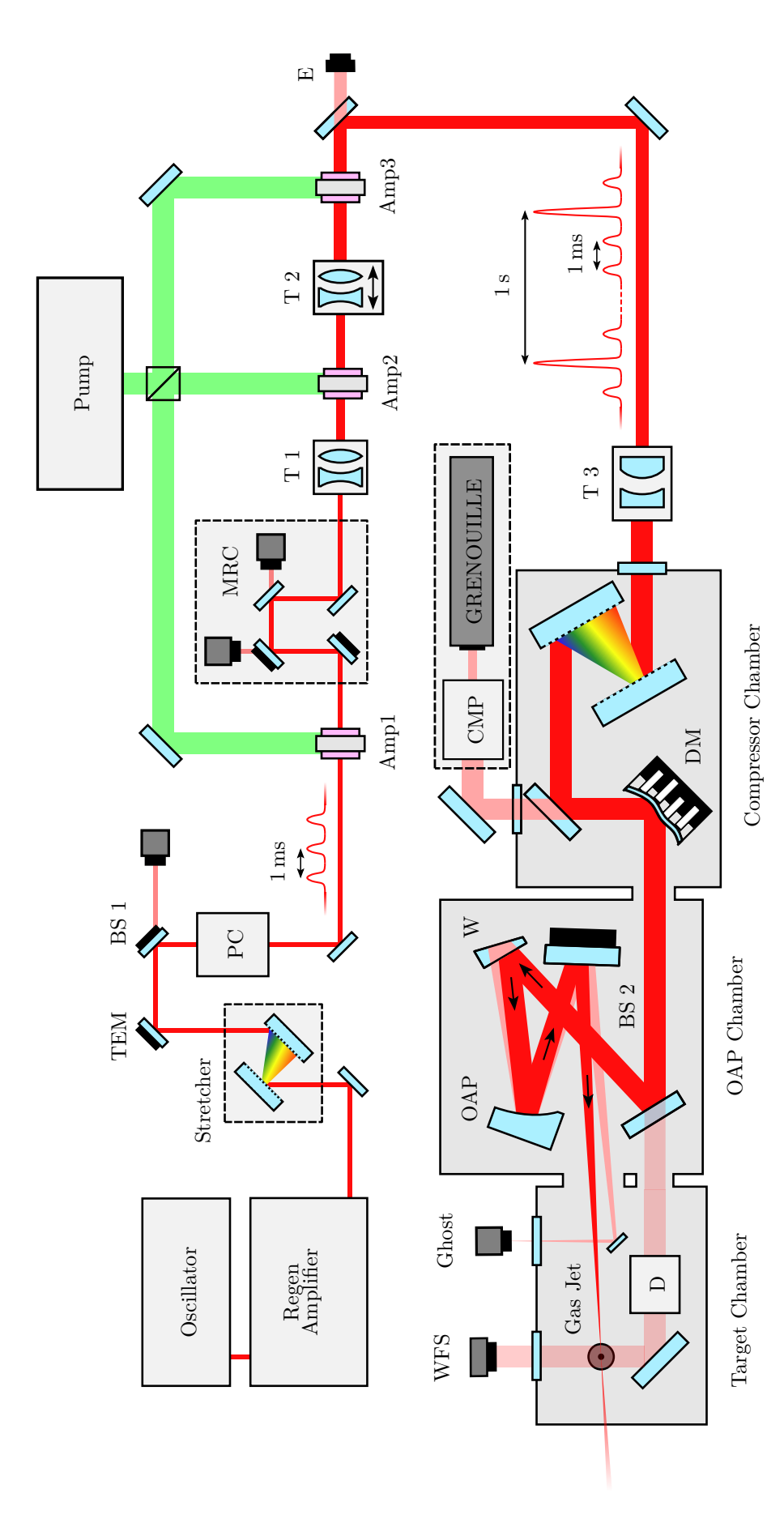
## 4.1 Laser System

The laser used for electron acceleration on the BELLA Center's HTU system, schematically displayed in Fig.5, is a Ti:Sapphire based, chirped pulse amplification (CPA) system delivering 800 nm pulses in the 100 TW regime to the target area.

The front-end is based on a commercial system from *Coherent* [67], a *Vitara* 80 MHz oscillator followed by a *Legend Elite* regenerative amplifier. After this first amplification, the 38 fs, 2.5 mJ pulses at a reduced repetition rate of 1 kHz are sent to the stretcher, where the pulse duration is stretched to 290 ps to reduce the risk of damaging sensitive optics during and after the next amplification stage.

After the stretcher, the beam passes through a setup to increase the pulse contrast, consisting of a Pockels Cell (PC) and set of linear polarizers. Despite the repetition rate of the final amplified pulse only being 1 Hz, the PC is operated at 1 kHz to maintain the un-amplified background pulse train for diagnostic purposes. Beam pointing and angle into the PC are controlled by an active stabilization system from *TEM Messtechnik* [68].

The beam is then sent to the main amplifier, consisting of three stages based on separate water-cooled Ti:Sapphire crystals. They are all pumped by the same 16 J, 16 ns GAIA laser from THALES [69], with a center wavelength of 532 nm. In the first stage (Amp 1), the pulse performs four passes through the crystal and gets amplified to about 100 mJ. The transverse beam position on the first crystal is stabilized against long-term drift using a custom beam pointing system (BS 1, as can be seen in Fig.5), and on the second amplification stage (Amp 2) by an active system from MRC Systems [70] at 1 kHz (utilizing the background pulse train), described in Sec.6.1. Four passes through the crystal in Amp 2 take the pulse energy up to about 1 J, and in the final stage (Amp 3), performing another three passes, the pulse energy is pushed to the final  $\sim 4.2 \,\mathrm{J}$ . To keep the beam intensity on the optics during and after the amplification process below their respective damage threshold, the beam is expanded from 6 mm to 12 mm FWHM between the first and second stage (T 1), and subsequently to 23 mm before the third stage (T 2). The second lens in telescope T 2 (see Fig.5) is mounted on a motorized linear stage, allowing to control the downstream wavefront radius of curvature. This variable telescope setup is used in closed loop with a wavefront sensor (WFS) for active stabilization of the longitudinal focal position, described in Sec. 6.4. After the final pass through the Amp 3 crystal, the pulse energy is recorded non-invasively through a calibrated energy meter (E) and a reflective mirror telescope (T 3 in Fig.5) expands the beam size to 81 mm FWHM. This pulse train, consisting of the amplified pulses at 1 Hz, and the low power background pulses at 1 kHz,



the Pockels cell (PC). A custom (BS 1) and a commercial (MRC) beam stabilization setup are used to stabilize transverse beam positions on the three temporal pulse dynamics. The deformable mirror (DM) optimizes pulse wavefront quality. After the DM, a copy of the beam is used as a probe for the plasma, timed with respect to the main pulse through a delay line (D) and detected by a wavefront sensor (WFS). A wedged mirror (W) creates a low-intensity copy of the main beam ("ghost beam"), both get focused by the off-axis parabolic mirror (OAP). The final steering mirror (BS 2) is amplifier crystals (Amp 1, 2 and 3). T 1 and T 2 are transmissive and T 3 a reflective beam expander telescope. The beam energy after amplification is non-invasively monitored (E). A leakage beam sent to the chirped mirror compressor (CMP) and GRENOUILLE allows monitoring of spectral and Figure 5: Schematic display of the Hundred TeraWatt Undulator (HTU) laser beamline. The pulse position and angle are actively stabilized (TEM) through used for active stabilization of the main beam position on target.

is then sent to the compressor.

Transmitted into the vacuum system and then entering the compressor chamber, the pulse gets compressed from 290 ps back down to its bandwidth-limited duration of about 38 fs. One of the two gratings is mounted on a linear translation stage, allowing for micrometer precise control of the grating separation, and in turn pulse compression. After the grating compressor, the beam is sent onto a commercial, 20 cm diameter deformable mirror (DM) from *Imagine Optic*, which enables control over the pulse wavefront. Leakage of the beam through a high-reflective (HR) optic is picked up for non-invasive, on-shot characterization of temporal and spectral pulse dynamics, based on a commercial *GRENOUILLE* diagnostic from *Swamp Optics*. The design and characterization of this diagnostic setup are described in detail in Sec.5.2.

Post compression and wavefront control, another leakage of the main beam gets sent straight to the target chamber and intercepts the gas jet target orthogonal to the main beam axis. It is picked up by a high resolution wavefront sensor (WFS) from *Phasics* to monitor the plasma density profile. The main beam in the OAP chamber beam is reflected onto a wedged fused silica optic (W), creating a low-intensity copy of the main beam. The setup was designed such that the front and back surface reflection overlap on the 3 m focal length off-axis parabolic mirror (OAP), with an angular separation of 1.21°. The final steering mirror (BS 2), located 1 m downstream of the OAP, then controls the transverse position of the laser focus against long-term drift, via a custom stabilization system. To monitor the beam position at focus non-destructively, for the purpose of active stabilization, the ghost beam is picked off by a mirror after the final steering optic and directed onto the detection setup outside of the vacuum system. The correlation of pointing between this "ghost beam" and the main beam has been extensively investigated and confirmed by Isono et al. in Ref.[71].

The laser system finally delivers an amplified 38 fs pulse of up to 2.5 J at 1 Hz to a spot of 40  $\mu$ m FWHM, corresponding to an intensity of  $\sim 5.2 \cdot 10^{18} \text{W/cm}^2$  on target.

## 4.2 Gas Jet Target and Electron Beamline

The electron beamline of the HTU setup, as seen schematically in Fig.6, includes the LPA target for generation of quasi-monoenergetic electron bunches, capabilities for dispersion and emittance growth mitigation, separation of electron and laser beam, bunch length and spectrum control, as well as variable focusing and steering.

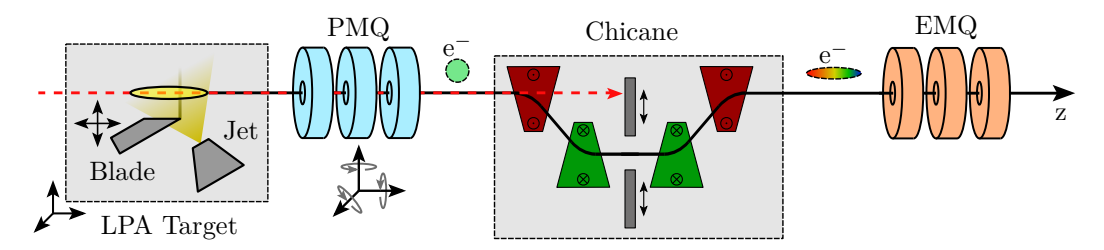


Figure 6: A schematic of the HTU system target assembly and subsequent electron beamline, used to deliver and match the electron beams to the VISA undulator. The trajectory of the laser pulse is shown as the red dashed line, the electron beam trajectory in black. Elements of the electron beam transport line after the gas jet target include a permanent magnet quadrupole (PMQ) triplet, magnetic chicane with adjustable tungsten slit, and electromagnetic quadrupole (EMQ) triplet.

A supersonic gas jet, capable of delivering helium at a pressure of up to 500 psi (pounds per square inch) to the interaction region, is the source for the plasma channel generated by the 2.5 J, 38 fs laser pulse at its 40 µm focal spot location. A blade is rigidly mounted above the gas jet to create a density shock in the gas profile, which enables generation of electron beams through the down-ramp injection process (see Ch.1.2.2). To control and tune the injection, the longitudinal and vertical position of the blade with respect to the gas jet are controllable, and the whole gas jet assembly (including the blade) can be translated with respect to the laser focus with three degrees of freedom, as displayed in Fig.6.

For most of the experiments discussed in this thesis, the jet assembly was tuned to produce electron beams of 100 MeV central energy. For such beams, the central energy rms jitter would typically be on the order of 2.5 MeV, with 1 - 3% rms energy spread and a bunch charge of  $90 \pm 30 \,\mathrm{pC}$  [72].

Beams with such comparably high energy spread and strong divergence are subject to significant chromatic emittance growth [73]. To reduce this effect and control the electron beams divergence after the plasma target, a permanent magnet quadrupole (PMQ) triplet is placed 3.5 cm behind the interaction point. For precise alignment of the PMQs magnetic axis to the electron beam trajectory, necessary to avoid introducing dispersion, the PMQ is mounted on a hexapod that provides full translation and rotation control (six degrees of freedom).

A custom magnetic chicane (described in Sec.2.2) 1 m behind the plasma source serves multiple purposes for the HTU experiment. For one, separating the electron beam path from the laser axis allows to eliminate stray laser and plasma light and prevent damaging more sensitive electron beam diagnostic equipment downstream. By inserting an adjustable tungsten slit, the laser is blocked and only the electrons at a defined transverse offset from the main axis and with a certain energy are transmitted. More importantly, it also reduces the electron bunch slice energy spread by stretching it, which has been shown to significantly improve and stabilize

FEL lasing by reducing the FEL gain length [74]. For the experiments conducted as part of this thesis, the chicane was set to generate  $R_{56}$  values of 150-200  $\mu$ m. Due to the lack of diagnostic equipment to precisely determine the 6D phase space of our electron beams, the  $R_{56}$  values used were experimentally determined to deliver the highest and most stable FEL gain.

After the chicane, the electron beam passes through an electromagnetic quadrupole (EMQ) triplet, which allows to precisely control the beam divergence. This is crucial for matching with the external periodic focusing of the FODO lattice, which is embedded in the VISA undulator. A pair of dipole steering magnets before and after the EMQ allow optimization of the electron beam trajectory through the triplet and into the VISA undulator.

#### 4.3 VISA Undulator

The undulator integrated into the HTU beamline is the VISA (Visible to Infrared SASE Amplifier) undulator [75], which was designed and built to be used at Brookhaven National Lab for one of the first FEL lasing demonstrations in the SASE regime [60, 76]. It consists of four identical, 1 m long sections that are embedded in a vacuum chamber. There is no free drift space between the segments, which each contain 55 periods (220 total). The rms undulator parameter is K = 0.9 and undulator period  $\lambda_u = 1.8 \,\mathrm{cm}$ , which corresponds to a resonant wavelength of 420 nm when using electron bunches at a central energy of 100 MeV (see Eq.3.2).

The VISA undulator was initially designed to be run with a classical LinAc source, a high beam density, and short FEL gain length, achieved by keeping the beam tightly focused along the whole length of the undulator. This required a unique addition to the magnetic structure in the form of four permanent magnet quadrupoles per undulator segment, arranged in a standard FODO lattice. With an effective field gradient of  $33\,\mathrm{T/m}$  and for electrons of energies between 70 and  $100\,\mathrm{MeV}$ , this distributed quadrupole focusing results in a  $\sim 60\,\mathrm{deg}$  phase advance (with four cells per each of the four undulator segments). The disadvantage of the additional focusing, especially for running with an LPA source (which is inherently less stable), are the significantly tighter alignment tolerances, both of the four segments to each other, and the electron beam to the undulator axis. [77, 78]

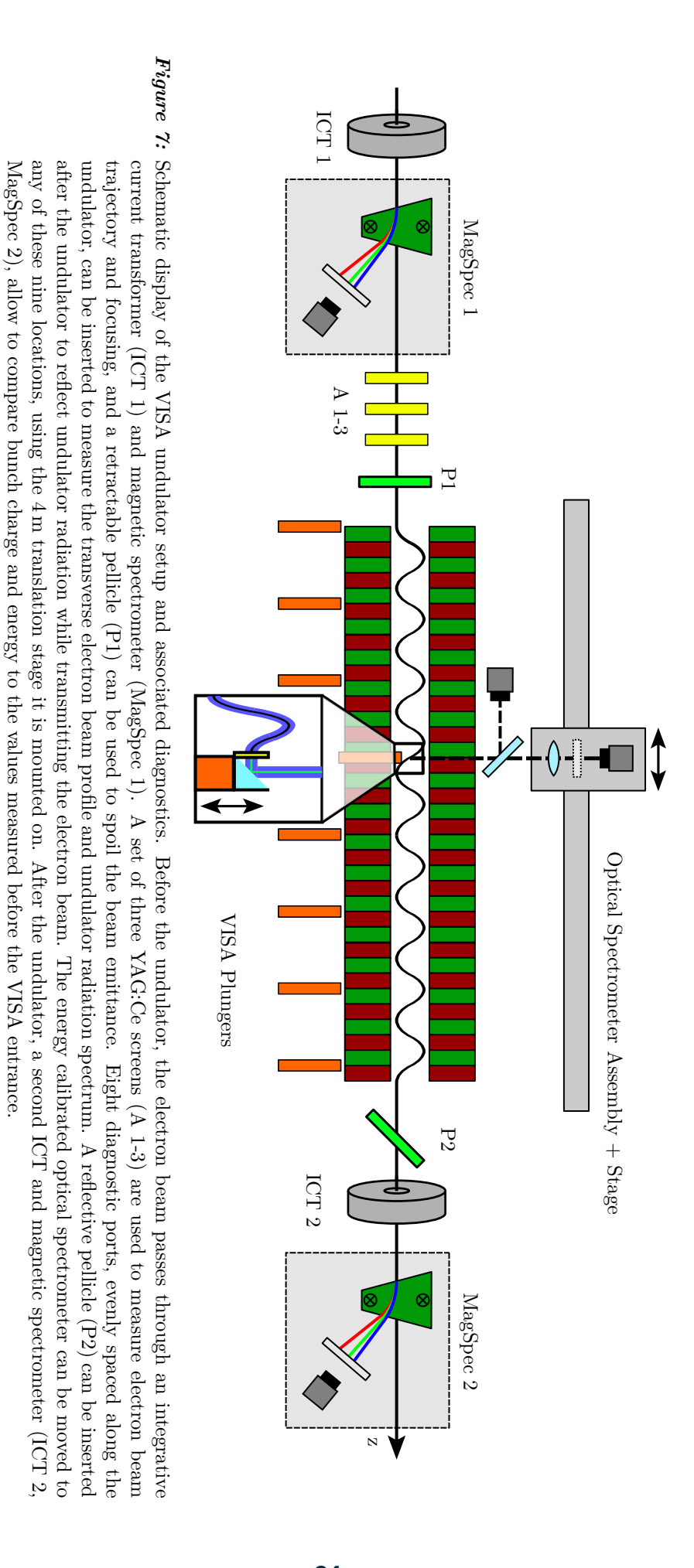
To prevent significant reduction in FEL performance, the electron beam trajectory should not deviate more than  $100\,\mu\mathrm{m}$  from the undulator axis along the four segments. Assuming the four undulator segments have a relative offset of less than  $100\,\mu\mathrm{m}$  with respect to each other, enabling adjustment of the electron beam trajectory inside the undulator can make alignment to the axis less challenging. For this purpose, 8 dual-axis dipole magnets were added externally and distributed along the whole length of the VISA undulator vacuum chamber.

Because VISA was meant to be operated in the visible to infrared spectrum, the diagnostics for the FEL radiation and electron beam profile along the length of the undulator were designed accordingly. The setup includes eight plungers, evenly spaced  $0.5 \,\mathrm{m}$  apart, which can be inserted normally with respect to the undulator axis. As is displayed schematically in Fig.7, all of them have a  $0.2 \,\mathrm{mm}$  thick,  $3 \times 3 \,\mathrm{mm}$  YAG:Ce screen and a right angle prism mirror mounted behind it, which allows imaging of the electron beam profile and collection of undulator radiation at the same time.

Each of the eight ports also has an identical diagnostic setup outside the vacuum chamber, consisting of a dichroic mirror, which directs the  $550\,\mathrm{nm}$  YAG:Ce emission (transverse electron beam profile) to a camera imaging the screen surface with  $7.5\,\mu\mathrm{m}$  resolution, and the  $420\,\mathrm{nm}$  undulator radiation to an optical spectrometer.

The spectrometer is mounted on a 4 m long, linear translation stage that allows the diagnostic to move to any port along the length of the undulator. The spectrometer is custom built, energy calibrated, and has a range of about 300-550 nm. A 5 cm diameter, UV enhanced lens ensures efficient light collection, and focuses the undulator signal through a transmission grating onto the chip of a high resolution CCD camera (a more extensive review can be found in Sec.5.3.1).

In addition to the eight identical plungers, a thin reflective pellicle (P2, see Fig.7) can be inserted after the undulator. It reflects only the undulator radiation while just minimally affecting the transmitted electron beam.



#### 4 The Hundred TeraWatt Undulator System

This set of diagnostics allows not only to precisely monitor the electron beam trajectory and beam size, but also the evolution of FEL radiation along the entire length of the undulator.

The fact that the VISA undulator and corresponding diagnostics setup was designed for visible to IR light is a constraint that affected the choice at which wavelength / electron energy to operate the HTU system. Pushing to electron bunch energies exceeding 100 MeV (wavelengths below 420 nm) will prohibit the use of most of the optical diagnostics for the FEL radiation along the undulator (due to absorption in the transmissive glass optics like windows and lenses), which will make the process of optimizing for higher gain inherently more difficult. An XUV spectrometer has been installed and commissioned, but only is able to collect light at the end of the undulator.

Aside from monitoring the electron beam along the undulator sections, there are additional diagnostics integrated into the beamline. A pair of integrating current transformers (ICTs) allow to measure charge transmission through the VISA undulator. Two magnetic spectrometers of identical specifications enable measurement and comparison of the electron spectrum before and after the undulator. Lastly, a 10  $\mu$ m thick nitrocellulose pellicle (P1) on a plunger before the undulator entrance serves as an emittance spoiler. By inserting and retracting the plunger one can quickly distinguish between incoherent undulator light and coherent FEL radiation (see Sec.5.3.2 for a more detailed description).

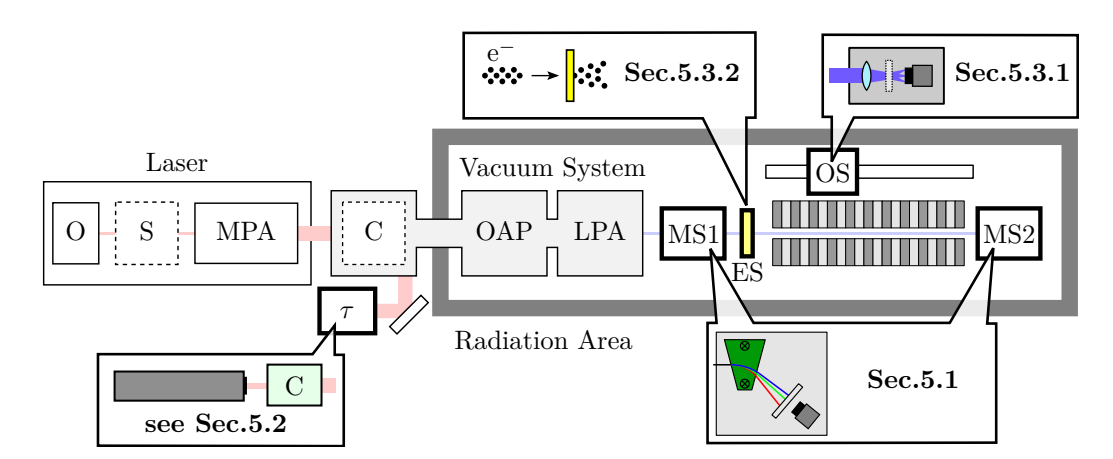


Figure 8: Schematic overview of the HTU system and locations of the diagnostics discussed in this section. After the laser system, consisting of oscillator (O), stretcher (S), and multi-pass amplifier (MPA), the laser pulse is transmitted into the vacuum system. Following the compressor (C), a leakage beam is coupled out to the pulse duration diagnostic ( $\tau$ ) discussed in Sec.5.2. The main beam is sent to the radiation area, which contains the OAP and target chamber (LPA). The two magnetic spectrometers (MS1 & MS2) are discussed in Sec.5.1, the emittance spoiler (ES) in Sec.5.3.2, and the optical spectrometer (OS) for undulator radiation in Sec.5.3.1.

This section will give a detailed overview of upgrades and additions to the diagnostic capabilities of the HTU system that were developed as part of the work for this thesis. They can be seen schematically in the overview Fig. 8.

First, the calibration and installation of new camera and objective pairs for the two magnetic spectrometers on the electron beamline will be discussed in Sec.5.1. This upgrade enabled higher resolution imaging of the scintillating screens and a higher degree of compatibility with the modernized control system infrastructure.

Secondly, Sec.5.2 will elaborate extensively on the design, setup and characterization of the on-shot, non-invasive pulse duration diagnostic based on a commercial *GRENOUILLE* device [79, 80]. After discussing first results and the discovered instabilities of the laser pulse duration, this section will explain the efforts to develop a custom retrieval algorithm for the spectral phase and pulse duration.

Finally, Sec.5.3 focuses on upgrades to the diagnostic capabilities of the VISA undulator [75] specifically. This includes the setup and characterization of the optical spectrometer used for the observations of the first undulator radiation on the HTU beamline, as well as its subsequent upgrade for higher UV transmission. Furthermore, the installation and working principle of the emittance spoiler pellicle, allowing to distinguish between coherent and incoherent FEL emission, is discussed.

# 5.1 Magnetic Spectrometer

As discussed in the previous section, the pair of magnetic spectrometers in use on the HTU beamline are based on an electromagnetic dipole with variable field strength (see Fig.7). The electron bunches are deflected by the dipole field onto a Lanex fast scintillating screen from Kodak [81]. The cameras initially installed to monitor the light emitted from the screen, and enable the calculation of electron beam energy and charge from the captured images, are 14 years old and limited in chip resolution and their compatibility with a modernized control system infrastructure.

Therefore, the decision was made to upgrade the diagnostic cameras to newer *Basler acA* 720 models [82], which contain about double the number of pixels for the same chip size and support Ethernet instead of FireWire connection, offering better compatibility with the existing suite of modern diagnostics on the HTU system.

To ensure the right electron bunch charge is calculated from the measured counts emitted by the scintillating screen, any combination of camera and objective has to be calibrated. The measurements and calculations for the characterization of the new diagnostic setup, required before the actual implementation into the magnetic spectrometer, will be discussed in the following section.

The initial camera and objective pair installed in the HTU magnetic spectrometer setup was calibrated at the Advanced Light Source (ALS) at Lawrence Berkeley National Laboratory (LBNL) by Nakamura et al. [83], using the Lanex screen installed on the spectrometer, and electron beams of known charge and energy.

The key to the calibration of the new camera and objective pair will be to determine a calibration between it and the old, ALS calibrated, diagnostic setup.

For this purpose, the dependencies of camera field-of-view (FoV), camera counts, and the camera-to-screen distance z, will be measured. Comparing the results to the values determined by Nakamura et al., will allow the calculation of the calibration factors between the new and old camera setup. This way, the the energy and charge calibration from the ALS can be transferred to the new camera and objective pair.

# **5.1.1** Longitudinal FoV Dependence

The first step before removing the old camera setup from the magnetic spectrometer, and key to the correct calibration, was to determine its camera-to-screen distance z. For this purpose, references on the Lanex mount in the form of markers spaced exactly 1 cm apart were utilized. Taking a reference image with the currently installed camera allowed to extract the cameras FoV value of FoV = 171 mm from the scaled image, using the software ImageJ. Afterwards, a calibration setup was designed and commissioned to determine the cameras FoV-z dependence, as can be seen in Fig.9a).

The tape measure in the plane of the calibration light source allowed precise and direct measurement of the FoV for different values of z, for a precise determination of the linear dependence between the two. Nakamura et al. [83] had already measured the FoV-z dependence for the camera and objective pair currently in use, but it was hard to reproduce from which reference point of the camera z had been measured (front of the objective, camera chip, etc.). So it was measured again here, from the front of the objective to the Lanex screen, which was added in front of the LED light source to imitate scattering from the screen in the magnetic

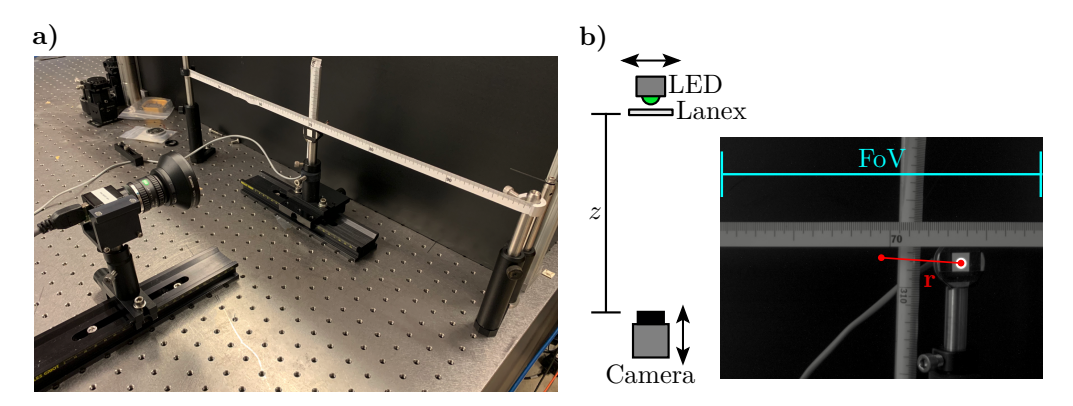


Figure 9: a) Picture of the setup to measure correlation between measured counts for a camera-objective pair and the distance to a calibration light source (green LED behind a 1 cm² Lanex screen, same light source used by Nakamura et al. in Ref.[83]). The camera-to-screen distance z can be varied by translating the camera on the longitudinal stage it is mounted on. The transverse sensitivity is measured by moving the LED assembly on the stage it is mounted on, horizontally to the camera. The FoV can be directly extracted from the images taken, due to the tape measure added to the plane of the light source.

b) Schematic display of the setup and an example image (exposure and contrast adjusted from the original image for display purposes). The image shows how the FoV can easily be determined from the image. For the calibration of transverse sensitivity, the distance of the LED to the center of the image r is calculated in post-analysis.

spectrometer. Fortunately, within the margin of uncertainty, both the slope and offset values match almost perfectly, as can be seen in Tab.1.

measured	$FoV(z) = (0.726 \pm 0.003) \cdot z + (21.309 \pm 0.466 \text{mm})$
Nakamura et al.	$FoV(z) = 0.732 \cdot z + 22.753 \text{mm}$

**Table 1:** Correlation between the cameras FoV and the camera-to-screen distance z, as measured as part of this work, and by Nakamura et al. in Ref.[83]

Comparing the two results strongly indicates that Nakamura et al. measured z from the same reference position on the camera. Because the two results match so closely, and their charge calibration will be used to cross-calibrate our new camera, their FoV dependence will be used going forward as well, for consistency.

For the measured FoV of 171 mm of the original camera installed in the magnetic spectrometer, using the dependency measured by Nakamura et al. (see Tab.1), the corresponding z value can now be calculated

$$z_{\text{calibrated}}(\text{MagSpec}) = \frac{\text{FoV} - 22.75}{0.73} = 202.66 \,\text{mm}$$
 (5.1)

This will allow comparing the sensitivity between the old and new camera setup, when installed at the same distance z from the Lanex screen.

# 5.1.2 Camera Sensitivity

To determine the sensitivity calibration factor  $\Delta S$ , the total number of counts measured with the old ALS calibrated camera setup and the new uncalibrated camera setup will be compared. For this purpose, they will be installed at the same distance  $z=z_{\text{calibrated}}$  from the LED light source, which is set to the same parameters, and using the same exposure time.

Setting the reference parameters on the calibration light source (green LED) to 10 V, 165 mA and the camera to 300 ms exposure time, the total counts measured with the old camera setup are  $N_{\text{old}} = 22.331 \cdot 10^5$ .

Using the same parameters with the new camera setup saturated the chip. So the images were taken at 150 ms exposure, and the total number of counts adjusted accordingly. This led to a total number of counts of  $N_{\text{new}} = 32.134 \cdot 10^5$ , at the same z position.

These results allow the determination of the first calibration factor  $\Delta S$ , which accounts for all differences in chip sensitivity, resolution, size, as well as light collection from the objective, etc.  $\Delta S$  simply follows from the ratio of measured counts for both cameras, given an identical light source at fixed distance  $z_{\text{calibrated}}$ :

$$\Delta S = N_{\text{old}}/N_{\text{new}}(z_{\text{calibrated}}) = 0.6949 \tag{5.2}$$

This represents a roughly 44% increase in sensitivity of the new compared to the old camera setup.

# 5.1.3 Longitudinal Sensitivity

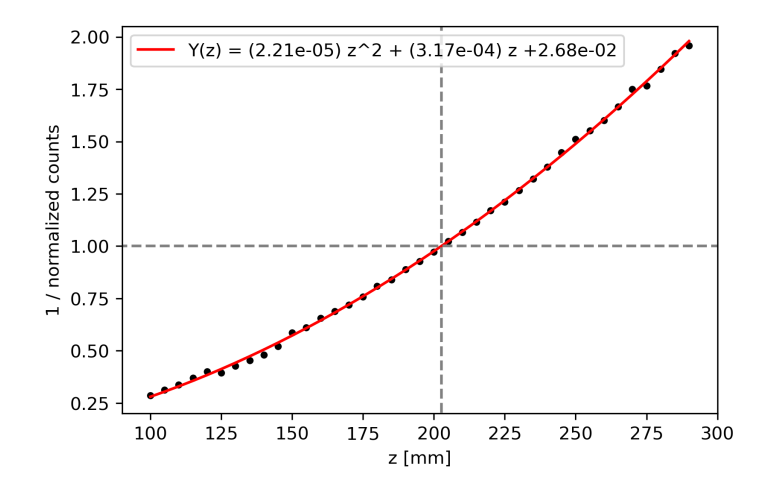


Figure 10: Measuring the longitudinal sensitivity of the new camera-objective pair by determining the dependence between measured counts of a Basler acA 720 and the distance between camera and light source z. The counts are normalized to the value at  $z_{\rm calibrated}({\rm MagSpec})$  (see Eq.5.1). A second order polynomial is fit to 1 / normalized counts (red curve) to extract the calibration factor Y(z).

The next step in the calibration of the new camera is to quantify its dependency between the measured counts and varying camera-to-screen distance, when everything else is kept constant. To experimentally determine it, the setup shown in Fig.9 was used. With the previously used LED and camera settings, the camera was moved along the rail in z direction and ten images taken every 5 mm. Because the relative size of the Lanex screen (which is mounted in front of

the LED) in the images taken changes with varying z position, the FoV(z) calibration was used to calculate the size of the 1 cm  $\times$  1 cm screen in pixels for every z position. After determining the position of the center of the LED in the image, the area corresponding to a circle with radius 5 mm was integrated. This way, an area of constant absolute size was used for the determination of the total number of counts, at all different longitudinal positions.

Fig.10 shows the result, when displaying 1 / normalized counts (normalized to the number of total counts measured at the reference position  $z_{\text{calibrated}}(\text{MagSpec})$ . The data showes an inverse quadratic dependence, which was to be expected when measuring the brightness of a light source emitting into roughly a half sphere. The factor Y(z) is larger than 1 for  $z > z_{\text{calibrated}}(\text{MagSpec})$ , to compensate for less signal due to an increased camera distance, and vice versa.

Combining both parameters determined so far allows to calculate the amount of counts the old, ALS calibrated camera setup would have measured, from the number of total counts detected by the new camera setup. However, so far this is only accurate for a light source located at the center of the image.

# 5.1.4 Radial Sensitivity (Vignetting)

The last step of camera calibration is to account for the changing radial sensitivity or "vignetting", when the light source is not imaged onto the center of the chip. One can expect a combination of effects, from increased effective distance to the source (when the LED is translated horizontally for a fixed z) and the corresponding inverse quadratic dependence, to additional reduction in collection efficiency of the camera objective.

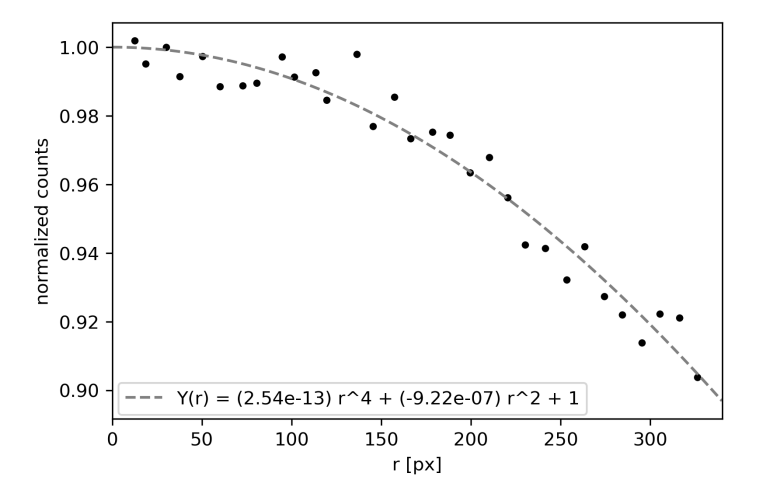


Figure 11: Radial sensitivity of the diagnostic measured by changing the transverse offset between camera and light source. From the images, the normalized counts, integrated over the 5 mm radius circle around the LED center, were calculated and plotted over the distance of the LED center to the chip center r. A fourth order, custom polynomial fit was used to approximate the trend.

To investigate this, the transverse offset of the LED with respect to the camera was systematically scanned, at the fixed distance  $z_{\text{calibrated}}(\text{MagSpec})$ . The images were analyzed to determine the distance r in pixels (px) between the point the LED is imaged to and the center of the camera chip,  $r[px] = \sqrt{(x[px])^2 + (y[px])^2}$ , which can be seen in an example image from this scan in Fig.9b). The total camera counts were integrated in the same way as described for the analysis of the longitudinal sensitivity, which leads to the plot shown in Fig.11. A significant effect on the measured counts can be observed when translating the light source orthogonal to

the camera, the number of counts measured are reduced by 10% at the edge of the chip (with respect to the center).

To determine the transverse sensitivity calibration factor Y(r), accounting for the observed effect, a custom fourth order polynomial (using just even exponential terms) was fitted to the data. This method was chosen to follow the procedure established Nakamura et al. [83]. Because, as discussed above, a combination of different effects can be expected to impact this radial sensitivity, it is not surprising the trend can not be precisely described by a simple quadratic model.

#### 5.1.5 Full Calibration

The parameters determined in the previous sections 5.1.2, 5.1.3, and 5.1.4 now provide a full calibration for the new camera and objective pair. Combining them to the factor  $C_{\text{calibrated}}$  allows the calculation of the total number of counts as they would have been measured by the old, charge calibrated camera setup, from the counts measured with the new camera setup at a certain distance z from the screen, and with the light source at a distance r from the center of the image:

$$C_{\text{calibrated}} = C_{\text{measured}} \cdot \left(\Delta S \cdot \frac{Y(z)}{Y(r)}\right)$$
 (5.3)

Using Eq.5.3 and the calibration factors determined in this chapter now allows to calculate the charge for an electron beam spectrum measured in a magnetic spectrometer with given energy calibration, based on the counts / (charge [pC]  $\cdot$  electron energy [MeV]) relation found by Nakamura et al. in Ref.[83].

## **5.1.6** Setup and Installation

The new camera-objective pairs were installed on both magnetic spectrometers on the HTU beamline (before and after the VISA undulator). For every camera, the distance to the Lanex screen z was determined by measuring the FoV (as described in Sec.5.1.1), and applying Eq.5.3. The other parameters ( $\Delta S$ , Y(z) and Y(r)) were included into the post-analysis script for the magnetic spectrometer, in the HTU control system. To utilize the existing energy calibration (at which position electrons of a certain energy will hit the Lanex screen, for a defined magnetic dipole field strength), the relative location of the camera FoV with respect to global spatial references on the magnet had to be quantified. This was enabled by the known relation between the 1 cm FoV markings on the Lanex mount and the global reference coordinates of the magnet.

After accounting for all the effects discussed in this section, the new magnetic spectrometer camera setup and calibration was completed and successfully tested against older reference results during the following high power runs. It enabled better resolution of (due to the doubling of total pixels on the chip) and an over 40% increase in sensitivity to electron beam energy and charge, as well as a higher degree of compatibility with the HTU control system infrastructure. Specifically, reducing the timeout between image acquisition and the duration of image post-analysis, improving overall performance and robustness of the magnetic spectrometer under experimental conditions.

# 5.2 On-shot, non-invasive Pulse Duration Diagnostic

Of the diagnostic capabilities to add to the HTU system, a non-invasive, on-shot pulse duration diagnostic based on a commercial pulse characterization device from Swamp Optics [80] had been considered for a while. Previously, the only way to estimate the pulse duration on target was to scan the compressor grating separation and monitor the plasma light intensity. Practically, the measured trend was only useful to find the grating separation value which corresponds to the shortest pulse duration. To assign a value to this position, the full beam had to be sent out of the compressor chamber to a GRENOUILLE diagnostic, which required venting the system and manually inserting a mirror into the beam path. Furthermore, to keep the beam from experiencing dispersion in the vacuum window and thereby changing the measured pulse duration at this specific compressor setting, the vacuum window had to be removed as well. This prevented the re-evacuation of the system after installing the additional mirror. With the compressor chamber under atmospheric pressure, the beam could not be amplified to full power during the pulse duration measurement, adding further discrepancies between the experimental and measurement conditions. Therefore, despite the tremendous amount of time and work required to set up and align the diagnostic every time, this technique would at best deliver values that could be considered to be a close estimate of the real pulse characteristics. For this reason, there was a strong desire for a permanent diagnostic setup that would deliver more precise values under actual experimental conditions.

In this section, the process of commissioning such a diagnostic will be described in detail. Starting with the considerations leading to the design of the beamline, followed by the first measurements and calculations that informed the choice of optics to set up the diagnostic. The first dedicated effort to commission the diagnostic by assessing its performance with respect to dynamics on target will be explained, and the results of the first measurements after successful commissioning. The observations from these first experiments led to a lengthy investigation into the best way to operate the new diagnostic, and how to extract the parameters giving the most insight into correlations to LPA dynamics. A condensed version of some of the data shown and discussed in this section has been published by the author and can be found in the corresponding supporting publication

**F. Kohrell**, S. K. Barber, K. Jensen, C. Doss., C. Berger, C. B. Schroeder, E. H. Esarey, F. Grüner and J. van Tilborg

Investigation of correlations between spectral phase fluctuations of the laser pulse and the performance of an LPA, Nucl. Instrum. Methods Phys. Res., A 1073 (2025)

### 5.2.1 Design

For the new diagnostic to deliver more insightful results than the existing, invasive technique, it has to be capable of operating under high power experimental conditions, so with a fully amplified beam.

This made it imperative for the system to remain under vacuum. Given the desire for flexibility of the diagnostic setup and to eliminate the need to vent the vacuum system every time

it is to be used, it would have to be placed outside of the vacuum chamber. To avoid having to break the interlock on the radiation cave when working on it, which would be highly disruptive during high power experiments, the diagnostic would have to be placed at a place in the system before the OAP chamber. This led to choosing a location outside of the compressor chamber. It is the earliest possible point in the system to measure the beam after compression, and the last possible point before the beam enters the radiation cave.

Because the chamber has to be under vacuum, the windows have to remain in place. This immediately determined the need for some sort of dispersion correction setup, to re-compress the stretched pulse after passing through the window.

The mirror sending the beam out of the vacuum chamber could technically be mounted on a motorized stage, or otherwise be inserted remotely, but this would make the diagnostic invasive (meaning no beam on target when measuring the pulse duration, and no pulse duration data when running the accelerator). A non-invasive setup would require picking up the leakage behind one of the high-reflective (HR) mirrors, which would add a significant amount of dispersion D2, as introduced in Sec.1.3.1 and Eq.1.13, to the analyzed beam. But because the need for dispersion compensation before the diagnostic had already been established, it seemed like an acceptable trade-off for the gain of pulse duration data on every shot, even during high power accelerator operation.

Based on the considerations discussed above, the decision was made to design a non-invasive system outside of the HTU compressor chamber, able to gather on-shot data during high power operation. Because the location is outside of the radiation controlled area, it would also ensure a high degree of flexibility, due to possibility of adjustments to the diagnostic even during high power operation.

#### **5.2.2** Setup

Similar considerations for a pulse duration diagnostic had been made previously on the Hundred TeraWatt Thomson-Scattering (HTT) beamline, which is based on a very similar setup to HTU (up to the target chamber). A prototype of the adjustable dispersion correction system, based on a chirped mirror compressor and subsequent glass wedge pair for precise tuning of the total dispersion, had been designed. Although not directly transferrable to the HTU setup, it was used as inspiration for the first design of the diagnostic beamline.

The first step was to determine roughly how much dispersion would have to compensated for with the chirped mirror compressor. Given that the diagnostic beam will be the leakage through a 1" thick HR mirror at  $45^{\circ}$ , and a 1/2" thick vacuum window at  $0^{\circ}$ , the total amount of dispersion D2 added to the measured pulse will be approximately

$$D2_{\text{approx}}(800 \,\text{nm}) = 36.163 \,\text{fs}^2/\text{mm} \cdot (\sqrt{2} \cdot 25.4 \,\text{mm} + 12.7 \,\text{mm}) = 1758.28 \,\text{fs}^2$$
 (5.4)

with the refractive index for fused silica at  $800 \,\mathrm{nm}$  being  $36.163 \,\mathrm{fs^2/mm}$  [84].

Because there was a certain amount of uncertainty about the substrate of the HR and window, as well as their exact thickness and incidence angles, the *GRENOUILLE* was installed to measure the duration of the stretched pulse directly. The compressor grating separation had

been set to deliver the shortest possible pulse on target (about 35 fs). Under these conditions, the *GRENOUILLE* measured a pulse duration of 200 fs outside of the OAP chamber, with a FROG Error of below 2% (indicating a less than high-quality retrieval accuracy [37], see Sec.5.2.3 for more detailed discussion).

Assuming the case of a bandwidth limited Gaussian pulse, it can be calculated how much second order dispersion (GDD)  $D2(\omega)$  is necessary to stretch a compressed pulse of length  $\tau_0$  to a certain pulse length measured on our diagnostic line  $\tau_m$ , using the following equation [85]:

$$\tau_m = \tau_0 \sqrt{1 + \frac{(4 \ln 2 \cdot D2(\omega))^2}{\tau_0^4}}$$
 (5.5)

or

$$D2(\omega) = \frac{\tau_0^2 \sqrt{(\frac{\tau_m}{\tau_0})^2 - 1}}{4 \cdot \ln 2}$$
 (5.6)

For a compressed pulse of  $\tau_0 = 35 \,\text{fs}$ , and a measured pulse length of  $\tau_m = 200 \,\text{fs}$ , Eq.5.6 delivers  $D2_{\text{meas}}(\omega) = 2485.76 \,\text{fs}^2$ .

The fact that the two results  $D2_{\text{meas}}$  and  $D2_{\text{approx}}$  deviate by about  $700 \,\text{fs}^2$  indicates that either the assumptions made for the calculation of  $D2_{\text{approx}}$  were significantly off, or that the pulse duration retrieval for such a significantly stretched pulse in the *Swamp Optics* software is inaccurate (supported by the FROG error exceeding 1% [37]). The safest way forward was to assume the larger of the two values, overcompensation with negative GDD through chirped mirrors can always be compensated easily by adding more glass into the beam path.

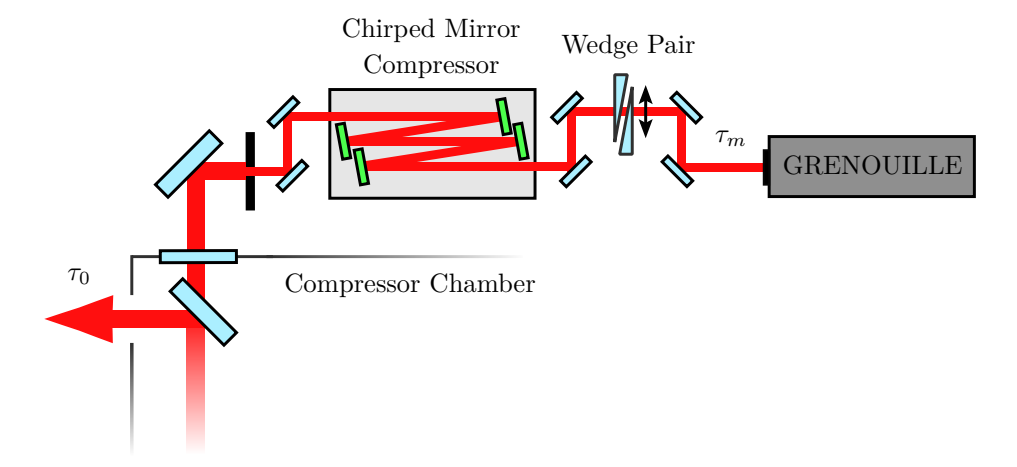


Figure 12: Schematic of the non-invasive, on-shot pulse duration diagnostic setup installed on the HTU beamline. The leakage of the main beam (compressed pulse duration  $\tau_0$ ) through the last high reflection optic in the compressor chamber gets transmitted out of the vacuum system and picks up significant positive GDD in the process. To compress the pulse before detection, a chirped mirror compressor overcompensates the accumulated GDD, and a pair of glass wedges can be used to fine-tune ideal compression. Finally, the diagnostic beam with the pulse duration  $\tau_m$  is sent to the GRENOUILLE, a commercial pulse characterization diagnostic from Swamp Optics [80].

Assuming the need to compensate a GDD of at least  $D2_{\text{meas}}(\omega) = 2485.76 \,\text{fs}^2$ , the choice was made to procure four HD2012 dispersive mirrors from *UltraFast Innovations* [86], providing

700 fs<sup>2</sup> per bounce, for a total overcompensation of about -300 fs<sup>2</sup>. A pair of glass wedges after the chirped mirror compressor was included in the design, to enable fine adjustments of the total dispersion on the beamline, and ability to ideally compress the pulse before the *GRENOUILLE*. With all the required components, the on-shot, non-invasive pulse duration diagnostic was set up, as can be seen schematically in Fig.12.

Because the beam coming out of the compressor chamber is  $\sim 10\,\mathrm{cm}$  in diameter and the GRENOUILLE has a much smaller acceptance, an iris was used to down-size the beam to about 5 mm. Due to space constraints and to avoid further GDD pick-up, reducing the beam size via an iris instead of a telescope was chosen. Even when using the iris to reduce the beam size, the intensity of the amplified pulse on the diagnostic line was still high enough to saturate the GRENOUILLE camera, another reason why down-collimating the full beam was not considered going forward.

### **5.2.3** Commissioning

After the setup was completed and aligned, first measurements at high power were conducted with the goal to experimentally determine the setting of the wedge pair in the diagnostic beam path, necessary to compensate for the excess in negative GDD added by the chirped mirror compressor. In its initial configuration, for the compressor grating separation that delivered the shortest pulse on target, about  $\tau_m = 60 \, \text{fs}$  were measured on the diagnostic line. However, during that same week undulator radiation was observed for the very first time on the HTU system, which shifted the focus away from the time consuming process of dialing in compression for the *GRENOUILLE*. When returning to this issue about three months later, *GRENOUILLE* data had been taken during most high power runs in the meantime, in the stretched  $\tau_m \neq \tau_0$  configuration.

The only way on the HTU system to ensure the measured pulse duration  $\tau_m$  and the pulse duration on target  $\tau_0$  match, is to perform a compressor grating separation scan and afterwards analyze the trend of the plasma light on target (picked up by a top view camera installed outside the target chamber) and the pulse duration measured by the *GRENOUILLE*. Because the shortest pulse (highest intensity) will produce the brightest plasma emission [87, 88], the grating separation value corresponding to this observation will have to match the shortest pulse duration measured by the *GRENOUILLE*.

When optimizing for compression on the diagnostic line, adding neutral density (ND) filters to keep the pulse from saturating the GRENOUILLE camera close to compression, as well as optimizing the wedge pair position, eventually led to matching results of  $\tau_0$  and  $\tau_m$ , as can be seen from the plot in Fig13. Based on Eq.5.4, the amount of added material corresponds to a GDD value of  $D2_{\rm added} \approx 568\,{\rm fs}^2$ . Assuming perfect pulse compression at the location of the GRENOUILLE, and considering that the chirped mirrors add  $-2800\,{\rm fs}^2$ , this puts the total amount of positive GDD on the diagnostic line at about  $2232\,{\rm fs}^2$ . This value lies within the interval calculated in Sec.5.2.2, and confirms that both methods used to estimate the amount of GDD added to the pulse by leaking through the HR and vacuum window were rather inaccurate. But choosing to overcompensate for the more extreme of the two values did allow for achieving ideal compression as planned.

As described above, maximizing the plasma light emission detected by the top view camera, located outside the target chamber, is the method used on HTU to determine when the pulse

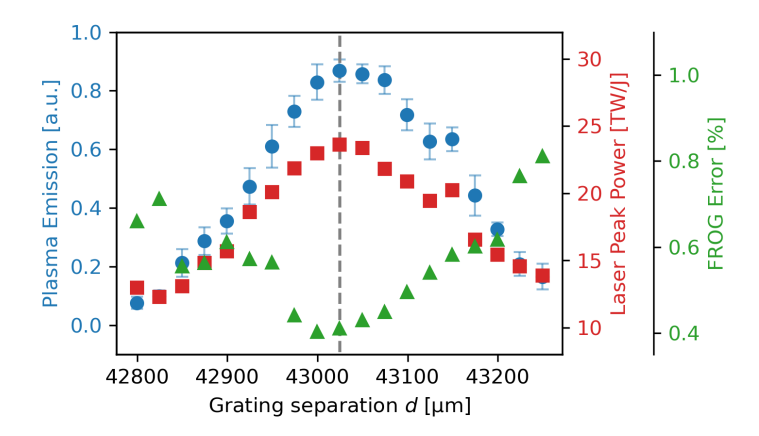


Figure 13: The first scan showing good overlap between the pulse duration on target and the diagnostic line. The blue curve shows the mean counts as detected by the camera looking at the plasma light on target (used as the proxy for pulse duration on target). The red curve shows the peak power parameter, as calculated from the GRENOUILLE data (representing the pulse duration measured on the diagnostic line). The FROG Error (green) is a measure of the accuracy of the FROG retrieval.

duration on target is the shortest. In the compressor grating separation scan displayed in Fig. 13, a good overlap was achieved between the peak plasma emission and the shortest pulse duration measured by the GRENOUILLE (represented by the "Laser Peak Power [TW/J]" parameter). This parameter is defined as "energy normalized peak power"  $P_E(t)$ , and has been proven a helpful metric when assessing the quality of compression and pulse contrast by Nakamura et al. in Ref.[89]. The value is determined by normalizing the instantaneous power of the laser with the total pulse energy. In addition to simply connecting pulse duration and pulse energy, it includes information about femtosecond level pre-pulses, and how much of the pulse energy is contained within the main pulse, making it an effective measure for the overall quality of the pulse [89].

Because the grating separation scan only changes pulse compression and not the pulse contrast, in this case  $P_E(t)$  is simply a measure of the pulse duration  $\tau_m$  on the diagnostic line, and the compressor position delivering the highest peak power value corresponds to the shortest pulse duration.

The uncertainty of the FROG retrieval algorithm ("Frog Error" in Fig.13), also displays a minimum at the compressor position corresponding to the highest "peak power [TW/J]" value (shortest pulse duration). This behavior was to be expected, because the FROG error is defined as the rms difference between the measured and retrieved FROG trace, and scales with the square-root of the laser pulses time-bandwidth product (TBP) [37]. This causes the retrieval process to become less accurate with increasing pulse duration. However, even at the edge of the parameter range during this scan, the FROG error was below 1%, which is the value given by Trebino et al. [37] as the limit for a high-quality retrieval.

With the diagnostic line set up to deliver results matching the pulse on target, it was ready to be actively included into the HTU system going forward.

# 5.2.4 First Results

After successfully commissioning the diagnostic, an effort was made to analyze all the previously taken data. This included the datasets acquired during the first observations of undulator radiation, for which the dispersion on the diagnostic line had not yet been ideally compensated. The hope was to nevertheless find correlations between the measured pulse duration  $\tau_m$  and the LPA and FEL parameters. Data from the noscan (scan under static experimental conditions, no parameter is being scanned) on 04/20/2023 showing the highest amount of undulator signal is displayed in Fig.14, next to the data from the first noscan with undulator light after dispersion matching on the *GRENOUILLE* setup, on 07/27/2023.

Important to note is that the pulse duration on target  $\tau_0$  is always compressed to its bandwidth-limited duration for all the experiments discussed going forward. Only the diagnostic pulse  $\tau_m$  is experiencing changes in compression, as the dispersion correction of the *GRENOUILLE* setup is manipulated.

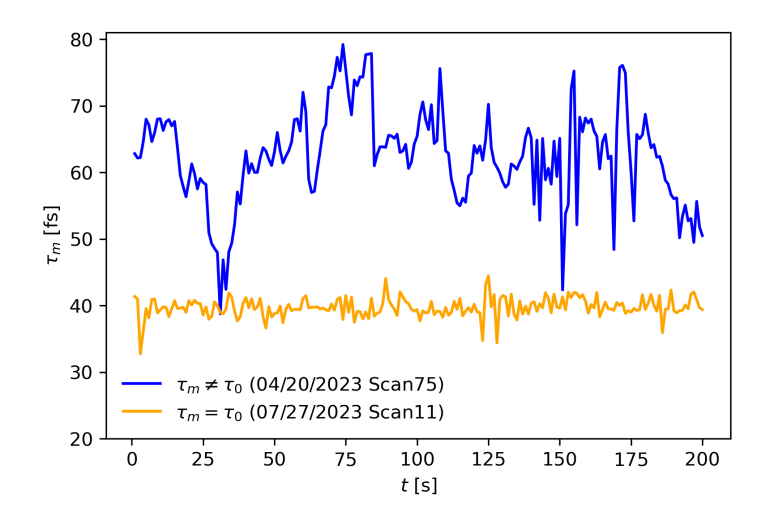


Figure 14: Comparing the pulse duration stability during a 200 shot noscan recording undulator radiation, taken at 1 Hz. The blue curve shows the pulse duration when not ideally compressed on the diagnostic line  $(\tau_m \neq \tau_0)$ . The orange curve shows the pulse duration after ideally compressing the diagnostic beam  $(\tau_m = \tau_0)$ .

As can be seen from the plot in Fig.14, the "stretched" pulse ( $\tau_m \neq \tau_0$ ) exhibits strong instabilities, in the form of systematic variations (not just shot-to-shot) with an amplitude of about  $\pm 15$  fs around the mean pulse duration of about 60 fs. Another important observation is that the timescale of these variations is on the order of tens of seconds. In comparison, the compressed pulse seems to show no such significant instabilities beyond shot-to-shot fluctuations. To quantify the difference in stability, the mean and rms values for both datasets were calculated:

- 04/20/2023 Scan75:  $\tau_m = 62.56 \pm 7.09$  fs
- 07/27/2023 Scan11:  $\tau_m = 39.75 \pm 1.44$  fs

To rule out a faulty post-retrieval or temporary instability, all pulse duration data taken before the dispersion compensation on 07/13/2023 (see Fig.13) was analyzed and compared. The results show the same behavior, and seem to indicate the effect to be a real dynamic of the laser system, only resolved when the diagnostic pulse  $\tau_m$  is stretched with respect to the pulse on

target  $\tau_0$ .

To investigate if this effect is originating on the diagnostic line, or indeed inherent to the main beam on target, an effort was made to find correlations of the measured pulse duration  $\tau_m$  to LPA parameters. Finding such a correlation would indicate the observed behavior to be affecting the pulse on target, and therefore the LPA process. The first parameter investigated was the electron bunch charge measured by the ICT upstream of the VISA undulator. The correlation plots for both scans can be seen in Fig.15.

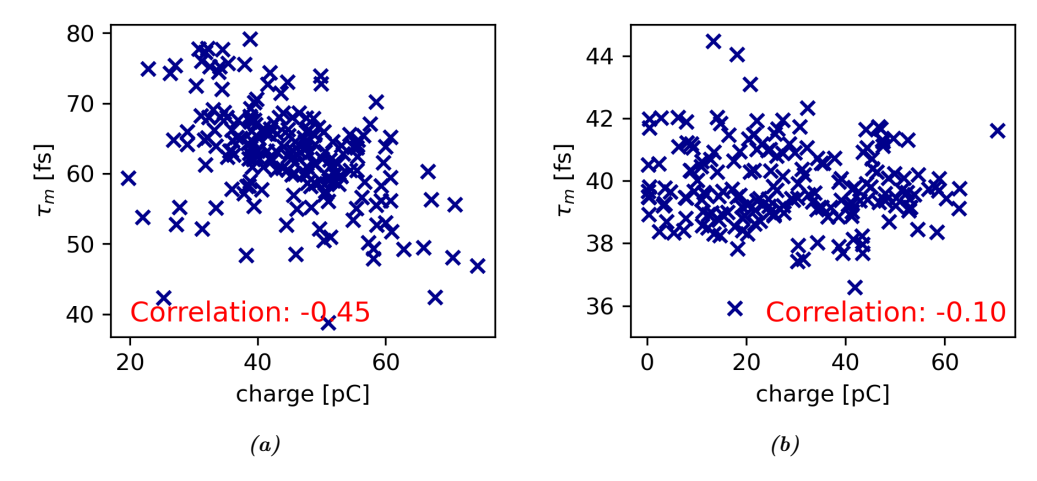


Figure 15: Correlation of laser pulse duration  $\tau_m$  as measured by the *GRENOUILLE* and the charge measured by the ICT before the VISA undulator. (a): 04/20/2023 Scan75. (b): 07/27/2023 Scan11. In both cases, the pulse on target is compressed to  $\tau_0 \approx 40 \, \mathrm{fs}$ .

Fig.15(a) shows a noticeable Pearson correlation of  $\rho = -0.45$  between pulse duration and charge for the stretched pulse on the diagnostic line ( $\tau_m \neq \tau_0$ ), which seems to indicate higher generated charge for shorter pulse durations. Of course, the fact that only the pulse on the diagnostic line is stretched, and the pulse on target still compressed, makes interpreting this correlation less trivial. Technically, the shortest pulse on target should correspond to  $\tau_m \approx 62$  fs, as discussed above. Any changes in pulse duration on target, assuming bandwidth limited compression, could only cause the pulse duration to get longer, which would decrease the generated charge. For the stretched pulse correlation, displayed in Fig.15(a), this should lead to a decrease in measured charge for pulses both longer and shorter than 62 fs. It seems that the vast majority of data points are right around or above 60 fs, and their behavior seems to match the above explained expectations. For the pulses shorter than 60 fs, there are not enough data points to see a clear correlation. But it is important to note that a simple correlation of "shorter pulse duration = higher charge" is not to be expected for this configuration.

In the case of the pulse detected by the *GRENOUILLE* being compressed to match the pulse on target ( $\tau_m = \tau_0$ , Fig.15(b)), the situation is very different than what was discussed above for the stretched case. Now one would expect a clear correlation, shorter pulses on the diagnostic line should correspond to shorter pulses on target, and the same for longer pulses. But a correlation factor of  $\rho = -0.1$  is too low to confidently claim there is a real correlation being observed.

Given that a clear correlation between pulse duration and charge is observed in the stretched configuration of Scan75, but not in the compressed case of Scan11, these results seem to strongly

indicate that the observed differences in pulse duration fluctuations between the two scans are not just an artifact on the diagnostic line, but have a real connection to the laser system and LPA interaction. It appears that whatever systematic fluctuations are affecting the laser pulse can only be resolved when the diagnostic pulse is stretched with respect to the pulse on target.

To try and further support the hypothesis that the fluctuations of  $\tau_m$  in the stretched case, seen in Fig.14, are based on real behavior of the compressed pulse on target  $\tau_0$ , simulations were conducted based on the statistics displayed in Tab.2. The goal is to show that starting from a compressed pulse with the experimentally measured rms jitter of Scan11, simply adding a fixed amount of dispersion will lead to an increase in pulse duration jitter matching what was observed experimentally in Fig.14 for Scan75.

For this purpose, a random array of 100 pulses was generated, matching the statistics of the compressed case in Scan11, based on the assumption that the changes in pulse duration are solely caused by spectral phase jitter. Using Eq.5.6, the amount of GDD (linear spectral phase) needed to stretch the pulse from 39.75 fs to 62.56 fs was calculated to be 691.5 fs<sup>2</sup>. This result was now utilized to stretch every pulse in the array by this fixed value, and calculated the corresponding pulse durations. The result can be seen in Fig.16.

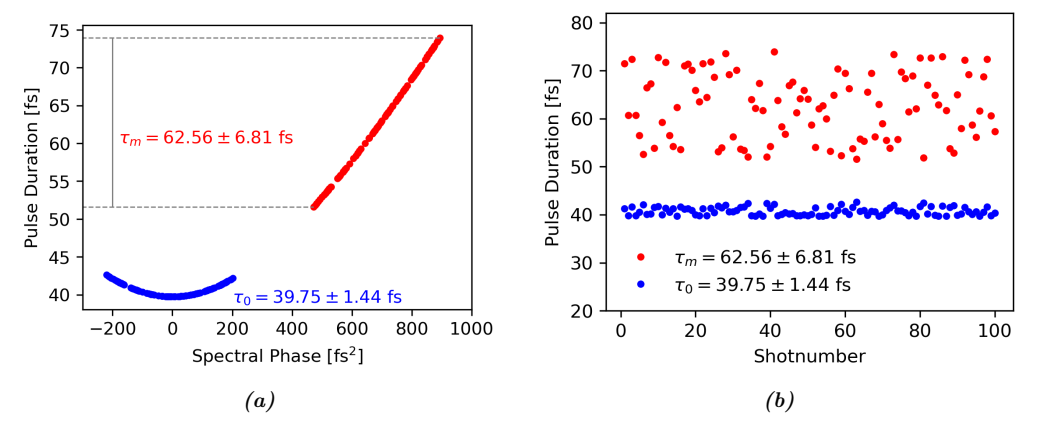


Figure 16: Displaying the statistics of 100 simulated laser shots, assuming only a change by a fixed amount of spectral phase (GDD) between the compressed (blue) and stretched (red) case. Plotted is the pulse duration over the (a) spectral phase and (b) shotnumber.

Fig.16(a) shows the quadratic dependence between pulse duration and linear spectral phase (or GDD). The compressed pulses (simulating the results from Scan11), with an amount of random spectral phase fluctuations causing the measured pulse duration rms shown in Tab.2, is displayed in blue. The same array of pulses, after adding a fixed amount of 691.5 fs<sup>2</sup> to each data point, is displayed in red. As can be clearly seen in the plot, both data sets lie on the same parabolic curve, the stretched array was merely "shifted" to higher spectral phase values. Due to the nonlinear trend of the relation between pulse duration and spectral phase (Eq.5.5), the identical rms jitter in spectral phase (about  $\pm 200 \, \mathrm{fs^2}$ ) causes significantly larger rms jitter in pulse duration for a stretched pulse. Comparing the statistics of the measured and simulated stretched pulses, as shown in Tab.2, the almost perfect reproduction of the observed pulse duration rms jitter seems to validate the assumptions made for this simulation.

Fig.16(b) shows the shot-to-shot behavior of the two simulated datasets. The displayed intervals visualize how a small, systematic change in spectral phase could translate into the strong variations observed in Fig.14.

	$\bar{\tau}_m$ [fs]	$\operatorname{rms}(\bar{\tau}_m)$ [fs]
Scan11	39.75	1.44
Scan75 (exp)	62.56	7.09
Scan75 (sim)	62.56	6.81

**Table 2:** Measured mean and rms values of  $\tau_m$  for both datasets displayed in Fig.14, as well as statistics of the simulated stretched pulse shown in Fig.16.

After analyzing the above displayed and discussed results, it seemed highly probable that the variations observed when measuring the stretched pulse on the diagnostic line are not just based on a real variation of spectral phase in the main laser pulse, but also that it might be desirable to operate the diagnostic in this stretched configuration. Fig.15 suggests that, due to the nonlinear relation between the spectral phase and pulse duration, the stretched configuration is more sensitive to small variations in spectral phase of the main laser pulse. These variations have been shown to impact LPA (as well as potentially FEL) parameters, and apparently can not be resolved in the compressed configuration.

This observation led to

- 1. The desire to develop a custom post-retrieval routine, designed to specifically analyze linear spectral phase (GDD) changes in the measured laser pulses, to correlate to LPA and FEL performance.
- 2. The decision to purposefully de-tune the dispersion compensation on the *GRENOUILLE* line, with the goal of operating in the seemingly more sensitive regime.
- 3. The question of where these instabilities are originating from, and if or how they can eventually be mitigated.

### **5.2.5** Linear Chirp Retrieval and Characterization

This chapter will focus on the development and optimization of a custom post-analysis routine to directly analyze the linear chirp variations of the laser pulse.

To extract the linear chirp dynamics from the *GRENOUILLE* data, the raw images as saved by the device first need to be analyzed. An in-house developed *LabView* script, based on the retrieval algorithm by Trebino et al. [37], optimizes spectral amplitude and phase traces by minimizing the "FROG error", which quantifies the discrepancy between the measured and simulated *GRENOUILLE* image. The simulated, or "retrieved", image is then calculated based on the generated spectral amplitude and phase traces. By selecting a "retrieval time", the user can determine how long to let the program run through the loop of changing the simulated pulse to try and minimize the FROG error. If not otherwise specified, all the *GRENOUILLE* data discussed in this thesis was calculated using a retrieval time of 30 s, to ensure a low error in the retrieved traces. However, such a long retrieval time per single image means this analysis can not provide real-time results for a parameter scan. The raw data is being taken on every shot,

but the results take hours to calculate.

With the spectral amplitude and phase traces for the data retrieved, as can be seen in Fig.17(a), an even-order polynomial in the form of Eq.5.7 can be fitted to the spectral phase  $\Phi(\omega)$  to extract the linear chirp parameter,  $\beta$  in Eq.5.7 (see Sec.1.3.1).

$$\underline{\Phi(\omega) = C + \alpha\omega + \beta\omega^{2} + \gamma\omega^{3} + \delta\omega^{4} + \varepsilon\omega^{5} + \zeta\omega^{6}}_{\text{2nd Order Fit}}$$
(5.7)

When looking at the spectral phase trace in Fig.17(a), it immediately becomes clear that a specified interval, based on the spectral amplitude of the laser pulse, has to be chosen for the polynomial fit. As to be expected (because the phase is undefined where the intensity is 0 [37]), for spectral amplitude values close to 0, the uncertainty of the spectral phase retrieval increases significantly, which can be seen by the strong variations observed outside the grey shaded area in Fig.17a)

Multiple different options were implemented and evaluated based on their ability to reproduce the expected trend of the linear chirp parameter  $\beta$  during a compressor grating separation scan. A combined approach was ultimately chosen, restricting the part of the spectrum to be analyzed to a fixed wavelength range  $840\,\mathrm{nm} > \lambda > 760\,\mathrm{nm}$ . This interval is defined through the center wavelength of the laser pulse  $\lambda_0 = 800\,\mathrm{nm}$ , and accounts for the expected width of the spectrum and potential fluctuations. An additional condition was added, of only fitting the spectral phase where the spectral amplitude value is larger than a chosen "Spectral Amplitude Threshold" (SAT) value, to limit the fit to a region of low retrieval error (as discussed above). A more detailed investigation and discussion of the impact of this SAT value on the results of the polynomial fits can be found in the appendix, Sec.10.1.

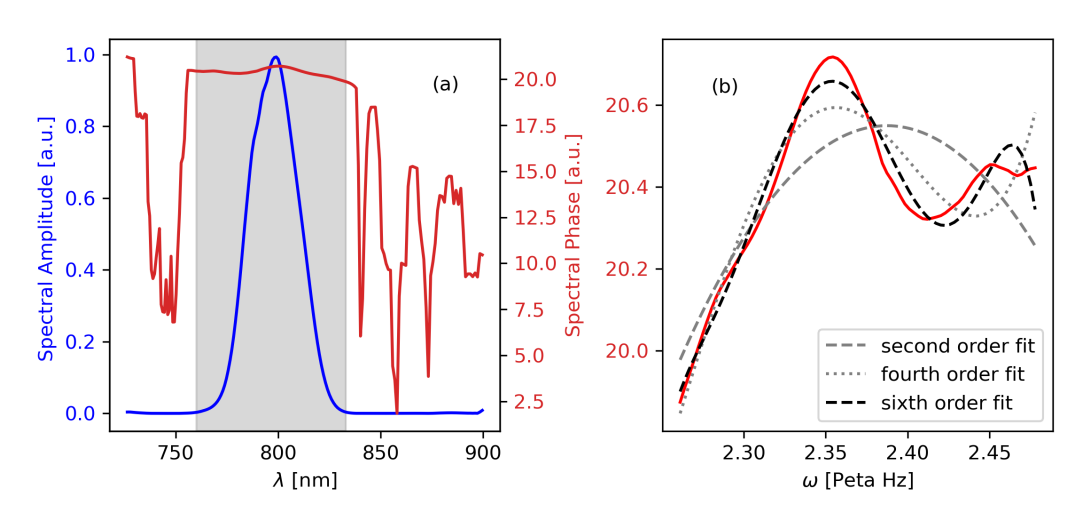


Figure 17: (a): Averaged spectral amplitude and phase of 20 consecutive laser pulses, retrieved from the raw images taken by the non-invasive GRENOUILLE setup. The shaded area represents the wavelength interval defined by  $840 \,\mathrm{nm} < \lambda < 760 \,\mathrm{nm}$  and the spectral amplitude threshold (SAT) > 0.003.

(b): Averaged spectral phase over the frequency interval corresponding to the shaded interval in (a). Polynomials of three different orders, as introduced in Eq.5.7, have been fitted to the spectral phase curve.

The wavelength interval which satisfies both above described conditions can be seen as the shaded area in Fig.17(a). It is then transferred from the wavelength to the frequency domain to fit the  $\Phi(\omega)$  polynomial and retrieve the linear chirp parameter, as can be seen in Fig.17(b).

To conduct detailed studies of the linear chirp parameter retrieval, dedicated compressor scans were taken at low laser power. The significant decrease in signal intensity on the *GRENOUILLE* diagnostic line required increasing the exposure time of its internal cameras from 1 ms to 850 ms. This enabled data acquisition at 1 Hz, but the saved images represent averages over 850 consecutive low power pulses (at 1 kHz repetition rate), instead of just one high power pulse (1 Hz repetition rate).

Because the *GRENOUILLE* is based on the second-harmonic generation (SHG) frequency-resolved optical gating (FROG) process the direction of time in the acquired images, and therefore in the retrieved traces, is ambiguous [37, 40]. This uncertainty about possible time reversal of the retrieved data with respect to the real pulse makes the sign of the linear chirp parameter ambiguous. The SHG FROG image of an up- versus down-chirped pulse of same duration and spectrum is identical. It is crucial to account for this uncertainty of the sign of the linear chirp parameter in the analysis going forward, to avoid misinterpretation.

Owing to this ambiguity, the spectral phase traces are being analyzed as such:

- 1. Fit the polynomial to each individual spectral phase trace in the chosen interval (see Fig.17(a))
- 2. Extract the linear chirp parameter  $\beta$  from the fit parameters and take its absolute value, to eliminate errors based on uncertainty of its sign (SHG FROG, discussed above)
- 3. Average the absolute  $\beta$  values over the batch of shots taken at the same compressor position d

The result for a compressor scan conducted on 01/29/2024 can be seen below in Fig.18. Twenty images were taken at each grating position d, and the three polynomials fitted to each spectral phase trace in the interval defined by the spectral range of  $840\,\mathrm{nm} > \lambda > 760\,\mathrm{nm}$  and SAT > 0.003, as in Fig.17. Uncertainties for each calculated parameter are returned by the fit as well. The averaged, absolute linear chirp values  $\bar{\beta}$  and errors were normalized to simplify comparing their trends during the compressor scan between the different polynomial orders.

The pair of parallel gratings in the compressor impose negative linear chirp on the transmitted pulse and the total amount scales linearly with the grating separation d [85, 90].

The  $\bar{\beta}(d)$  trend from the 2<sup>nd</sup> and 4<sup>th</sup> order polynomial retrieval displayed in Fig.18 seems to qualitatively match this expectation of change in GDD with increasing grating separation. Once the values get close to  $\bar{\beta}=0$ , it seems that the linear trend is "reflected" from the x-axis. This is to be expected, due to the fact that the absolutes of the  $\beta$  values are being averaged, explaining the loss of information about their sign. Following the theoretical expectation, a manual sign-flip will be implemented later, to enable a linear fit to the entire dataset.

The values extracted from the 6<sup>th</sup> order polynomial fit, however, show a seemingly completely uncorrelated trend.

The connection between polynomial order, SAT value and quality of the  $\bar{\beta}$  trend were investigated in detail and can be found in the Appendix, Sec.10.1.

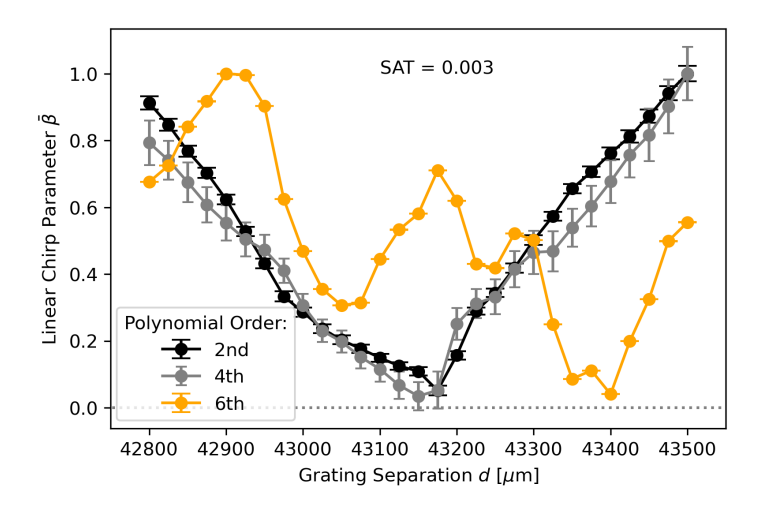


Figure 18: Change in normalized, absolute linear chirp parameter  $\bar{\beta}$  of the low power laser pulse with the compressor grating separation d. Polynomial fits of three different orders were used to extract  $\bar{\beta}$  from the spectral phase, and the behavior of the different chirp parameters are being compared. The spectral phase traces fitted were retrieved from SHG FROG images taken on the HTU GRENOUILLE diagnostic line.

Because, at least for the 4<sup>th</sup> order polynomial, there seems to be a direct correlation between accuracy of reproducing the expected  $\bar{\beta}(d)$  trend and the SAT value, it makes sense to look back at Fig.17. The data displayed here was taken at the grating separation position  $d=43\,175\,\mu\mathrm{m}$ , which, in Fig.18, appears to be the closest value to  $d_0$ , the grating position corresponding to ideal pulse compression. The seemingly flat spectral phase in the region of  $I(\lambda) > 0$ , as can be seen in Fig.17(a), supports this observation. Zooming in on it in Fig.17(b) and comparing the three different fits, it becomes apparent why cropping the spectral phase interval further would drastically change the  $\beta$  values returned by the 4<sup>th</sup> and 6<sup>th</sup> order polynomials. They are much more sensitive to deviations from an idealized parabolic trend of the spectral phase than the 2<sup>nd</sup> order fit. And, because with increasing polynomial order the second order term has decreasing effect on the overall curve shape, the expected sensitivity of  $\beta$  to small changes in the fitted spectral phase curve increases as well. The less sensitive the polynomial function is to changes of  $\beta$ , the more  $\beta$  can deviate from the expected linear trend when varying d, while the polynomial fit still accurately represents the spectral phase curve. This explains the complete mismatch between the  $\bar{\beta}(d)$  trend from the 6<sup>th</sup> order polynomial fits, despite the good overlap between the polynomial and spectral phase trace, as shown in Fig.17(b).

It was desirable to have the potential for investigation of higher order spectral phase effects, for which the  $2^{\rm nd}$  order fit provides no information. Because of this reason, and the fact that the  $\bar{\beta}(d)$  trend from the  $4^{\rm th}$  order polynomial fit reproduces the expected linear chirp behavior seemingly as well as the  $2^{\rm nd}$  order (for values of SAT < 0.01), the choice was made to use the  $4^{\rm th}$  order polynomial retrieval going forward.

Utilizing the above discussed technique and findings, the data for the same compressor scan was used to try and extract a value usable to benchmark the retrieval performance against experimental results. The grating separation position  $d_0$  was chosen, which corresponds to

the compressor setting delivering the shortest measured pulse duration. To extract  $d_0$  from the linear chirp data taken during this compressor scan, the absolute, averaged linear chirp parameter  $\bar{\beta}$  is calculated as discussed above. Then, a sign-flip is introduced at the grating separation exhibiting the smallest  $\bar{\beta}$  value. This enables the addition of a linear fit according to Eq.5.8 to the entire dataset, as can be seen in Fig.19.

$$\bar{\beta} = a \cdot d + b \tag{5.8}$$

$$\Longrightarrow d(\bar{\beta} = 0) = d_0 = -\frac{b}{a} \tag{5.9}$$

Using the returned linear fit parameters, as shown in Eq.5.9, the theoretical value for  $d_0$  was calculated to be  $d_0 = 43\,127.40\,\mu\text{m}$ . Before making a final statement of how well this value matches our experimental results, its uncertainty should be calculated.

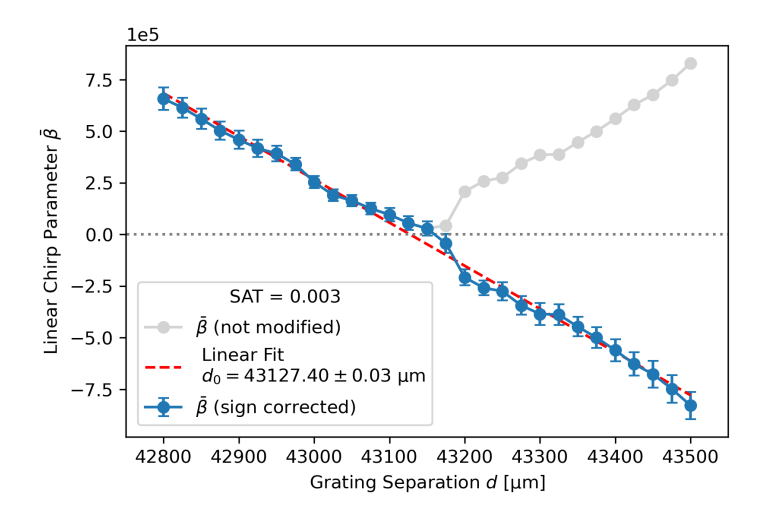


Figure 19: Averaged absolute linear chirp parameter  $\bar{\beta}$  trend during compressor grating separation scan (grey).  $\bar{\beta}$  was retrieved from the spectral phase data using a 4<sup>th</sup> order polynomial fit. A manual sign-flip is implemented (blue) to enable a linear fit of the whole dataset.  $1/\Delta\bar{\beta}$  (uncertainties for  $\bar{\beta}$ ) are used as weights for the linear fit (red dashed line), and its intersection with the x-axis is calculated to compare the  $d_0$  value to experimental findings.

The uncertainty for  $d_0$  was determined based on the errors returned for the linear fit parameters and the "propagation of uncertainty" method, as can be seen below:

$$d_0 = -\frac{b}{a} \quad \left| \frac{d}{dx} \right|$$

$$\Delta d_0 = -\frac{d}{dx} \left( \frac{b}{a} \right)$$

$$= d_0 \left( \frac{\Delta b}{b} - \frac{\Delta a}{a} \right)$$

This method delivered an error for  $d_0$  of  $\Delta d_0 = 0.034 \,\mu\text{m}$ . Because this error is so small compared to  $d_0$ , the result was verified by calculating the maximum error, which offers the most conservative way to determine parameter uncertainty:

$$\Delta d_0' = \frac{d_{0,max} - d_{0,min}}{2}$$

$$= \frac{1}{2} \left( \frac{b_{max}}{a_{min}} - \frac{b_{min}}{a_{max}} \right)$$

$$= \frac{1}{2} \left( \frac{b + \Delta b}{a - \Delta a} - \frac{b - \Delta b}{a + \Delta a} \right)$$

Even using this conservative approach, the error matches the previous result,  $\Delta d_0' = 0.034 \,\mu\text{m}$ , leading to the theoretically retrieved grating separation position corresponding to ideal compression of the laser pulse  $d_0 = 43127.40 \pm 0.03 \,\mu\text{m}$ .

To now quantify the level of accuracy with which the spectral phase retrieval reproduces the behavior of the measured pulse, it was compared to the *GRENOUILLE* data taken during the same scan. For the extraction of the grating separation position  $d_0$  directly from the retrieved traces, the pulse duration  $\tau_m$  of the pulse on the diagnostic line was plotted over the grating separation d, as can be seen in Fig.20.

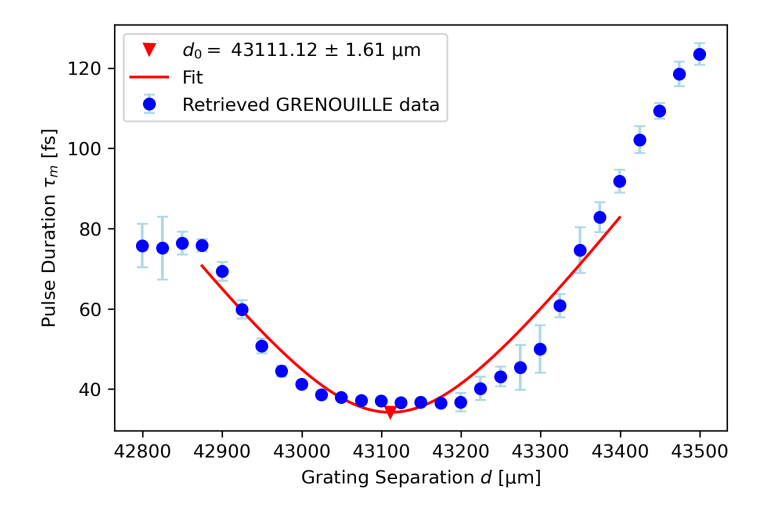


Figure 20: Pulse duration  $\tau_m$  of the pulse measured on the diagnostic line over compressor grating separation d.  $\tau_m$  is calculated from the retrieved 20 GRENOUILLE images per step of d, the average value and standard deviation are displayed. A custom fit to the data in the interval [42875,43400]  $\mu$ m, based on Eq.5.10, was performed to estimate  $d_0$ .

Because the trend of the averaged pulse duration  $\tau_m$  does not clearly reveal the compressor position delivering the shortest pulse, a custom function  $\tau_{fit}(d)$  was fit to the data. This fit is based on Eq.5.5, due to the linear scaling of grating separation d and the dispersion D2 imposed on the laser pulse [85, 90], as well as the correlation between  $\tau_m$  and D2 (see Eq.5.5). After accounting for the fact that D2 = 0 is valid for  $d = d_0$ , one can define the simplified relation

$$D2 = C \cdot (d - d_0)$$

Substituting this in Eq.5.5 leads to the modified equation below, which was used to fit the experimentally determined trend of  $\tau_m$ , as displayed in Fig.20.

$$\tau_m(d) = \tau_0 \sqrt{1 + \frac{(\tilde{C} \cdot (d - d_0))^2}{\tau_0^4}}$$
 (5.10)

The lower interval boundary of 42 875  $\mu$ m was chosen to avoid including data that strongly deviates from the expected trend and is exhibiting especially high uncertainty. As in Fig.19, the fit used 1 / the standard deviation of the pulse duration  $(1/\Delta \tau_m)$  as weights, and, because  $d_0$  is one of the fit parameters in this custom equation, the function returns the uncertainty for it directly.

The custom fit function returns  $d_0 = 43111.12 \pm 1.61 \,\mu\text{m}$ , which deviates from the value determined by the linear fit in Fig.19 by only 16.28  $\mu\text{m}$ . This strongly suggests a high accuracy of the linear chirp parameter  $\bar{\beta}$  retrieval, especially because the step size during compressor scans on the HTU system is set to 25  $\mu\text{m}$ . Therefore, to experimentally determine with high confidence which of the two values is more accurate, the resolution chosen to optimize the compressor position would need to be doubled. Under the current experimental conditions, the difference between the two calculated values for  $d_0$  can effectively be considered to be negligible.

These results have established the linear chirp calculation, which is based on the  $4^{\rm th}$  order polynomial fit to the spectral phase curve retrieved from the *GRENOUILLE* images, as a reliable method to reproduce the behavior of dynamics of the laser pulse. The  $4^{\rm th}$  order fit was chosen to extract additional information on higher order chirp terms. To compare the behavior of the already analyzed  $\beta$  to the higher order chirp terms  $\gamma$  and  $\delta$  (see Eq.5.7), the data from the same compressor scan as focused on in the rest of this chapter is plotted below in Fig.21.

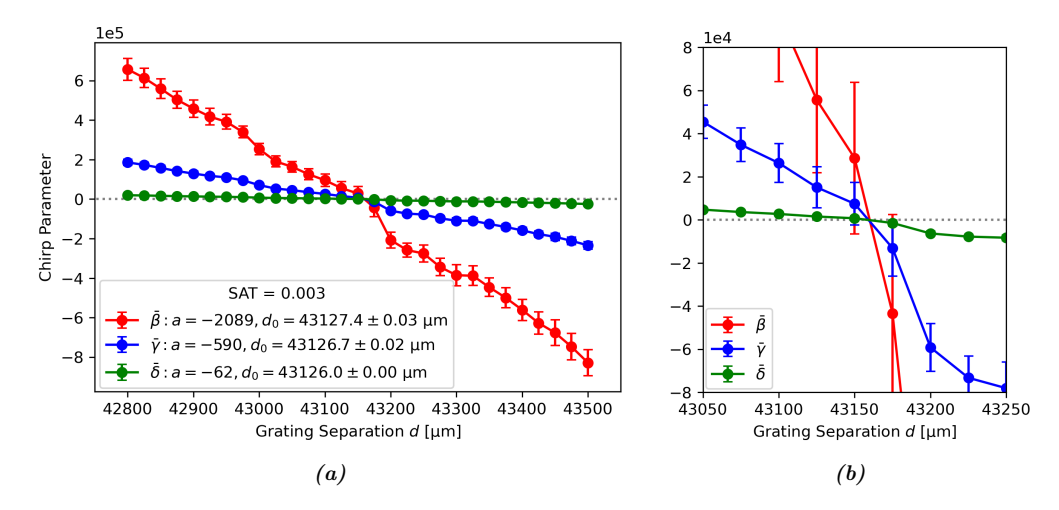


Figure 21: Displaying the dynamics of linear and two higher order chirp terms during a compressor grating separation scan. The values were calculated from the spectral phase traces recoded by the *GRENOUILLE*, as for Fig.19 and discussed extensively in this chapter.

(a): Linear trends were fitted to each parameter data set, to extract the values and uncertainties of  $d_0$ , where each chirp term is minimized. a is the scaling factor for each linear fit  $(y = a \cdot d + b)$ 

(b): A zoomed in view of (a), to visualize the difference in scaling of the different order chirp parameters when changing the grating separation, as well as the quality of overlap between their respective  $d_0$  values.

As can be seen in Fig.21(a), when applying the same technique as discussed for the analysis of Fig.19, the three parameters all exhibit seemingly clean linear trends. Immediately noticeable is the significant difference of the scaling factor a. Some of this effect can be explained by accounting for the  $\frac{1}{n!}$  factor of the Taylor series, which was included into the chirp parameters in Eq.5.7. Correcting for this would result in

• 
$$\bar{\beta} = \frac{1}{11}\bar{\beta}_{\text{Taylor}} \implies \bar{\beta}_{\text{Taylor}} = \bar{\beta} \implies a_{\text{Taylor}}(\bar{\beta}) = a(\bar{\beta}) = -2089$$

• 
$$\bar{\gamma} = \frac{1}{2!} \bar{\gamma}_{\text{Taylor}} \implies \bar{\gamma}_{\text{Taylor}} = 2\bar{\gamma} \implies a_{\text{Taylor}}(\bar{\gamma}) = 2a(\bar{\gamma}) = -1180$$

• 
$$\bar{\delta} = \frac{1}{3!} \bar{\delta}_{\text{Taylor}} \implies \bar{\delta}_{\text{Taylor}} = 6\bar{\delta} \implies a_{\text{Taylor}}(\bar{\delta}) = 6a(\bar{\delta}) = -372$$

Even when accounting for this, the difference in scaling remains significant, and the second order (linear) chirp parameter is still affected most strongly when varying the compressor grating separation. The fact that the other, higher order parameters are also changing with d, immediately begged the question if they can all be minimized at the same compressor position.

Performing linear fits for all three parameters, determining their  $d_0$  value and uncertainty, leads to the results displayed in the label of Fig.21(a), and can seen in the zoomed in view in Fig.21(b). All three  $d_0$  values lie within 1  $\mu$ m of each other, which is well below the value of the 25  $\mu$ m scan resolution. Due to these results, it can be confidently stated that the compressor effectively zeroes out the linear chirp and higher order spectral phase terms when optimized to deliver the shortest pulse duration on target.

# **5.2.6 Correlation of Linear Chirp to LPA Parameters**

The newly established linear chirp retrieval, which has been characterized and optimized in the previous Sec.5.2.5, can now be employed with confidence to the analysis of experimental data. The goal is to quantify if the observed correlation between laser pulse duration  $\tau_m$  and electron bunch charge (see Fig.15(a)) can be traced back to variations of the pulse spectral phase. If confirmed, the next step would be to locate the origin of the instability and attempt to stabilize it.

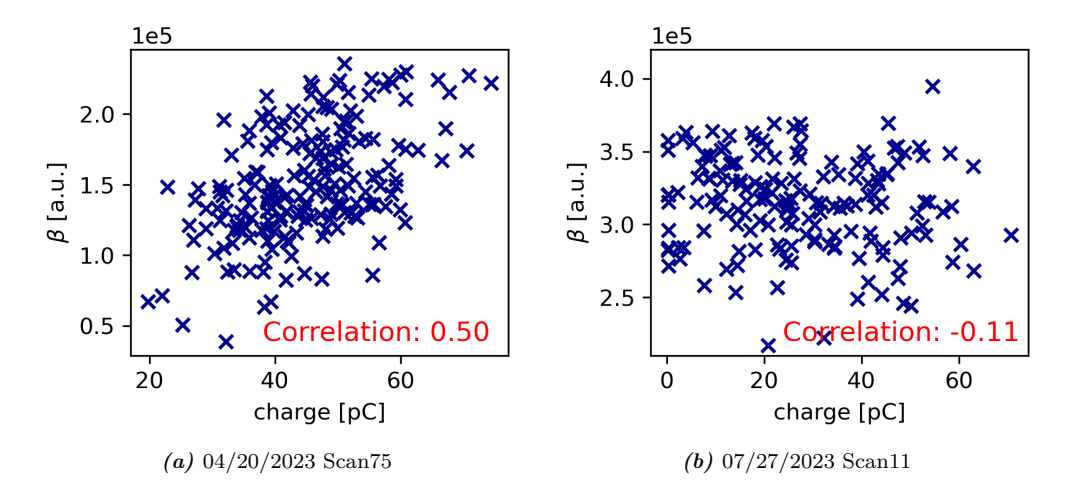


Figure 22: Correlation of linear chirp parameter  $\beta$ , retrieved from the spectral phase recorded by the *GRENOUILLE*, and the charge measured by the ICT before the VISA undulator. In both cases, the pulse on target  $\tau_0$  is compressed, and only the amount of dispersion witnessed by the measured pulse  $\tau_m$  is varied.

As can be seen in Fig.22, the results for the linear chirp parameter  $\beta$  match what was observed for the pulse duration. In the stretched case, or  $\tau_m \neq \tau_0$ , the linear chirp shows a noticeable correlation to the electron bunch charge (Fig.22(a)). In the compressed case, when the dispersion on the diagnostic line is compensated ( $\tau_m = \tau_0$ ), no significant correlation can be

observed. This indicates that the chirp retrieval accurately reproduces the observed shot-toshot dynamics of the laser-plasma interaction, which is crucial if it is to be employed as part of the new on-shot diagnostic. It also confirms that the linear chirp must be responsible for at least a significant part of the observed pulse duration changes, as already suspected based on the simulations displayed in Fig.16.

However, some of the effects which can be observed in the above shown plots are not as intuitive.

Firstly, as observed and discussed in Fig.15(a), one would not expect a simple linear correlation between linear chirp  $\beta$  and bunch charge in this case. Because the pulse on target is shortest for a certain value of  $\beta_m$  on the *GRENOUILLE* line that is  $\beta_m \neq 0$ , the highest measured charge would be expected at  $\beta = \beta_m$ , with decreasing charge for  $\beta > \beta_m$  and  $\beta < \beta_m$ . This explains why the highest charge was not observed for  $\beta_m \to 0$ , which would correspond to the shortest pulse on the diagnostic line, but instead for a severely stretched pulse on target.

Secondly, when comparing the plots in Fig.22, one can observe the  $\beta$  values in (b) to be exceeding the values displayed in (a). Seeing how Fig.22(b) was taken in the "matched" setting of the diagnostic, where  $\tau_m = \tau_0$  and therefor  $\beta_m = \beta_0$  is valid, the linear chirp would be expected to be much closer to zero. This counterintuitive behavior can be explained by a drawback of using the 4<sup>th</sup> order polynomial for the chirp retrieval instead of the simple 2<sup>nd</sup> order quadratic fit. The effect can be visualized by taking a closer look at the dataset displayed below.

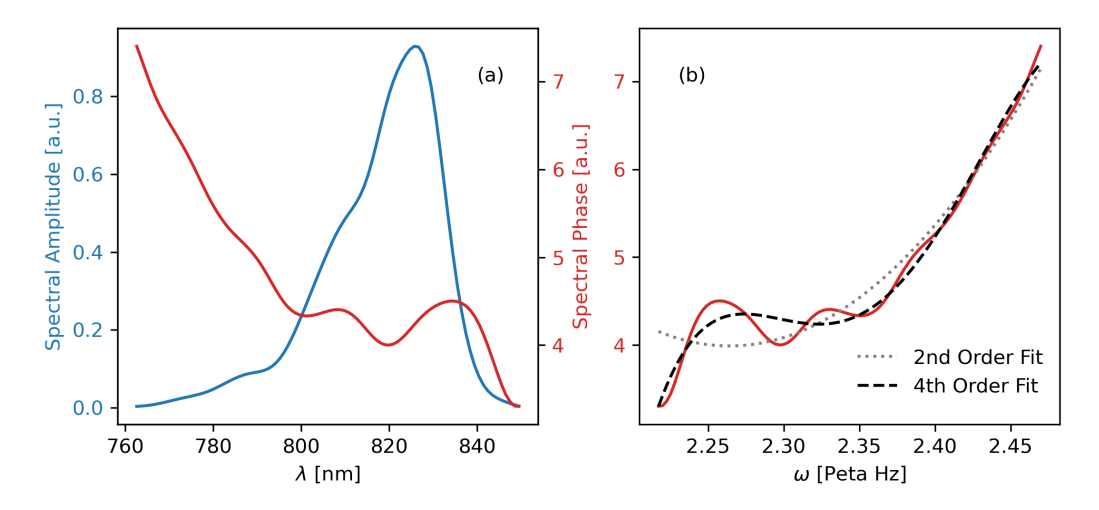


Figure 23: (a): Averaged spectral amplitude and phase of 200 consecutive laser pulses, retrieved from the raw images taken by the non-invasive GRENOUILLE setup. The shown wavelength interval is defined by  $840\,\mathrm{nm} > \lambda > 760\,\mathrm{nm}$  and the spectral amplitude threshold (SAT) > 0.003. (b): Averaged spectral phase over the frequency range corresponding to the wavelength interval in (a).  $2^{\mathrm{nd}}$  and  $4^{\mathrm{th}}$  order polynomials, as shown in Eq.5.7, have been fitted to the spectral phase curve for chirp parameter retrieval.

As can be seen in Fig.23(b), both fits seem to represent the average spectral phase trace reasonably well. But, when calculating the mean linear chirp parameter  $\bar{\beta}$  in both cases, the difference is tremendous.  $\bar{\beta}_{2^{\rm nd}} = 5.5 \cdot 10^2$ , but  $\bar{\beta}_{4^{\rm th}} = 3.14 \cdot 10^5$ . Due to its higher order terms, the 4<sup>th</sup> order polynomial fit can represent spectral phase trends with non-quadratic components and at non-ideal compression very well, and should represent the dynamics of  $\beta$  accurately, as shown in Fig.18. But close to compression, the high order terms can cancel each other out efficiently

enough to recreate a fairly flat spectral phase curve with still extremely large parameters. This is immediately visible in Fig.21(b), at the grating position closest to ideal compression of the laser pulse,  $\bar{\beta}$  and  $\bar{\gamma}$  are still on the order of 10<sup>4</sup>.

Based on the above discussed findings, it seems the absolute retrieved linear chirp values are not reliable for quantitative comparisons between scans conducted at different compression settings on the diagnostic line (especially with comparably small GDD offsets). However, this technique can still be utilized to visualize shot-to-shot fluctuations and give helpful qualitative insights into correlations of the laser-plasma interaction.

# 5.2.7 Investigation of spectral effects

The observed clear dependence between spectral phase (chirp) and pulse duration variations, and close to perfect reproduction of the temporal pulse behavior through simulation of spectral phase instabilities, strongly suggests the spectral amplitude does not contribute significantly to the detected long-term instabilities of the pulse duration. However, measuring the laser pulse spectrum non-invasively would add another important parameter of the laser pulse to the diagnostic capabilities of the HTU system. Technically, the *GRENOUILLE* can measure the temporal and spectral amplitude simultaneously, but the quality of the retrieved spectra through comparison with independent spectral measurements had to be verified.

The first comparative measurements of the laser spectrum were conducted by installing a fiber-coupled VIS-NIR spectrometer from *Hamamatsu* on the ghost beam diagnostics line (described in Sec.4.1), measuring leakage of the high power laser pulse. Due to the spectral phase diagnostic being non-invasive by design, spectral data with the *GRENOUILLE* and *Hamamatsu* could be taken simultaneously. The results from the first scan can be seen in Fig.24.

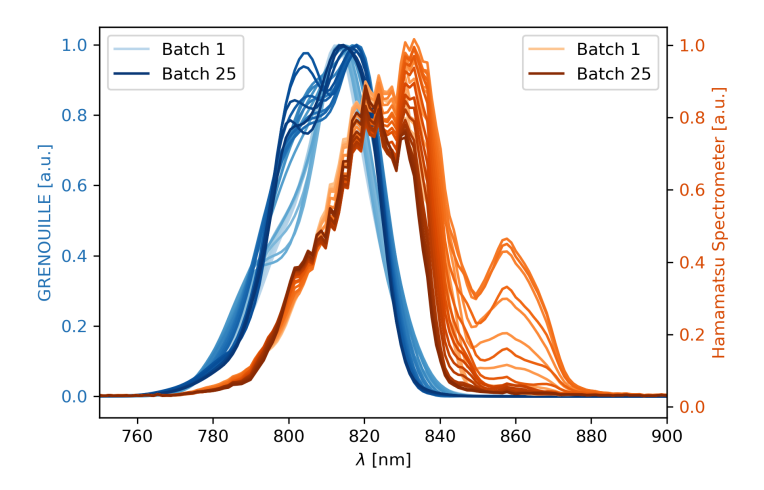


Figure 24: Spectral amplitude retrieved from the images taken by the GRENOUILLE (blue) and the Hamamatsu spectrometer (red). The data was taken during a compressor grating separation scan, 20 consecutive laser pulses at 1 Hz repetition rate were averaged per batch, corresponding to a step of the compressor position d. Each trace corresponds to a value of d in the measured interval of  $[40850,41450]\mu m$  (step size  $\Delta d = 25 \mu m$ ), the color of the traces get darker from smaller to larger values of d.

The immediate observations, when comparing the spectra from the GRENOUILLE and Hama-

matsu spectrometer, are the shifted center wavelength and spectral width changing with the compressor grating separation d. As can be seen when looking at the blue traces in Fig.24, the spectra as recorded by the GRENOUILLE are centered at about 810 nm and the overall spectral shape shows some changes with d (going from batch 1 to 25).

In comparison, the spectra recorded on the ghost beam diagnostic line by the Hamamatsu spectrometer (red), appear to be centered closer to 825 nm and exhibit a much stronger change in spectral shape with d (apparent by the second peak appearing at 860 nm for compressor grating separation values roughly in the center of the measured interval. Ideally, one would not expect to see any changes of the spectrum when simply varying the separation of the compressor gratings. To further investigate the shift and different dynamics of the two datasets, the second moment

$$D2\sigma = \sqrt{\frac{\sum_{i} ((\lambda_{i} - \lambda_{com})^{2} \cdot I(\lambda_{i}))}{\sum_{i} I(\lambda_{i})}}$$
 (5.11)

with the centroid

$$\lambda_{com} = \frac{\sum_{i} (\lambda_{i} \cdot I(\lambda_{i}))}{\sum_{i} I(\lambda_{i})}$$
 (5.12)

of the spectral amplitude was calculated for both cases, as can be seen in Fig.25.

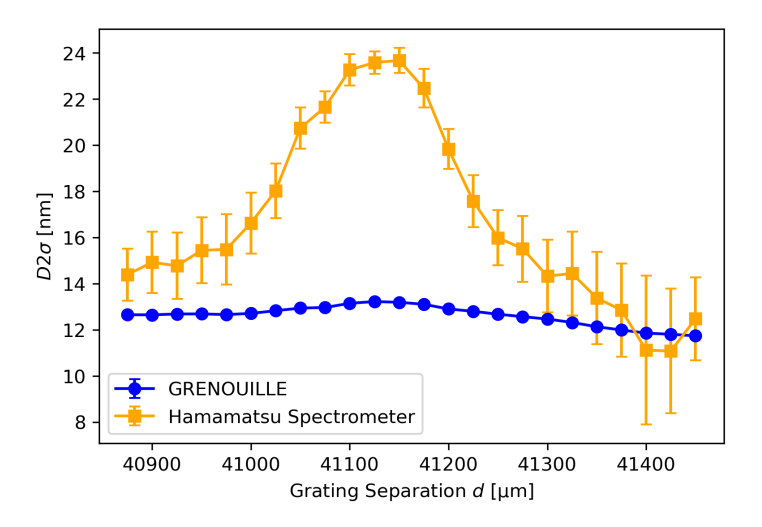


Figure 25: Second moment  $D2\sigma$  and corresponding standard deviation of the spectral amplitude for the dataset displayed in Fig.24. The values are averaged over 20 consecutive shots at each compressor position d.

When comparing the change of second moment values with changing grating separation d, a clear difference between the GRENOUILLE and Hamamatsu data can be observed. The spectral width of the laser pulse, as measured by the independent spectrometer on the ghost beam diagnostic line, shows a very strong dependence on d, as can be seen in Fig.25. It seems that this effect can be explained with the change in B-Integral between the two diagnostics. The B-Integral

$$B \stackrel{!}{=} \Phi_s(t) = -\frac{2\pi}{\lambda} \int_0^d n_2 I(z,t) dz$$
 (5.13)

is a measure for the phase shift  $\Phi_s(t)$  added to a laser pulse of wavelength  $\lambda$  and intensity evolution I(t), when transmitted through a medium with non-linear refractive index  $n_2$  of

thickness d along the laser axis z [91, 92].

Assuming the intensity to be constant throughout the medium, and choosing t = 0 for  $I(t = 0) = I_0$  the peak intensity, Eq.5.13 can be simplified to

$$B_0 = \frac{2\pi}{\lambda} n_2 I_0 d \tag{5.14}$$

In this simplified case, using the non-linear refractive index for fused silica determined by Ensley and Bambha [93] and the beam parameters from Sec.4.1, the B-Integral value for the beam analyzed on the *GRENOUILLE* diagnostic line is approximately:

$$B_{0,F} = \frac{2\pi}{\lambda} n_2 \frac{P_L}{\pi w^2} d$$

$$= \frac{2\pi}{800 \text{ nm}} \left( 2.7 \cdot 10^{-20} \frac{\text{m}^2}{\text{W}} \right) \frac{(< 0.005) \cdot 6.5 \cdot 10^{13} \text{ W}}{\pi (5 \text{ cm})^2} 25.4 \text{ mm}$$

$$< 0.22$$

Here,  $P_L$  is the laser power incident on the vacuum window and determined by the R > 99.5% reflectivity of the HR optic the beam is leaked through:  $P_L = P_0 \cdot T = P_0 \cdot (1-R) = P_0 \cdot (<0.5\%)$ . The resulting value of the B-Integral is low enough for an ultra-short laser pulse system that one would not expect to see non-linear effects like spectral broadening to significantly impact the measured pulse, which matches the observations in Fig.25.

For the *GRENOUILLE* line, the HR leakage of a roughly 10 cm diameter beam is sent through the vacuum window. However, the ghost line utilizes a copy of the high-power main beam generated by the reflection at the rear surface of the final steering mirror, which has a 98% surface reflectivity on the front, and 80% reflectivity on the back surface. Therefore, a total  $2\% \times 80\% \times 2\% = 0.032\%$  of the main beam are focused by the OAP, and sent out through the vacuum window with a transverse beam size on the order of just 1 cm. Assuming both vacuum windows are fused silica and of identical thickness, as well as no losses in the beam path between the two pick-off locations, Eq.5.14 can be utilized to estimate the difference in B-Integral in the two cases:

$$B_{0,G}/B_{0,F} = \frac{\frac{2\pi}{\lambda}n_{2,G} \quad I_{0,G} \quad d_{G}}{\frac{2\pi}{\lambda}n_{2,F} \quad I_{0,F} \quad d_{F}}$$

$$= \frac{I_{0,G}}{I_{0,F}}$$

$$= \frac{P_{0,G}}{\pi w_{G}^{2}} \cdot \frac{\pi w_{F}^{2}}{P_{0,F}} = \frac{P_{0,G}}{P_{0,F}} \cdot \frac{w_{F}^{2}}{w_{G}^{2}}$$

$$\approx \frac{0.032\%P_{0}}{< 0.5\%P_{0}} \cdot \frac{(5 \text{ cm})^{2}}{(0.5 \text{ cm})^{2}} > 6.4$$

With the value for  $B_{0,F}$  calculated above, that puts the B-Integral for the ghost beam on the order of  $B_{0,F} = 1.41$ . This value supports the hypothesis of non-linear effects on the ghost line causing the strong spectral broadening behavior observed close to compression when scanning the compressor separation (see Fig.25), given the fact that B > 1 is considered the threshold were non-linear effects usually become relevant [92]. The systematic red-shift of the entire spectrum observed in Fig.24 might be caused by Raman scattering [94], which would also explain the modulation of the spectral amplitude.

The calculations and plots above make it clear that the *Hamamatsu* spectrometer on the ghost line can not be used as a reliable diagnostic to benchmark the quality of the spectral retrieval of the *GRENOUILLE*. A *Thorlabs CCS175* spectrometer was installed directly on the *GRENOUILLE* diagnostic line, eliminating issues based on different copies of the beam being analyzed. The new setup, modified with respect to Fig.12, can be seen in Fig.26.

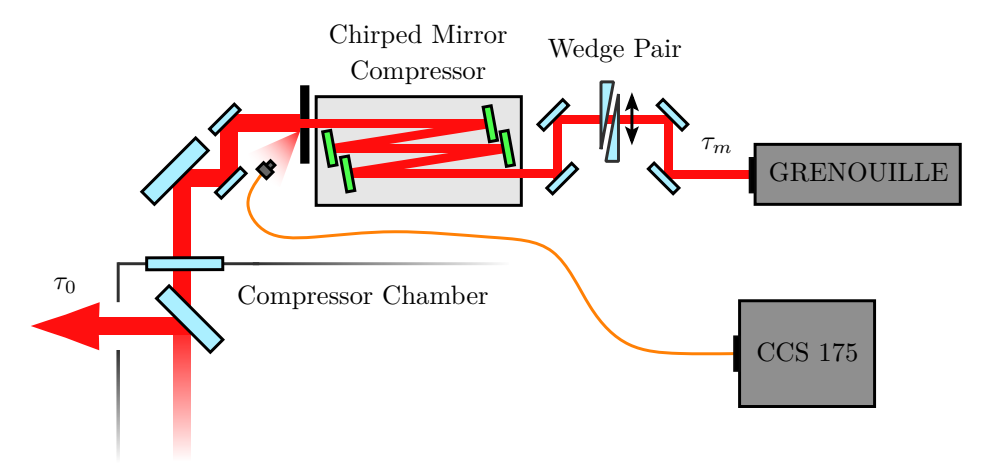


Figure 26: Schematic display of the non-invasive, on-shot spectral phase diagnostic line. To measure the spectrum of the laser pulse independently from the GRENOUILLE device, a CCS175 spectrometer from Thorlabs was installed, picking off the scattered reflection of the laser pulse from the front surface of the iris, which is used to downsize the beam before sending it to the chirped mirror compressor. A single-mode fiber transports and couples the beam into the spectrometer.

Designated compressor grating separation scans were conducted at low power to reproduce the experimental conditions of Fig.24.

As can be seen in Fig.27, the *GRENOUILLE* spectra match the corresponding data from the previous spectral analysis, displayed in Fig.24, very well. Not just the overall wavelength range (780 - 840 nm), but also the observed dynamics when changing the compressor grating separation d.

Comparing the Thorlabs and Hamamatsu spectral data, it becomes clear that the strong non-linear effects impacting the behavior of the spectrum when scanning d have successfully been mitigated. For the Thorlabs data, there is barely any change observable between the spectral amplitude traces for the different batches. This confirms the hope that installing the spectrometer on the diagnostic line would lead to more conclusive, reliable spectral data independent of the GRENOUILLE. It seems that the B-Integral, as the calculations above suggested, was indeed responsible for the observed spectral broadening and red-shift of the spectrum.

However, even if less pronounced than in the *Hamamatsu* setup, the data from the CCS175 spectrometer still shows a significant mismatch in spectral width and center wavelength with respect to the retrieved *GRENOUILLE* spectra.

The most likely explanation seems to be that there is a systematic problem with the accuracy of the *GRENOUILLE* retrieval algorithm, which calculates the spectral amplitude and phase traces based on the SHG FROG images. To investigate this possibility, the raw and retrieved images will be compared.

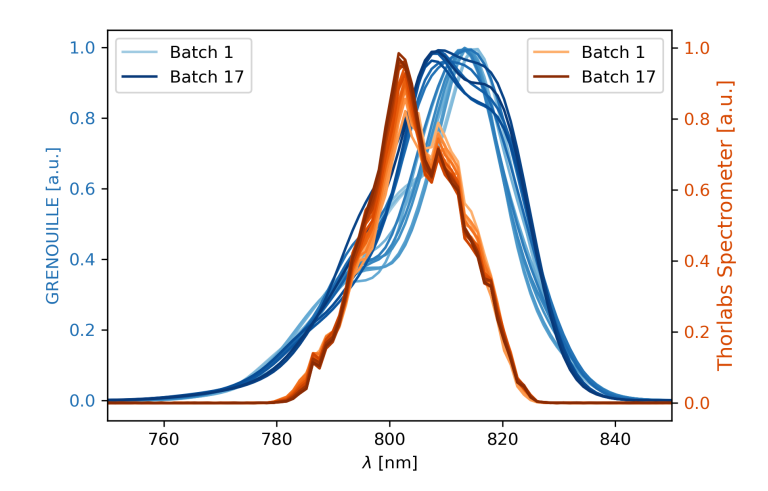


Figure 27: Spectral amplitude retrieved from the images taken by the GRENOUILLE (blue) and the Thorlabs CCS175 spectrometer (red). The data was taken during a compressor grating separation scan, 10 consecutive laser pulses at 1 Hz repetition rate were averaged per batch, corresponding to a step of the compressor position d. Each trace corresponds to a value of d in the measured interval of  $[40800,41200]\mu m$  (step size  $\Delta d = 25 \,\mu m$ ), the color of the traces gets darker from smaller to larger values of d.

Because the design of the SHG FROG device is based on an autocorrelator and transient grating spectrometer, simply integrating the spectral axis of the raw images delivers the spectral amplitude trace [37, 40].

Fig.28(a) shows the result of applying this method to the image averaged over the number of shots per compressor grating separation step  $\Delta d$ .

Comparing the traces from the averaged raw and retrieved images for the first compressor step, shown in Fig.28(b), proves that the retrieval process adds a significant amount of uncertainty to the analyzed spectral data.

Because of previously conducted studies focused on the impact of the retrieval time on the FROG error, too short of a retrieval time can be excluded as the potential issue. This dataset, as well as all the others analyzed in this work, have been retrieved using a 30 s retrieval time per image.

If not the retrieval time, then the retrieval algorithm itself must be responsible. However, given the fact that the retrieved pulse duration, as well as the spectral phase (which is extracted from the retrieved spectral amplitude and phase traces) show a clear correlation to real LPA parameters (see Fig.15(a) and Fig.22(a)), it seems the uncertainty from the retrieval must be a systematic effect that does not overshadow shot-to-shot dynamics. If it can be shown that the second moment  $D2\sigma$  from the raw images correlates with the retrieved parameters, it will provide us with a more reliable, yet much less time consuming technique to quantify variations of the spectral and temporal dynamics of the laser pulse on the *GRENOUILLE* diagnostic line.

By design, the raw and retrieved traces (from which both second moments as well as pulse duration and spectral width are calculated) should be highly correlated [37]. As shown above, the retrieval process does not recreate the raw data perfectly. To investigate if raw and retrieved traces still correlate, the *GRENOUILLE* data from the compressor scan displayed in Fig.27 is analyzed. The pulse duration  $\tau_{retrieved}$  and spectral width  $\Delta \lambda_{retrieved}$  are extracted from

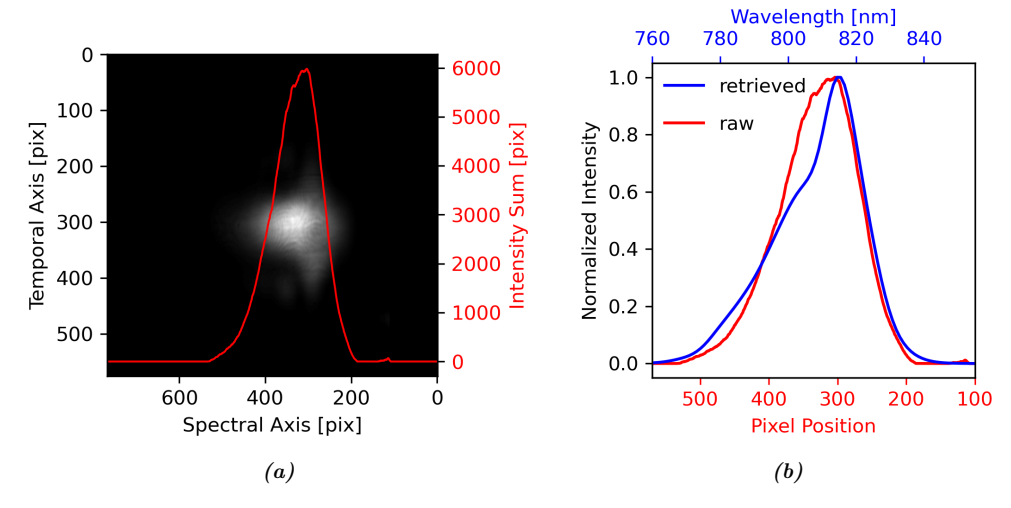


Figure 28: Calculation of the spectral amplitude trace from the raw SHG FROG images taken by the GRENOUILLE, and comparing it to the retrieved spectrum. Both traces represent the first grating separation position  $d=40\,800\,\mu\text{m}$ . (a): Average over ten consecutive raw SHG FROG images, taken with the GRENOUILLE. Integrating over the spectral axis delivers the red trace, which corresponds to the spectral amplitude. (b): Comparison between the normalized spectral amplitude traces extracted from the averaged raw (red) and the retrieved (blue) GRENOUILLE images. Because the exact pixel-to-wavelength calibration is unknown, the range of the x-axis for the trace from the raw image was adjusted to match the two curves.

the retrieved images (generated after running 30 s post-analysis on every raw image). The second moments  $D2\sigma_{temp}$  and  $D2\sigma_{spectr}$  are determined directly from the raw images taken by the *GRENOUILLE*, after simply integrating the image over the temporal or spectral axis, respectively. The result of correlating the raw temporal second moment against the retrieved pulse duration can be seen in Fig.28(a), as well as the raw spectral second moment against the retrieved spectral width in Fig.28(b).

When comparing the temporal parameters in Fig.29(a), a clear correlation between the data extracted from the raw and retrieved images of  $\rho = 0.82$  can be found. This is to be expected if there is no major issue with the retrieval accuracy, because the integrated temporal axis and pulse duration are inherently correlated based on the design of the SHG FROG autocorrelator [37]. To quantify how much the retrieved and raw traces fluctuate shot-to-shot, the relative uncertainty

$$\delta x = \frac{\Delta x}{\bar{x}} \tag{5.15}$$

is calculated for both parameters analyzed in Fig.29(a), with  $\Delta x$  the standard deviation and  $\bar{x}$  mean value of the dataset. Applying Eq.5.15 to both cases delivers  $\delta(\tau_{retrieved}) = 0.28$  and  $\delta(D2\sigma_{temp}) = 0.16$ . These results show that the retrieved temporal pulse parameter has an almost twice as high relative uncertainty, compared to the raw temporal pulse parameter. It seems that the retrieval process adds a non-negligible amount of jitter, which is not inherent to the raw data. This might impact the analysis accuracy of shot-to-shot stability of the laser pulse. Going forward, using the raw image second moment  $D2\sigma_{temp}$  seems to be the more stable and reliable choice.

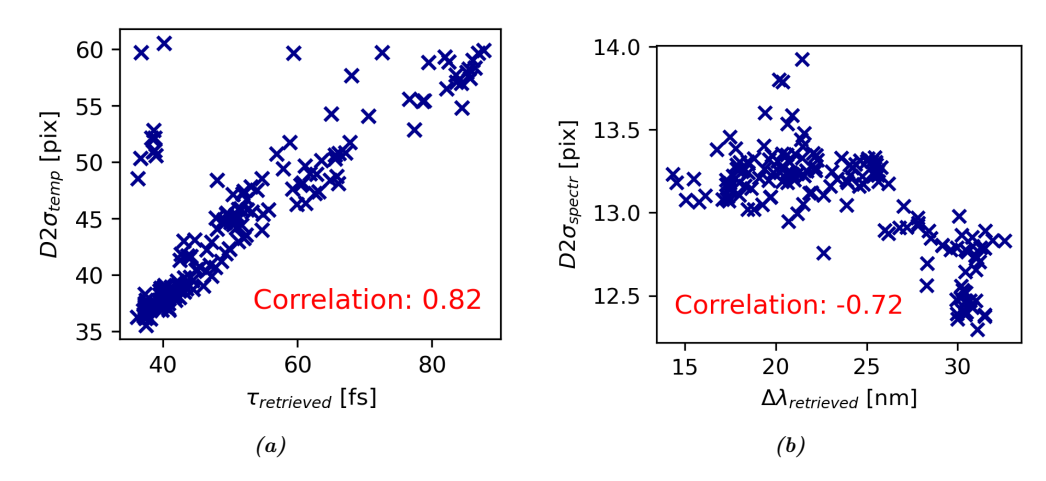


Figure 29: Investigating the correlation between second moments  $D2\sigma$  extracted from the raw GRENOUILLE images, and the pulse parameters retrieved from post-analyzed data. (a): Second moment of the raw GRENOUILLE image temporal axis  $D2\sigma_{temp}$  vs. retrieved pulse duration  $\tau_{retrieved}$ . (b): Second moment of the raw GRENOUILLE image spectral axis  $D2\sigma_{spectr}$  vs. retrieved spectral width  $\Delta\lambda_{retrieved}$ .

Focusing on the spectral properties, Fig.29(b) shows the correlation between the second moment  $D2\sigma_{spectr}$  of the raw images, integrated over the spectral axis, and the spectral width calculated from the retrieved images. One can observe a fairly strong correlation of  $\rho = -0.72$  which, as discussed above, is to be expected. If there are real changes in the spectral width of the laser pulse, they should be represented in the raw and retrieved images. However, the amplitude of their respective spectral variations differs hugely. Applying the relative uncertainty technique, as discussed above and displayed in Eq.5.15, one finds  $\delta(\Delta \lambda_{retrieved}) = 0.21$  and  $\delta(D2\sigma_{spectr}) = 0.02$ .

This result has two clear implications:

- 1. The real change in spectral width during the compressor scan analyzed here, as recorded by the raw *GRENOUILLE* images, is just 2%. This confirms the expectations that the spectral width of the laser pulse should not change when simply varying the compressor grating separation d. Furthermore, it supports the previous hypothesis, based on the B-Integral calculations, that there are no strong non-linear effects on the *GRENOUILLE* diagnostic line, creating changes of the spectral width through spectral broadening.
- 2. The retrieval process adds a high amount of uncertainty to the spectral axis of the FROG image. An increased relative error by about a factor of two for the temporal case had already been observed, but in the spectral case the difference exceeds a factor of ten.

Combining the observations from Fig.29(a) and (b) makes it clear that going forward the second moment from the raw images should be used as the proxy for temporal and spectral behavior of the laser pulse.

Not only does using the second moments allow real-time analysis of the raw FROG images, eliminating the need to apply time-consuming retrieval algorithms as post analysis, it also delivers results highly correlated to the pulse duration and spectral width, but with significantly reduced relative uncertainty.

The importance of this new technique for reliable, fast analysis of LPA data going forward can not be overstated.

# 5.3 Undulator Radiation Diagnostics

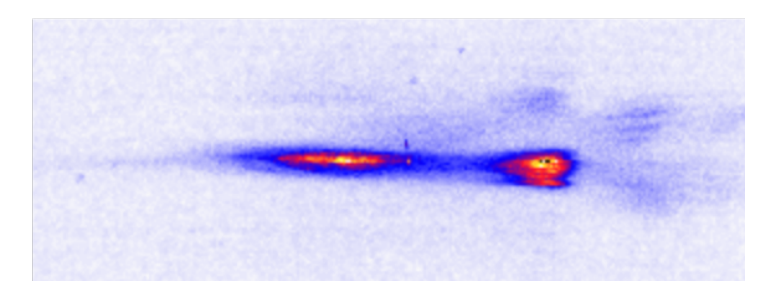


Figure 30: Image of the first shot of undulator light suggesting coherent emission on the HTU beamline, captured on the optical spectrometer.

After the first undulator light was observed in 04/2023 (see Sec.7.1 for a more detailed discussion), the shape of the recorded spectrum, as can be seen above in Fig.30, immediately drew the accuracy of the spectrometer setup into question.

In addition, the need arose for a way to confirm that the observed radiation was indeed originating from the SASE FEL process.

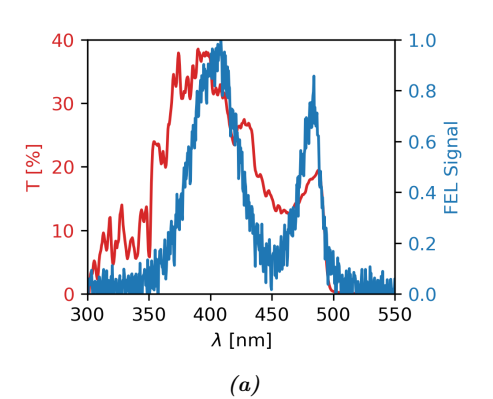
This section will describe the work that went into upgrading and adding diagnostic capabilities of the undulator setup, to address the above mentioned concerns.

# **5.3.1** UV Spectrometer

The simple optical spectrometer installed on the 4 m translation stage parallel to the undulator (see Fig.7) was based on a 45° prism mirror and 200  $\mu$ m thick YAG:Ce screen mounted on a pneumatic plunger, sending the electron beam profile and undulator radiation out of the vacuum system (at any of the nine ports along the undulator). A dichroic mirror separates the YAG:Ce emission and undulator radiation, transmitting the latter onto a two inch diameter, fused silica lens. The lens focuses the collected light through a transmission grating onto the chip of a acA2000-165um camera from Basler, which has a < 500 nm filter mounted to it for further reduction of room and laser light. The calibration was conducted using a 450 nm diode laser, by sending it to the spectrometer a simple pixel-to-nanometer calibration was established.

When the first undulator light on the HTU beamline was observed, the spectra showed an obvious dip feature, as can be seen in Fig.30. To try and understand the origin of the spectral shape, a white light source and *Black Comet* spectrometer from *STELLARNET* were used to set up a calibration diagnostic, measuring the transmission curves of all optical elements in the beam path of the undulator light. This included the VISA plunger setup, vacuum window, dichroic mirror, lens, transmission grating and camera filter. The result can be seen in Fig.31b (red), overlayed with an averaged undulator radiation spectrum (blue), taken on 04/20/2023. The quantum efficiency of the camera chip was retrieved from Ref.[95] and displayed in Fig.31(b).

Because the undulator radiation was expected to be centered at  $\lambda_0 \approx 420 \,\mathrm{nm}$  when using electrons of 100 MeV central energy (see Sec.3.2.1 and Eq.3.2), the region of the spectrum around this center wavelength is of highest concern. As Fig.31(a) shows clearly, the transmission T in the interval from 350 to 500 nm is strongly modulated, and outside of it effectively zero. Of



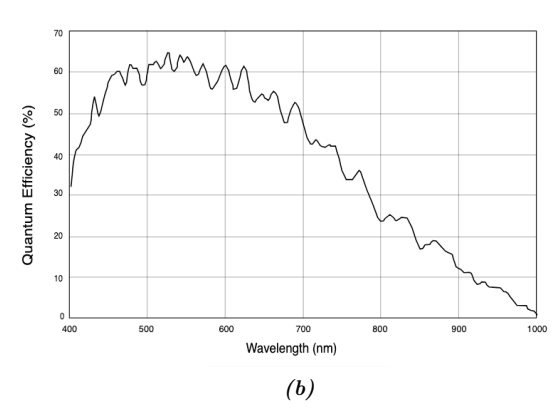


Figure 31: (a): Transmission curve of the optical spectrometer (red) and a normalized, integrated spectrum extracted from Fig.30. (b): Quantum efficiency curve of the camera used in the spectrometer setup [95].

course, multiplying the spectrum with the inverse transmission generally is an option to correct for such inhomogeneities, but not in areas where there is effectively no signal transmission. Even where  $T \neq 0$ , the transmission of the already weak signal is so low that the signal-to-noise ratio is much lower than required for signals as weak as being detected in this case.

In addition, the quantum efficiency of the CMOS chip used in the spectrometer camera is only about 45% at 420 nm (see Fig.31(b)), and varies drastically when moving to slightly shorter or longer wavelengths. *Basler* did not report a value for the quantum efficiency below  $\lambda < 400$  nm.

Having the ability to precisely assess small differences in undulator signal intensity is key when optimizing matching, transport and transmission of the electron beam through the undulator. For this reason, the choice was made to upgrade all the components possible to UV enhanced alternatives. This includes the focusing lens, transmission grating and the camera itself.

Implementing these changes caused a significant improvement in transmission of the spectrometer setup above 300 nm, as can be seen in Fig.32(a). In the wavelength range of interest (350 - 500 nm), signal is now being detected with an effectively flat transmission of  $\sim 60\%$ . The resulting spectra do not exhibit the previously observed dip feature at 450 nm and match the expected distribution, centered around  $\lambda_0 \approx 400$  nm, much more closely. Fig.32(b) shows the raw acquired spectrometer image integrated to gain the FEL Signal trace in (a). The parabolic shape of the first diffraction order of the undulator radiation wavelength  $\lambda_l$ , observed in the recorded spectra, qualitatively matches the theoretical expectation of angular dependence of the coherence (see Eq.3.3), discussed in Sec.3.2.1.

Because, for most of the analysis of undulator performance, the main metric used will be the total signal strength of observed undulator radiation, an energy calibration of the system is required.

For this purpose, a 405 nm blue diode laser was used, initially installed on the system to set references on the YAG:Ce screen profile monitors for electron beam trajectory alignment. It is set up to be sent down the magnetic axis of the VISA undulator and offers precise control over the diode output power. Inserting a plunger and directing the light onto the optical spectrometer, the counts in a region of interest defined around the 1<sup>st</sup> diffraction order measured at a certain exposure time, can then be used to calculate a counts-to-energy calibration for the

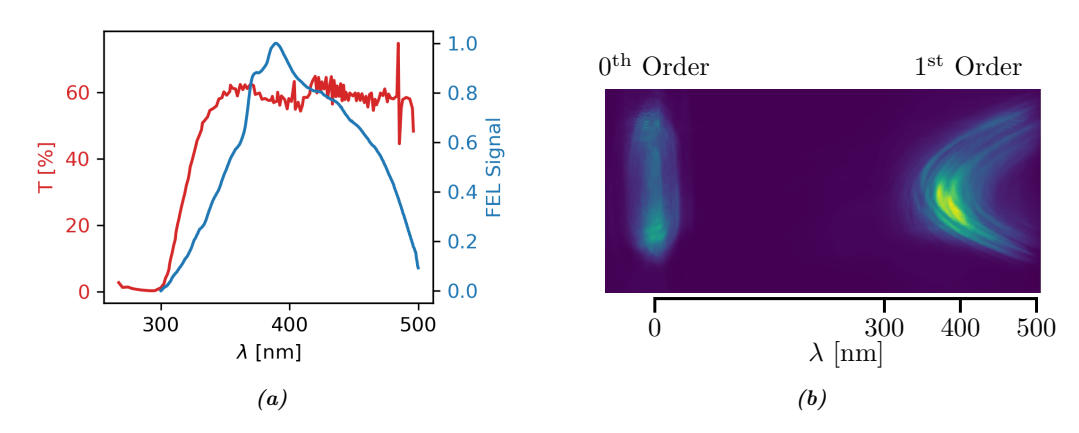


Figure 32: (a): Transmission curve of the UV enhanced optical spectrometer (red) and normalized integrated undulator emission spectrum. (b): Actual acquired image of the 0<sup>th</sup> and 1<sup>st</sup> diffraction orders of the undulator radiation, with wavelength calibration for reference.

setup. Conveniently, because the system has a reasonably flat transmission curve, this energy calibration can be assumed to be independent of wavelength (in the region of interest). Setting the diode laser to an output power of  $1\,\mathrm{mW}$  and camera exposure to  $150\,\mathrm{ms}$ , as well as taking into account the transmission at  $405\,\mathrm{nm}$  of the neutral density (ND) filter used to reduce the diode laser intensity, the energy calibration factor was determined to be

$$F_E = 1.4637 \times 10^{-6} \ [\frac{\text{nJ}}{\text{counts}}]$$

This factor is used going forward to determine the energy of undulator radiation measured along the undulator by integrating the part of the spectrometer image that includes the 1<sup>st</sup> order of diffraction.

### **5.3.2** Emittance Spoiler

After the detection of what appeared to be the first undulator signal recorded on the HTU experiment, it seemed necessary to devise a way of confirming that the observed light is indeed generated through the SASE FEL process. As a first test, the current on the magnetic spectrometer upstream of the VISA undulator was turned on. This ensured that no electrons would reach the undulator on a matched trajectory, and the signal disappeared as expected. However, a more sophisticated while still repeatable and flexible technique to be added to the system was desired. To satisfy these criteria, a 10 µm thick nitrocellulose pellicle (P1 in Fig.7) was installed on a pneumatic plunger before the undulator entrance, close to where the electron beam comes to a focus. By scattering the transmitted electron beam it serves as an emittance spoiler, simple estimations for a 100 MeV beam suggest that the normalized emittance would increase by more than 10 mm-mrad when the spoiler is inserted [96] (the exact value depends on the beam parameters at the location of the inserted pellicle). Such large emittance values eliminate the possibility of generating FEL gain, but the pellicle is thin enough not to have significant impact on the electron beams energy or trajectory. Both previous statements were verified experimentally, by taking alternating data sets with the spoiler inserted and retracted, as can be seen in Fig.33.

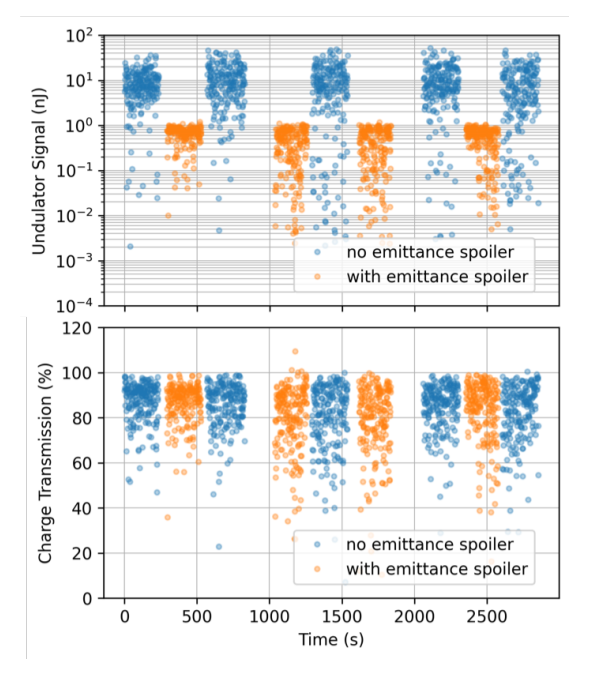


Figure 33: Undulator signal (top) and charge transmission (bottom) measured over roughly one hour of LPA-driven FEL operation. Blue data points represent the emittance spoiler was retracted, orange that it was inserted.

The results, taken during the campaign for the work discussed by Barber et al. [72], demonstrate the close match between observation and theoretical expectation for the emittance spoiler. With the pellicle inserted, no FEL gain above the level of incoherent emission can be observed, while the charge transmission is not affected. These tests were repeated multiple times over the course of about one hour of continuous operation, showing the effectiveness of the new diagnostic. If the observed optical signal can be influenced as such, simply by spoiling the beam emittance, the signal with the spoiler removed has to be originating from SASE FEL lasing. Thus, this new diagnostic tool can serve as a way to quickly distinguish between incoherent undulator light and coherent FEL radiation, simply by inserting and retracting the pellicle.

# 6 Efforts to stabilize the LPA Interaction

Laser-plasma accelerators (LPAs) are emerging as a potentially more compact and cost efficient alternative to classic radio-frequency (RF) accelerators, inspiring hope to make the crucial technology of high energy and brightness electron beams accessible to a much wider range of research and industrial facilities [5, 18].

However, they come with their own set of unique challenges, namely the reliable and reproducible generation of stable electron beams. Because of the inherent property of the LPA process that a new plasma column, which acts as the accelerating cavity, is formed on every shot, the stability of the LPA interaction strongly affects the electron beam parameters. In contrast to RF accelerators, this can lead to significant shot-to-shot fluctuations. Especially potential instabilities of the drive laser properties, namely pulse energy, duration, as well as longitudinal and transverse beam pointing, can be expected to be the most significant cause of electron beam fluctuations. [10, 97]

For this reason, a part of the work conducted for this thesis project was dedicated directly towards improving the stabilization of key drive laser parameters. First, the implementation of a beam stabilization system on the amplifier table will be discussed in Sec.6.1, as an effort to reduce pulse energy fluctuations and drift. Utilizing the non-invasive, on-shot pulse duration diagnostic (described in Sec.5.2) to track down and try to stabilize pulse duration jitter will be described in Sec.6.2. Finally, a project to control the change in laser pulse wavefront will be introduced in Sec.6.4, which has been able to effectively mitigate longitudinal focal instabilities in the LPA interaction region, leading to huge performance improvements of the LPA-driven FEL studies.

Some of the results discussed in Sec.6.1-6.3 were published as part of the long-term LPA-driven FEL stability campaign by Kohrell et al. in Ref.[98].

# 6.1 Laser Pulse Energy

#### 6.1.1 Motivation

The fully amplified laser beam of the HTU system normally shows a 1-2% energy jitter, and performance degradation over the course of 5 to 8 hrs of operation on the order of 5% peak energy loss have been recorded. With its theoretically expected correlation to the electron energy, and the goals for reliable, stable LPA-driven FEL operation, it is imperative to reduce the laser pulse energy jitter and long-term drift as much as possible.

Due to strongly noticeable transverse beam pointing instabilities on the amplifier table, the decision was made to implement a beam stabilization system between the first and second amplifier crystal (see Fig.5). It was expected that stabilizing the position of the laser pulse with respect to the pump profile on the crystal would reduce not only beam pointing jitter and drift further downstream, but also stabilize the laser pulse energy.

# 6.1.2 Stabilization System Setup

The existing beam stabilization systems installed on the HTU system are commercial units from *TEM Messtechnik*. They offer a uniquely high amount of control over the parameters of the proportional-integral-derivative (PID) controller, which is used for active control of the corrective action of the motorized mirror mounts, as well as beam position and angle set point.

However, this amount of control comes with a high degree of complexity in setup and maintenance of the system. Because the stabilization system on the amplifier table has the main purpose to guarantee stable laser pulse energy output, and its position and angle set point will not have to be dynamically adjusted after the initial setup, reliable operation was prioritized over the capability to control a wide range of parameters. For this reason, a commercial unit from MRC Systems was chosen. It consists of two 2-inch piezo-driven mirrors which support  $> 300\,\mathrm{Hz}$  correction bandwidth for active stabilization, and two position-sensitive device (PSD) detectors, offering  $< 0.5\,\mu\mathrm{m}$  spatial resolution. To enable a stabilization bandwidth exceeding the 1 Hz frequency of the main laser, the 1 kHz un-amplified background pulse train (discussed in Sec.5) will be utilized. The system offers control only over the beam position set point on both detectors, as well as the proportional (P) factor of the PID loop, which for a beam stabilization system is expected to be most significant (moving an actuator by x amount should change the beam position by a proportional factor  $K \cdot x$ ). It therefore provides a flexible and capable, yet easy-to-use tool for beam stabilization.

The simplest approach to stabilize the beam to a straight line reference through the amplifier was chosen, using the first mirror to stabilize the beam position on the surface of the second mirror, and using the second mirror to stabilize the beam at a position of the second amplifier crystal. To achieve non-invasive monitoring of the beam position in two different planes between Amp1 and Amp2, the system was set up with both PSDs detecting leakage through a different HR optic, as can be seen in Fig.34. PSD 1 was placed in the plane corresponding to the surface of the second mirror, and PSD 2 in the plane as close to the surface of the second amplifier crystal as possible, given the constraints imposed by the existing amplifier setup.

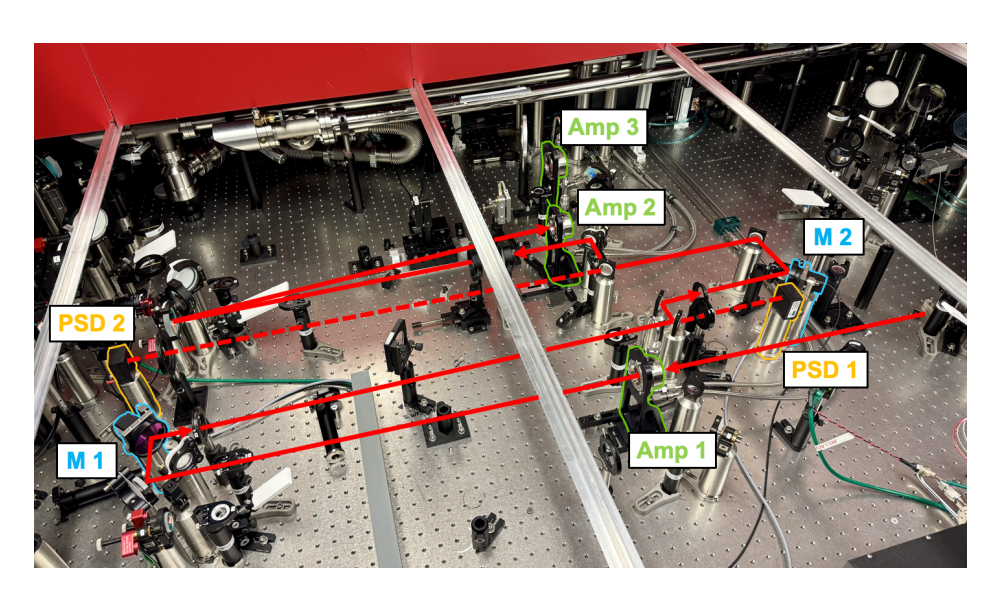


Figure 34: Picture of the HTU laser system main amplifier, displaying the position of the MRC mirrors (M1, M2) and PSD sensors (PSD1, PSD2) used for active stabilization between the first (Amp1) and second amplifier crystal (Amp2). The beam path has been drawn schematically to help visualize the setup.

In addition to working around the pre-existing optical setup, operating a beam stabilization system in the environment of a high-power, multi-pass amplifier came with its own unique set of challenges.

Firstly, stray light turned out to be a significant issue. The 16 J GAIA pump laser creates an enormous amount of highly intense background light at 532 nm, which all cameras and other optically sensitive diagnostics installed on the amplifier table have to be shielded against. Because of the large wavelength gap between the pump and emission wavelength of the Ti:Sapph crystals, this is issue is solvable by protecting the diagnostics with band-pass filters of high optical density.

Much more challenging was the mitigation of the 800 nm stray light. Due to the amount of optics and reflective surfaces in a small, confined space, all the leakage beams and back-reflections create a vast background of light at the signal wavelength. In addition to these coherent background sources, the spontaneous emission from the three pumped Ti:Sapph crystals adds powerful, omni-directional sources of 800 nm emission. Because the PSDs are supposed to pick up and precisely monitor the position of the un-amplified 2.5 mJ, 1 kHz background laser pulses after leaking through an HR optic, the stray light can be expected to be of high enough intensity to affect the position readout of the PSDs. During the system setup, this proved to make the detection highly unstable and prone to misinterpretation of the beam position, leading to the actuators steering the beam away from the reference axis, and even completely off the second amplifier crystal.

After many iterations with different types of shielding, the most effective strategy proved to be placing irises close to the PSD surfaces, effectively eliminating stray light on the PSDs while maintaining sensitivity to the small amplitude jitter of the transverse beam position.

Secondly, the significant energy difference between the  $2.5\,\mathrm{mJ}$  1 kHz background pulse train, which was to be used for stabilization, and the  $100\,\mathrm{mJ}$  1 Hz amplified pulses posed an inherent challenge. The MRC system had been installed between Amp1 and Amp2 to keep the difference in pulse energy between the 1 kHz and 1 Hz pulse trains as low as possible, but even the present factor of  $40\times$  proved to be too significant. For precise determination of the beam position on the PSD, it is essential to operate the detectors such that the 1 kHz signal is close to their saturation limit. In this case, the  $40\times$  more intense 1 Hz amplified pulse it at risk of damaging the sensor. Because both signals are at the same wavelength, there is no way of spectrally separating the two. Furthermore, the MRC system is very sensitive to interruptions of the beam, and will steer the beam drastically when it gets clipped in the attempt to maintain alignment. This prohibited the use of mechanical shutters, due to the high-power beam and highly sensitive alignment tolerances downstream of the amplifier.

The option found to be the most robust and reliable was modifying the input trigger to the MRC control unit. By setting it to its default "OFF" level for an interval of  $\pm 5\,\mathrm{ms}$  centered around each amplified pulse, the detector simply stops acquiring data when the high power signal arrives. This proved to successfully protect the sensitive electronics from damage by the amplified 1 Hz beam and prevent accidental misalignment of the beam due to clipping, when shuttered mechanically.

#### 6.1.3 Results

Analysis of beam position root-mean-square (rms) jitter  $\Delta r$  at different positions on the amplifier table revealed significant improvements when running the MRC active stabilization system, as can be seen in Tab.3. The values for the PSD sensors were extracted from the MRC software and represent the combined  $r = \sqrt{x^2 + y^2}$  beam position. The statistics at the amplifier crystals were determined by taking 500 shots on each of the cameras imaging the respective

planes. The RMS jitter of the beam position centroid for x and y was calculated in pixels, and the camera-specific pixel-to-µm calibrations used to extract the spatial values.

	$\Delta r \; [\mu \mathrm{m}]$					
	MRC Off		MRC On		Improvement	
	$\Delta x$	$\Delta y$	$\Delta x$	$\Delta y$	$\Delta x$	$\Delta y$
PSD 1	27.1		3.9		6.9	
PSD 2	12.1		2.4		5.0	
Amp 2	141.8	87.6	16.5	26.0	8.6	3.4
Amp 3 Input	220.5	135.8	29.4	82.3	7.5	1.7
Amp 3 Output	528.4	375.3	86.7	269.7	6.1	1.4

**Table 3:** Comparison of beam position rms jitter at different locations in the HTU main amplifier, with and without running the *MRC* beam stabilization system.

There are a number of observations which can be made from the data shown in Tab.3. The most noteworthy is that the MRC stabilization system is able to significantly reduce beam position rms jitter downstream of Amp 1 in the HTU main amplifier. The relative improvement decreases with distance to the stabilization setup, which is to be expected. More optics and sources of instability are introduced with increased optical path length, whose effect is not monitored by the PSD sensors, and therefore can not be corrected.

Additionally, there is a significant difference between the instability in x and y direction on all three positions that monitor them separately. When the stabilization is turned off, in all three cases the ratio between the two components is  $\Delta x/\Delta y = 1.5 \pm 0.1$ , so the inherent beam position jitter is about 1.5 times stronger in x than in the y direction. The most likely explanation for this effect is that the vast majority of optics in the system are mounted on vertical posts fixed to the horizontal optical table. Realistically, most vibrations affecting the optics will be horizontal or vertical movements of the optical table, which are more likely to change the beam pointing in x direction. Because the plane of the table surface is less likely to deform and warp, the tip-/tilt-motion of the post (required to change y pointing of the beam) should inherently be more stable.

When turning the active stabilization on, one would expect to see the horizontal and vertical instability being reduced by about the same factor, assuming that the actuators responsible for driving the mirror position are identically capable. Instead, the stabilization appears much less effective in the y direction. The relative improvement is on the order of a third to a quarter of the jitter reduction in the x direction, such that, when the stabilization is on, the absolute rms jitter in the vertical direction is now larger than in the x direction. Why the stabilization of the vertical instabilities is so much less effective is not clear. A possible explanation could be the frequency of the source of vertical jitter. If differs significantly from the horizontal component and falls into a band where the MRC stabilization is less effective, the observed behavior could be explained.

Despite the unequal effectiveness of the stabilization in the horizontal and vertical plane, the total relative improvement

$$\delta(\Delta r) = \frac{\Delta r(MRC \text{ off})}{\Delta r(MRC \text{ on})}$$
(6.1)

is close to an order of magnitude reduction in rms jitter on the two following amplifier crystals. This represents a significant overall improvement and makes the setup an effective addition to stabilizing the transverse beam position in the laser system.

No pulse energy values were recorded during these first scans to assess the effectiveness of the MRC system. A first test, measuring the shot-to-shot rms jitter of the pulse energy measured destructively after the final amplification stage, revealed no obvious improvement when the MRC was activated. Its impact on long-term pulse energy stability was recorded during a later campaign and discussed in Sec.6.3.

# **6.2** Pulse Duration

During the setup and characterization of the non-invasive, on-shot pulse duration diagnostic, discussed extensively in Sec.5.2, strong, long-timescale variations of the pulse duration were observed (see Fig.14). However, it was shown that these instabilities were only resolvable when the diagnostic was in a de-tuned dispersion setting, where the pulse duration measured by the  $GRENOUILLE\ \tau_m$  fulfilled  $\tau_m \neq \tau_0$ , with  $\tau_0$  the pulse duration on target. In subsequent efforts, it was demonstrated that spectral phase variations are the main driver of these observed instabilities (Fig.16), and in Sec.5.2.5 and 5.2.7 implemented a Python-based, real-time analysis of the raw images allowing us to retrieve the pulse duration dynamics with high accuracy. This chapter will focus on attempting to find the origin of the discovered instabilities and ways to reduce or correct them.

# **6.2.1** Investigating the Source of the Instabilities

To get meaningful insight into the dynamics of the laser pulse duration and the origin of the observed, reproducible long-term variations, a dedicated long-term campaign was planned on the HTU system. Because the amplification process in the main amplifier was one of the suspected effects causing the pulse duration changes, the campaign was separated into a designated low-power (un-amplified, 2.5 mJ pulse energy) and high-power run (amplified to 3 J pulse energy) on back-to-back days. This was to ensure the study of the dynamics would be under as comparable experimental and environmental conditions as possible.

Right before this study, a malfunction of the beam stabilization system after the stretcher, which is supposed to lock the alignment through the Pockels cell, caused a hot spot that damaged the compressor and final steering mirror before the LPA target. The beam could still be sent through the compressor and onto the *GRENOUILLE* diagnostic line, but not onto the target. For this reason, even for the high power data set, no LPA or FEL results were acquired which would have enabled the study of possible correlations.

#### Low Power

To take *GRENOUILLE* data on the designated diagnostic line when analyzing the un-amplified 1 kHz laser pulse, the ND filters protecting the diagnostic under high-power conditions need to be removed. Furthermore, the exposure of the temporal camera, which records the SHG FROG images, has to be increased from 1 ms to 850 ms. At such high exposure times, the experimental control system is unable to maintain its default 1 Hz repetition rate for data acquisition. For this reason, data was only taken at 0.5 Hz repetition rate.

The result of the first scan can be seen in Fig.35: 3000 consecutive shots were taken without varying any of the experimental parameters, nonetheless the temporal second moment  $D2\sigma_{temp}$  (blue) changed noticeably during this scan. To make sure the strong correlation to the pulse duration  $\tau_m$  found under high power conditions (see Fig.29(a)) still holds true, the time-consuming post analysis of the *GRENOUILLE* images was conducted and the extracted value of the pulse duration is displayed in red in Fig.35.

When analyzing the results, it became clear that the mean pulse duration value also drifted significantly over time, from 63.5 fs during the first 500 shots (green shaded area of the plot), to 54.1 fs during the last 500 shots (orange shaded area). Similarly, the amplitude of the rms pulse duration variations also increased drastically between those two intervals, by more than

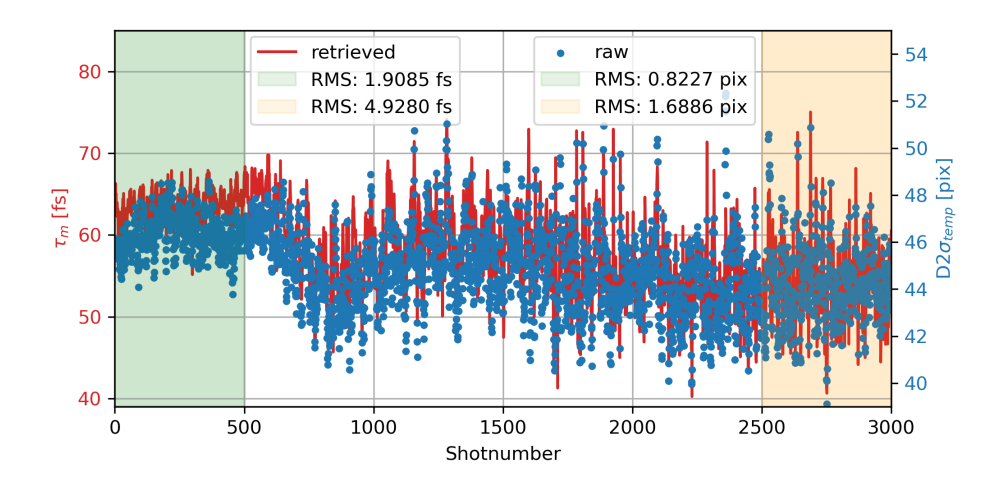


Figure 35: Change of the pulse duration  $\tau_m(\text{red})$ , as measured by the *GRENOUILLE*, and second moment of the raw images temporal axis  $D2\sigma_{temp}$  (blue) over 3000 shots at low power. The rms variation of both parameters over the first (green shaded area) and last 500 shots (orange shaded area) is calculated and displayed.

a factor of two. These dynamics match what was observed for the second moment  $D2\sigma_{temp}$  (blue) of the raw images, justifying the decision to focus solely on the real-time second moment analysis going forward.

Scan008, displayed in detail in Fig.35, was conducted under the experimental conditions expected to be the least stable. No attempt was made to stabilize the pulse duration / spectral phase. This included even turning off the MRC system on the amplifier table. The other two scans, consisting of only 1600 and 1500 consecutive shots respectively, were used to investigate the impact of different possible ways to stabilize the observed variations.

In Fig.36, the three consecutive scans are plotted over time (calculated from the shot number and previously mentioned 0.5 Hz acquisition rate). Less than 15 mins passed between the scans to change experimental configurations and device settings, therefore a common time axis was chosen to simplify interpretation of the complete dataset.

As can be seen clearly in the plot, there are significant, systematic changes of the second moment  $D2\sigma_{temp}$  (and pulse duration  $\tau_m$ ) over the course of the monitored 3+ hours of low power operation. The increase in variation amplitude, strongly noticeable in the dataset of Scan008 in Fig.35, seems to stabilize after about the first hour. The last 500 shots of Scan011 show an almost identical value of second moment  $D2\sigma_{temp}$  rms to the last 500 shots of Scan008. This suggests that the process responsible for the increase in rms jitter has stabilized after an hour of operation.

To quantify the long-term effects of  $D2\sigma_{temp}$ , in addition to the shot-to-shot instabilities, the rolling average over 100 consecutive shots was calculated for the full dataset and can be seen as the red trace in Fig.36. This averaged trace allows to quantify the overall trend of  $D2\sigma_{temp}$ , and visualizes strong drift over roughly the first and last hour of the data set.

During Scan008, as mentioned above, no attempt at stabilization of  $D2\sigma_{temp}$  was made. To determine if it has any effect on pulse duration rms fluctuations or long-term drift, the MRC system was turned on during Scan010. For Scan011 it was again deactivated, and instead a number of weights were placed on the lid of the protective housing which encloses the laser pulse

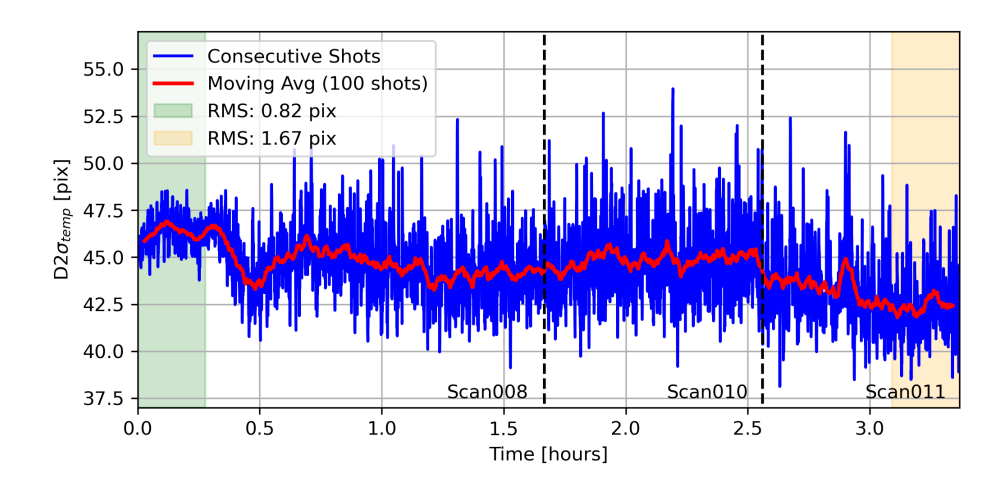


Figure 36: Monitoring the change of temporal second moment  $D2\sigma_{temp}$  from the raw GRENOUILLE images over multiple hours of laser operation at low power. Three back-to-back measurements of  $D2\sigma_{temp}$  (blue) from consecutive laser shots are plotted over operation time. The rms jitter of the second moment for the first (green shaded area) and last 500 shots (orange shaded area) is calculated and displayed, as well as the moving average (red) over 100 consecutive shots.

stretcher. This technique had previously been demonstrated to significantly reduce observed laser pulse duration variations on the Hundred TeraWatt Thomson-scattering (HTT) system. Suspected to be caused by airflow from the HVAC unit causing vibrations of the stretcher enclosure. The hope was that the observed effects on the HTU system could be stabilized the same way.

The MRC system seems to have had some effect, based on the reduced drift observed during Scan010. Calculating the standard deviation of the rolling average  $\delta(D\bar{2}\sigma)$  in the respective intervals leads to

- $\delta(\bar{D2\sigma})[Scan008] = 0.93 \,\mathrm{pix}$
- $\delta(\bar{D2\sigma})[\text{Scan010}] = 0.37 \,\text{pix}$
- $\delta(D\bar{2}\sigma)[\text{Scan011}] = 0.72 \,\text{pix}$

Despite the rms variation of  $D2\sigma_{temp}$  showing no sign of improvement between the last 500 shots of Scan008 (see Fig.35) and Scan010 and Scan011, there is a significant change in the long-term drift between the three scans. Especially the reduction by a factor of 2.5 between Scan008 and Scan010, and the increase by a factor of 2 between Scan010 and Scan011, strongly suggests the activation of the MRC beam stabilization system during Scan010 to have a profound impact on at least the observed long-term drift instability.

To verify this interpretation, the centroid  $r_{x,y}$  of the laser pulse position was calculated directly from the images capturing the beam on the second amplifier crystal. Acquired simultaneously during the three scans displayed in Fig.36, and applying the same rolling average technique as for the second moment  $D2\sigma_{temp}$ , both parameters are plotted over the scan time for comparison, as can be seen in Fig.37(a).

The averaged centroid behavior qualitatively matches expectations based on the results from Sec. 6.1 and adds new understanding of the laser pulse position dynamics. The centroid rms jitter is much reduced and drift seems to have been eliminated completely, when the MRC system

is active (Scan010, green shaded area). Outside of that interval, during Scan008 and Scan011, both shot-to-shot variations and long-term drift are of significant scale. Correlating the two parameters, as can be seen in Fig.37(b) and (c), shows a measurable correlation between them with the MRC turned off, that vanishes completely when the beam stabilization is activated.

Insightful conclusions can be drawn from the above observations. Firstly, if the MRC is not active, the laser pulse centroid drifts noticeably when passing through the main amplifier, even under low power conditions (when the crystals are not pumped). This result was unexpected, which is why previously the MRC had not been activated during low power operations. Turning on the MRC system reduces shot-to-shot and long-term drift instabilities of the beam centroid very effectively, even at low power.

Secondly, at least a significant part of the observed long-term drift of the laser pulse duration is correlated to drift of the laser beam position on the amplifier table. This is demonstrated nicely when comparing the correlations between  $D2\sigma_{temp}$  and  $r_{x,y}$  when the MRC system is deactivated (Fig.37(b)) versus when it is activated (Fig.37(c)).

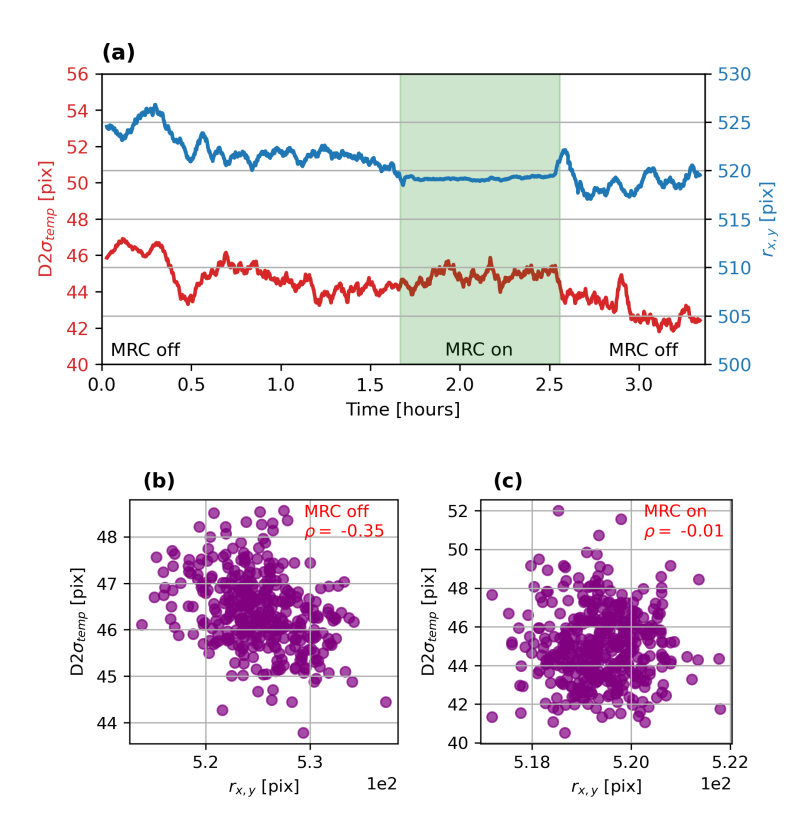


Figure 37: Comparing the dynamics of averaged second moment of the GRENOUILLE raw images temporal axis  $D2\sigma_{temp}$  (red, correlated to laser pulse duration) to the centroid of the beam position on the second amplifier crystal  $r_{x,y}$  (blue) under the un-amplified (low power) conditions. In (a), the trend of both over time is plotted. (b) shows the direct correlation between the parameters with the MRC system turned off, and (c) the correlation with the MRC system turned on.

Knowing that operating the MRC system can not only stabilize the beam position shot-to-shot, but effectively eliminate its drift on the amplifier crystals and simultaneously significantly reduce slow changes of the laser pulse duration, is a highly valuable result.

The stretcher enclosure reinforcement added for Scan011 seems to have had no effect on the

temporal laser pulse dynamics. Both the drift and rms jitter of  $D2\sigma_{temp}$  show no significant improvement compared to Scan008, which seems to indicate the observed effects are not caused by the air currents from the HVAC unit vibrating the stretcher housing. This leads to the conclusion that the instabilities are either inherent to the low power pulse coming out of the laser front end, or are originating from after the stretcher. The observation from Fig.37 seems to match this interpretation, suggesting that at least a significant part of the pulse duration drift is caused by slow changes of the beam centroid in the laser amplifier.

To further investigate temporal laser pulse performance, this investigation was repeated under high power conditions.

#### **High Power**

Due to the afore mentioned damage to one of the compressor gratings and final steering mirror, the beam was not amplified to the maximum 4 J of pulse energy, but instead to only 3 J. The intention was to reduce the risk of destroying more beamline components after the compressor, by avoiding to introduce more hot spots in the beams intensity profile downstream of the damaged grating.

The ND filters, which had been removed from the *GRENOUILLE* diagnostic line for the low power studies, were implemented again and the exposure of the camera acquiring the SHG FROG images set back to 1 ms. Due to other unrelated control system issues, the data acquisition frequency still only averaged to about 0.75 Hz, instead of the ideal 1 Hz repetition rate of the amplified laser pulse.

With the experimental setup restored to its default configuration for high power operation, no additional effort was made to confirm the amount of dispersion on the diagnostic line. While the low power data was acquired in the stretched configuration of  $\tau_m \neq \tau_0$ , with  $\tau_m \approx 60$  fs, the amplified beam with the added dispersion from the ND filters was closer to ideal compression,  $\tau_m \approx \tau_0$  with  $\tau_m \approx 37$  fs. This was only discovered during the data analysis when running the post retrieval on the *GRENOUILLE* data, to correlate pulse duration  $\tau_m$  and second moment  $D2\sigma_{temp}$ .

Based on previous observations, as can be seen in Figs.15 and 22, the temporal pulse properties in the compressed configuration ( $\tau_m = \tau_0$ ) do not reveal any insightful correlations to LPA parameters, and when monitored over extended periods of time show no noticeable variations (see Fig.14). This suggested there would be no insights gained into the long-term temporal dynamics under high power conditions, as opposed to the low power results discussed previously.

Surprisingly, the long-term analysis of all three scans conducted at high power still shows very strong time-dependent dynamics of the resulting  $D2\sigma_{temp}$  traces, as can be seen in Fig.38. Scan005 and Scan007 were taken under identical experimental conditions, with the weights on the stretcher cover as added for the last scan of the low power study, and the MRC system turned off. There was a thirty-five minute interruption between Scan007 and Scan009, due to removal of the weights from the stretcher enclosure. The MRC system remained turned off during Scan009.

As can be seen in Fig.38, the high power pulses temporal second moment appears comparatively stable during the first scan. The rms jitter of the first 500 shots is lower than observed during the corresponding low power scan, and there seems to be no noticeable drift of the average value of  $D2\sigma_{temp}$ . No noticeable change in the average  $D2\sigma_{temp}$  value is observed be-

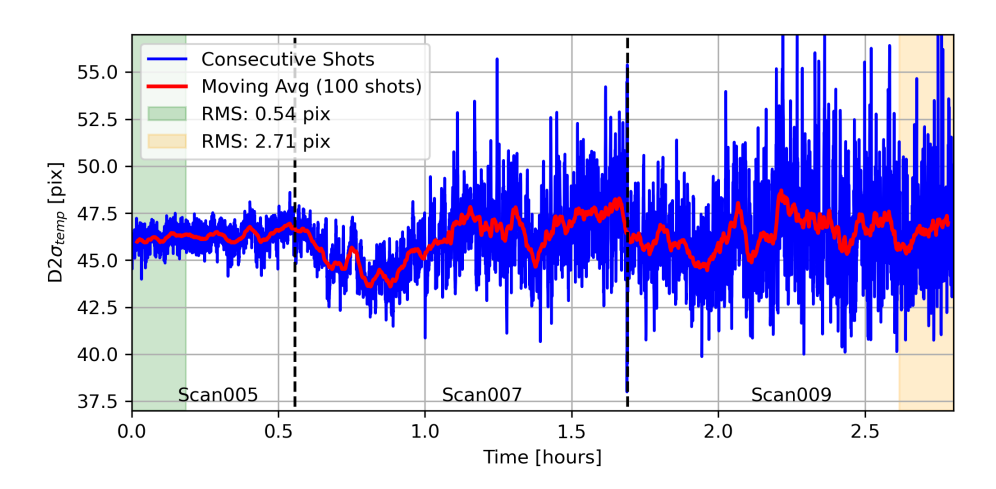


Figure 38: During high power operation, the change of the temporal second moment  $D2\sigma_{temp}$  of the laser pulse is monitored non-invasively over multiple hours of operation. Three back-to-back datasets of  $D2\sigma_{temp}$  (blue) are displayed, each under static experimental conditions. The rms variation of the second moment for the first (green shaded area) and last 500 shots (orange shaded area), as well as the moving average (red) over 100 consecutive shots, are calculated and displayed.

tween Scan005 and Scan007, buy shortly after the start of Scan007 strong long-term drift and shot-to-shot jitter start to appear. Both the jitter and long-term drift of the average  $D2\sigma_{temp}$  seem to increase significantly throughout the dataset of Scan007. The removal of the stretcher reinforcement before Scan009 does not appear to systematically impact the observed stability of  $D2\sigma_{temp}$  in a noticeable way. Instead, the trend of increasing shot-to-shot jitter and long-term drift seems to continue. These observations are supported by the  $5\times$  increase in calculated rms jitter of  $D2\sigma_{temp}$  between the first and last 500 shots.

# 6.2.2 Summary

The most notable discovery, when comparing the observations under low (Fig.36) and high power conditions (Fig.38), is that there appears to be no fundamental difference between the two cases. Despite the variation of some external parameters between scans (amplification of the laser, operation of the MRC system, reinforcement of the stretcher enclosure), they exhibit a very similar overall behavior. The amplification process was suspected to be one of the key origins of the observed temporal pulse parameter instabilities, which appears to have been an incorrect assumption. This is supported by the observations from the low power test, assigning the source of the variations to the laser front end, or beam position drift in the main amplifier. The noticeable increase in shot-to-shot rms variation of  $D2\sigma_{temp}$  between the first and last 500 shots of the acquisition period was reproduced in both experiments.

When investigating the impact of reinforcing the stretcher enclosure at low and high power, it was discovered that this does not appear to have any measurable impact, neither on shot-to-shot variation, nor long-term drift of  $D2\sigma_{temp}$ .

Instead, the length of system operation appears to be a factor of high impact to the scale of the instabilities in both pulse energy regimes. It can be stated with a high degree of confidence that the rms jitter and long-term drift of  $D2\sigma_{temp}$  increase with operational time of the laser system.

Additionally, studying the impact of the MRC beam stabilization system on the beam centroid and temporal second moment under low power conditions, revealed the long-term drift of both parameters to be correlated.

The importance of being able to resolve all of the above discussed temporal dynamics of the laser pulse, even in the compressed configuration of  $\tau_m = \tau_0$ , can not be overstated. While it has proven impossible to extract this information from the retrieved pulse duration and linear chirp parameter close to or at compression, the temporal second moment  $D2\sigma_{temp}$  can not only be determined from the raw images in effectively real time, but also appears to be much more sensitive. This makes it an even more capable and important tool for this non-invasive, on-shot pulse duration diagnostic going forward.

# 6.3 Combined Pulse Energy and Duration Stabilization Study

In Sec.6.1, the process of setting up and characterizing a stabilization system for the beam centroid in the HTU system multi-pass amplifier was described in detail. The intention was to reduce the long-term drift of the laser pulse energy  $E_P$ , correlated to the change in centroid position on the amplifier crystals, observed when operating the system continuously over many hours. First results showed a reduction in centroid rms jitter of about an order of magnitude on the two amplifier crystals downstream of the MRC. But no conclusive proof of successful stabilization of  $E_P$  during high power operation has been shown.

Long timescale variations of the pulse duration, discovered after setting up an on-shot, non-invasive pulse diagnostic (described in Sec.5.2), were investigated in detail in Sec.6.2, to narrow down the origin and find ways to stabilize the instabilities. Comparing data from low and high power campaigns led to the conclusion that there are two seemingly independent contributions to the effect.

- 1. The "fast" component (tens of seconds), which increases over time, appears to occur irrespective of amplification or efforts to stabilize the stretcher or beam pointing. This leads to the conclusion that this component must be inherent to the front end of the laser.
- 2. The "slow" component (tens of minutes to hours) is a systematic drift of the temporal second moment (and therefor the pulse duration) observed irrespective of amplification. However, this component was discovered to be impacted by the beam pointing stabilization on the amplifier table. Under low power conditions, a reduction in long-term drift of over 60% was observed when turning on the MRC system.

These observations led to conducting a designated study of the impact the MRC stabilization has on  $E_P$  and  $D2\sigma_{temp}$  under high power conditions.

#### 6.3.1 Results

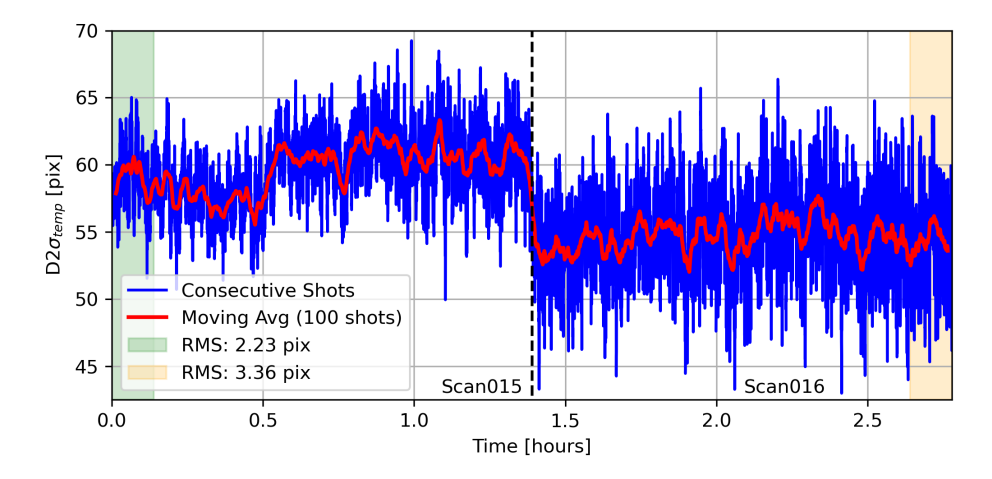


Figure 39: Change of  $D2\sigma_{temp}$  (blue) over multiple hours of high power operation. The rolling average (red) over 100 consecutive shots is displayed for both back-to-back scans. The MRC beam stabilization system was turned off for Scan015 and turned on for Scan016. The rms jitter of  $D2\sigma_{temp}$  for the first (green shaded area) and last 500 shots (orange shaded area) are calculated and displayed.

5000 shots at 1 Hz repetition rate of the main pulse (amplified to 4 J energy) were taken with the MRC system turned off, immediately followed by another 5000 shots with the MRC system turned on. The change in  $D2\sigma_{temp}$  over the course of the experiment is displayed in Fig.39, following the same methods used in the display of temporal second moment behavior in Figs.36 and 38.

Again, the familiar effect of the "fast component" shot-to-shot variations increasing over time can be observed. The rms jitter of  $D2\sigma_{temp}$  increased from 2.23 pix during the first 500 shots of Scan015 (MRC off) to 3.36 pix in the last 500 shots of Scan016 (MRC on). This represents an increase in rms of 51% over the course of slightly over 2.5 hrs of high power operation, and confirms an observation made previously during low power operation that the MRC system does not appear to improve the shot-to-shot stability of  $D2\sigma_{temp}$ .

However, when calculating the standard deviation of the rolling average  $\delta(\bar{D2}\sigma)$  for the case of the MRC system off (Scan015) and MRC system on (Scan016), in an effort to quantify the long-term drift of  $D2\sigma_{temp}$ , a 33% improvement is found:

- $\delta(\bar{D2\sigma})[\text{Scan015}] = 1.67 \,\text{pix}$
- $\delta(\bar{D2\sigma})[\text{Scan016}] = 1.12 \,\text{pix}$

Despite being a less significant improvement than what was found under low power conditions, this result qualitatively matches the previous observations and confirms the ability to stabilize at least the long-term drift of  $D2\sigma_{temp}$  and in turn the pulse duration  $\tau$ , when stabilizing the laser beam centroid on the amplifier table with the MRC system.

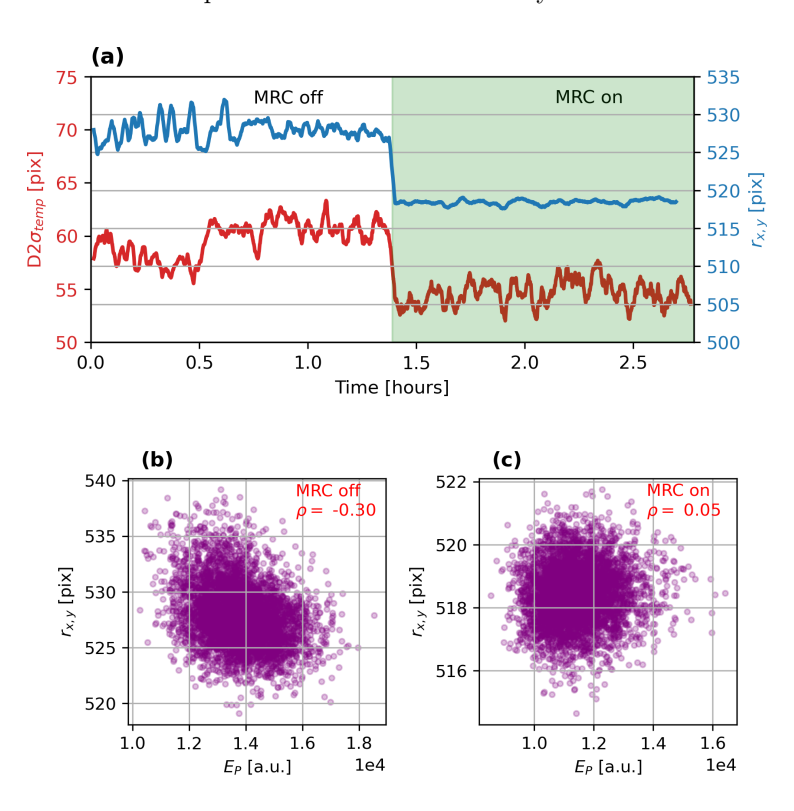


Figure 40: Impact of the MRC beam pointing stabilization over multiple hours of high power operation. (a): Comparing the short- and long-term instabilities of the averaged beam centroid on the amplifier  $r_{x,y}$  (blue) and the averaged temporal second moment  $D2\sigma_{temp}$  (red) in the case of MRC off and on (green shaded area). (b): Correlation between  $r_{x,y}$  and laser pulse energy  $E_P$  with MRC turned off and (c) MRC turned on.

To investigate the impact that stabilizing the beam centroid  $r_{x,y}$  has on the pulse energy  $E_P$ , the peak counts detected by a camera imaging the main beam after the final amplifier were used as a proxy (the on-shot energy meter E in Fig.5 was not in commission). As can be seen in Fig.40(a), the behavior of  $r_{x,y}$  observed for turning the MRC on and off matches the observations made previously at low power, as can be seen in Fig.37(a), effectively eliminating long-term drift and significantly reducing shot-to-shot jitter. The averaged temporal second moment  $D2\sigma_{temp}$  was plotted to enable direct comparison between the two parameters in the two regimes.

As demonstrated for  $D2\sigma_{temp}$  in the low power case (see Fig.37(b) and (c)), under high power conditions the correlation between the pulse energy  $E_P$  and  $r_{x,y}$  is drastically reduced from  $\rho = -0.30$  with the MRC off (Fig.40(b)) to  $\rho = -0.05$  when the MRC is turned on (Fig.40(c)).

The results of this combined study, under conditions matching high-power LPA operation, demonstrate effective stabilization of the laser pulse energy and pulse duration against long-term drift, when stabilizing the laser beam centroid in the multi-pass amplifier.

#### 6.4 Wavefront Stabilization

The results shown and discussed in this section were part of a collaborative effort between the BELLA Center and *RadiaSoft*, and the corresponding publication to the results discussed in this section is

Kyle Jensen, Samuel Barber, Curtis Berger, Chris Doss, **Finn Kohrell**, Stephen Coleman, Nathan Cook, Jonathan Edelen, Joshua Einstein-Curtis, and Jeroen van Tilborg *Improved laser-plasma accelerator stability via high-bandwidth longitudinal focal position stabilization of 100 TW-class laser system*, Phys. Rev. Accel. Beams - in review

#### 6.4.1 Motivation

With the high degree of correlation between the fluctuations of the laser pulse, the accelerating plasma structure, and LPA electron beam it generates, it is not surprising that not just the transverse but, specifically, also the longitudinal focal position instability has been found to be a strong driver of observed fluctuations of electron beam spectra [10].

On the HTU system, changes of the longitudinal focal position are determined by calibrated conversion from the non-invasively monitored laser beam wavefront radius of curvature (RoC). Over a full day of high-power operation, short-term jitter of up to  $\pm 2\,\mathrm{mm}$  has been observed, with long-term drift exceeding 5 mm. The HTU system employs the density down-ramp injection scheme (see Sec.1.2.2), which has a highly localized injection region defined by the location of the high density shock. Especially for this reason, longitudinal variations on the order of the laser pulse Rayleigh range can be expected to drastically limit the performance of the generated electron beams shot-to-shot, and effectively prohibit multi-hour continuous operation with stable electron beams, which is crucial for conducting LPA-driven FEL studies.

# **6.4.2** Setup

To enable active control and closed-loop stabilization of the RoC, a transmissive telescope with variable lens separation is set up between the second and third multi-pass amplifier (T 2 in Fig.5). By mounting the downstream lens of the telescope pair on a moving magnet linear translation stage from Zaber, which allows for sub-µm precision and ms-response time to movement requests, the longitudinal focal location can be effectively adjusted with a precision of roughly 100 µm.

The desired capability for active feedback was implemented through the setup of a Shack-Hartmann wave-front sensor (WFS) from *Thorlabs* on the ghost beam line. As mentioned in Sec.4.1, the ghost beam has been shown to allow non-invasive monitoring of the transverse and longitudinal focal position on-target.

The RoC values calculated from the WFS data are sent to a closed-loop PID controller, calculating the required move of the telescope stage to keep the longitudinal focal position at its pre-determined setpoint location.

Because the WFS is measuring the non-amplified kHz train of background pulses, which has a RoC highly correlated to that of the amplified 1 Hz pulse train, the active correction of

the amplified laser can be conducted at repetition rates exceeding 1 Hz. Depending on the set exposure time and spatial resolution, up to 880 Hz acquisition rate can be realized. For the results presented here, and the subsequent LPA operation, the WFS was operated with a 32 Hz acquisition rate.

### 6.4.3 Results

During high-power LPA operation, assessing the effectiveness of stabilizing the longitudinal focal position of the 1 Hz amplified laser pulse led to the results displayed in Tab.4. Measured over 500s each with the longitudinal focal stabilization (LFS) off and on, a reduction in rms standard deviation of the longitudinal focal position by 40% was observed.

Simultaneously taken electron spectra revealed an impressive improvement of LPA stability correlated to the LFS performance, reducing the rms variations of average bunch energy by 52%, the mean energy spread by 19% and rms fluctuation of the energy spread by 37%. These improvements in electron beam quality with activating the LFS culminated in a 80% reduction in the number of "missed" shots, for which a bunch charge of less than  $5\,\mathrm{pC}$  was recorded.

Table 4: Results of longitudinal focal stabilization at high-power during LPA operation.

	Stabilization off	Stabilization on
Long. focal position [mm]	$\pm 0.46$	$\pm 0.28$
Avg. Energy [MeV]	$120.3 \pm 18.9$	$111.1 \pm 9.1$
Energy Spread (rms) [%]	$5.3 \pm 3.0$	$4.3 \pm 1.9$
Charge [pC]	$19.4 \pm 17.9$	$40.4 \pm 20.4$
Missed Shots $(< 5 \mathrm{pC})$	145~(29%)	32~(6%)
Correlation (long. focal pos. vs charge)	-0.64	-0.48

In addition to this noticeable improvement of the quality of generated electron beams on a shot-to-shot timescale, the LFS system also completely eliminates long-term drift of the longitudinal focal position of the amplified laser on-target. Given the scope of this effect before the implementation of the LFS, this added stabilization capability represents a tremendous achievement and step towards enabling long-term, stable LPA-driven FEL operation on the HTU system.

# 6.5 Summary

This section focused on the implementation of diagnostics and active stabilization systems to detect, quantify and mitigate instabilities of the laser pulse affecting the reliability of the HTU systems LPA source. Especially the observed long-term drift of pulse energy, and longitudinal focal position were limiting the ability to run extensive LPA-driven FEL studies, but slow variations of the pulse duration had also been observed and correlated to impact the LPA performance.

The installation of a commercial two-stage beam stabilization system from MRC Systems between the first and second multi-pass amplifier, discussed in Sec.6.1, led to an improvement of transverse beam centroid rms  $(r_{x,y})$  on the downstream amplifiers by about an order of magnitude.

During the commissioning of the non-invasive, on-shot pulse duration diagnostic (described in Sec.5.2), systematic variations of the pulse duration over tens of seconds to minutes of operation time had been observed. In Sec.6.2, dedicated campaigns conducted to quantify the effect and find a way to stabilize it were discussed.

First, the validity of using the temporal second moment  $D2\sigma_{temp}$ , extracted from the raw GRENOUILLE images as a proxy for the pulse duration was demonstrated. This enabled real-time analysis compared to the application of post-analysis retrieval algorithms, taking up to  $30 \,\mathrm{s}$  per data point (acquired at  $1 \,\mathrm{Hz}$ ).

Afterwards, studies of both the un-amplified and fully amplified laser pulse were conducted, to learn about possible influences of the amplification process on the observed instabilities. In both cases, schemes to reinforce the housing of the pulse stretcher were tested, but proved to have no noticeable impact.

However, under both low and high power condition the same general trends of  $D2\sigma_{temp}$  were observed. A significant increase in short-term jitter and long-term drift over multiple hours of operation seemed to strongly suggest the source of the instabilities to be not directly connected to the amplification process, as previously assumed.

Running the MRC system during the low power investigations showed that the stabilization of the beam centroid  $r_{x,y}$  significantly reduced long-term drift of  $D2\sigma_{temp}$ , giving rise to the hope that both pulse duration and energy could be stabilized with reducing the instability of the beam centroid in the amplifier.

A combined campaign discussed in Sec.6.3, measuring  $\tau$  and  $E_P$  during high power operation, was conducted to specifically study the impact of the MRC system on long-term stability of both LPA parameters. The results confirmed previous observations made at low power, and showed noticeable improvement of both pulse duration and energy stability over multiple hours of operation, when the MRC system is active.

This makes the stabilization of the transverse beam centroid  $r_{x,y}$  on the amplifier table a highly capable tool in enabling stable, long-term LPA-driven FEL operation.

Sec.6.4 focuses on mm-scale drift of the longitudinal focal position, observed repeatedly when running the laser system at high power over multiple hours. Therefore, a system designed to measure and stabilize the pulse wavefront RoC was devised. Based on a WFS installed on the "ghost line", the RoC of the 1 kHz pulse train was measured non-invasively. Operated

in closed-loop with a motorized linear stage in the transmissive telescope between Amp2 and Amp3, the RoC can be stabilized and long-term drift completely removed.

The impact on LPA performance is significant, not only eliminating the need to re-optimize overlap between focal position and plasma down-ramp target multiple times per day, but noticeable improving the stability of electron beam energy, energy spread, and charge.

As discussed in this section, the newly implemented diagnostic and stabilization capabilities on the HTU system play a key role in enabling reliable, long-term LPA operation. This improved performance of the electron beam source proved to be vital to the effort of demonstrating stable, high-gain and long-term LPA-driven FEL operation.

At the start of this thesis project, the main focus on the HTU experiment was to generally improve the performance of the system enough to allow reliable generation of electron beams of high enough quality to send to the undulator and enable FEL lasing. This chapter will give an overview of the progress that happened since then, which enabled the observation of first undulator light on the system, and later the demonstration of unprecedented levels of gain and long-term stability for an LPA-driven FEL.

# 7.1 First undulator radiation observed

After continuous efforts to improve LPA performance, in April of 2023 it became possible for the first time to send optimized electron beams past the magnetic spectrometer (MagSpec 1 in Fig.46) on a regular basis. Even though the majority of time was still spent on source optimization, multiple hours of electron beam trajectory and focusing studies, conducted by scanning steering magnet and EMQ triplet currents, became a regular part of HTU high power operations.

Virtual references on the phosphor screens upstream of the undulator (A 1 - A 3, see Fig.7) were used to align the electron beam to what was believed to be an accurate representation of the VISA undulators' magnetic axis. To achieve optimal focusing of the electron beam on the final transverse beam profile monitor before the undulator entrance A 3, extensive studies were conducted to scan the currents on the EMQ triplet, which caused the introduction of noticeable horizontal dispersion of the electron beams. Considerable work went into experimentally determining and referencing the magnetic axis of the EMQ triplet, to avoid any steering or dispersion introduced by optimization of electron beam focusing.

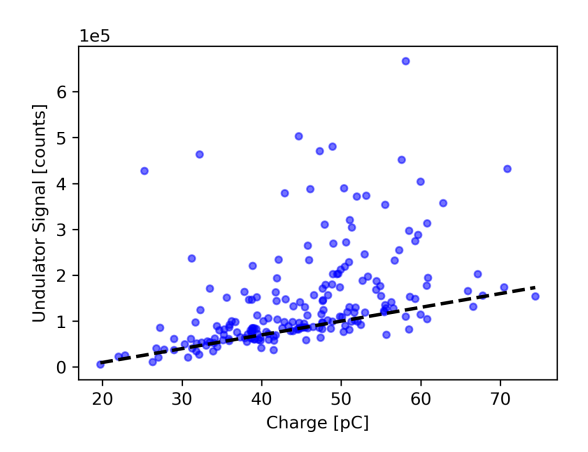


Figure 41: Integrated undulator radiation signal over charge, measured on 04/20/2023. The black dashed line indicates the potential scaling of incoherent undulator emission.

Sending focused electron beams on the such optimized trajectory into the undulator quickly revealed the first, very weak indications of undulator radiation. Deliberate misalignment of the beam by use of the dipole magnet of MagSpec 1 upstream of the undulator, strong enough steer it fully into the phosphor screens of the spectrometer and miss the undulator entrance, quickly

revealed that the signal was not simply stray laser or plasma light.

Within two weeks of operation under these conditions, multiple demonstrations of what appeared to be predominantly incoherent undulator radiation were achieved. As can be seen in Fig.41, the majority of shots seems to follow a linear trend of undulator signal with bunch charge (visualized by the black dashed line). The shots lying significantly above this apparent linear trend appeared as noticeably brighter flashes on the camera and could be first evidence of coherent emission, an exemplary image such shots recorded on the optical spectrometer can be seen in Fig.30.

Despite these promising first results, the system lacked key diagnostic capabilities to quantify important properties of the electron beam before and after the undulator. Furthermore, because the undulator radiation signal was to be used as the main metric to assess LPA-driven FEL performance, the detection and quantification of it needed to be significantly improved by UV-enhancing and energy calibrating the optical spectrometer. Other early issues included the lack of spatial resolution of the transverse electron beam profile on the phosphor screens upstream of the VISA (A 1 - A 3), no direct way to confirm and measure the incoherent emission scaling, as well as no reliable way to determine bunch charge and energy after the undulator. In addition, the performance and stability of the laser system itself seemed to cause significant problems when trying to generate stable, low energy-spread electron beams at 100 MeV, able to support hours of continuous electron beam transport and FEL optimization studies.

# 7.2 Crucial Increase of Laser System Performance

An important part of establishing LPA-driven FELs as a viable technology for future compact light source facilities is to demonstrate "turn-key" operation of the entire setup. This requires exceptional stability of the laser system not just during, but also between machine operation, such that an immediate return to reliable production of stable electron beams after hours or days of down-time can be facilitated.

In this specific effort, there has been tremendous progress on the HTU system over the last three years covered in this thesis. The time required between laser start-up and achieving stable electron beam generation at 100 MeV has been reduced from 6-8 hrs in September of 2022 to less than 2 hrs in the most recent experiments. This time includes the "search-and-clear" procedures required before sending the high-power laser pulse to the target area. If the lab was already in the "cleared" state before starting the laser, this would bring the time required to achieve electron beam generation down to less than 90 mins. Some of the key steps of achieving this drastic improvement and progress towards "turn-key" operation and their specific impact will be discussed in this section.

# 7.2.1 Laser Front End Operation

The laser front end, based on the *Vitara* oscillator and *Legend* regenerative amplifier (see Sec. 4.1 and Fig. 5), used to be turned on every morning as part of laser start-up and shut down at the end of each day, to increase the life-expectancy of its componentry. However, over the course of over a year of this mode of operation, a slow but constant energy loss of the 1 kHz beam was observed. This manifested itself as a decrease in output power of more than 20% over the course of a few months, and was eventually connected to algae build-up in the chiller system. Flushing and disinfecting the cooling system would briefly solve the problem and return the system to its design output, but the slow degrading effect would re-appear after a few weeks.

Because this introduced not only a constantly varying pulse energy, but also the need for regular intervention and interruption of front-end operation, the decision was made to test running the system continuously throughout the week and only shut it down only over the weekend. The hope was to slow down algae build-up by reducing the time the chiller system would sit inactive, which turned out to be highly effective in increasing output stability. Changing the operation procedures accordingly, the observed decrease in output power was reduced from > 20% to < 5% over a comparable time-frame. After setting the output power back to its desired value, this change to the operating procedure has so far enabled almost a year of operation without impactful energy loss and the need for chiller maintenance.

# 7.2.2 Laser Alignment and Active Stabilization

Over the course of time covered in this thesis, significant changes were made to the active stabilization infrastructure of the laser system.

The added capabilities for fast corrections of beam pointing and radius-of-curvature (RoC) in the amplifier setup, discussed extensively in Secs. 6.1 and 6.4, also make initial alignment of the laser system in preparation for LPA operation more efficient.

By precisely defining a setpoint for the beam position on both PSD detectors of the MRC system once, when the beam is set to its design trajectory through the amplifier and subsequent beamline towards the target chamber, the return to this alignment on a following day was made substantially less cumbersome. Effectively, simply activating the MRC system after sending the beam to the amplifier will reproduce the previously set trajectory. Additional manual alignment of the beam position on the amplifier table, into the compressor chamber, and onto the target is usually only required once at the beginning of the week, after two days of actual laser shut-down.

Even this procedure, and potential small additional corrections during the week, have been substantially simplified and accelerated by the implementation of motorized alignment references. An iris, mounted on a pneumatic actuator right after the multi-pass amplifier, can be remotely inserted into the beam-path. It thus allows for remote and simple confirmation of the beam pointing on all down-stream references.

A set of ceramic plates at various locations in the vacuum system, each mounted on an individual linear translation stage, can be inserted into the beam path. Imaging the inserted ceramic plates with cameras outside of the vacuum system allows to check the alignment without the need to vent the system. In the target chamber, a pair of such plates installed before and after the interaction point enables precise characterization of the trajectory incident on the LPA target. Adjustments to the beam trajectory can be made through piezo-actuated mirror mounts if necessary, enabling the system operator to go through a full system alignment in a few minutes, entirely from the control room.

The LFS system allows to quickly determine, manipulate, and stabilize the longitudinal focal position of the laser on target. This significantly enhances the repeatability of LPA operation, because the time required to re-optimize the overlap between longitudinal focal location and down-ramp plasma target during every high-power campaign can be greatly reduced.

In addition to the stabilization techniques discussed above, the schemes for correction of slow drift of the laser beam centroid position through the Pockels Cell onto the amplifier table, as well as on the LPA target, unlocked more stable and reproducible alignment of the whole laser system.

Set up in a simple single-stage design, the custom beam stabilization systems are based on the in-house developed control system architecture. A set of stepper motor actuators drive an optical mount to stabilize the laser beam centroid, measured in real-time on a designated CCD camera in the experimental system, to a user specified position in the image. Because the control system operates on the 1 Hz trigger of the amplified laser beam, this stabilization technique is only applicable reliably to slow corrections, and used to compensate for long-term drifts in areas of the setup not already covered by faster active stabilization systems.

For this slow drift correction, the custom single-stage system has proven highly useful. Flexible and quickly adjustable through the integration into the native control system, it serves as a powerful tool to effectively lock the beam centroid in areas where long-term drift is noticeable and correction is especially crucial.

Finally, a designated effort has been made over the past few years to set more alignment references, improve documentation of the system and develop detailed procedures to help make operation of the entire system more efficient, repeatable and safe. This covers everything from laser start-up, amplifier alignment, setting new PSD setpoints for the *MRC* system, cleaning

and aligning the compressor gratings, to procedures for venting and pumping down the vacuum system, or swapping high-pressure helium bottles for the LPA target gas jet supply. The impact of these procedures is harder to quantify, but they have strongly improved the ability to familiarize new team members with the system, and provided a way to ensure everyone is following the exact same steps when preparing, maintaining, and operating the system. Thereby, they have definitely improved the teams' ability to operate in a stable and reproducible way. Copies of the detailed procedures developed and contributed to by the author can be found in Sec.10.2 of the Appendix.

# 7.2.3 Improvements of Laser Beam Quality

The observed instability of the LPA interaction, and generated electron beams in the early stages of this research project were at least partially assigned to the drive laser. A significant effort was made to improve the homogeneity of the high-power transverse beam profile after the final amplifier (as can be seen in the top left of Fig.42), laser pulse energy transmission from the amplifier to the LPA target, and pulse wavefront (top center image in Fig.42) to enhance the transverse mode quality at focus (top right image in Fig.42).



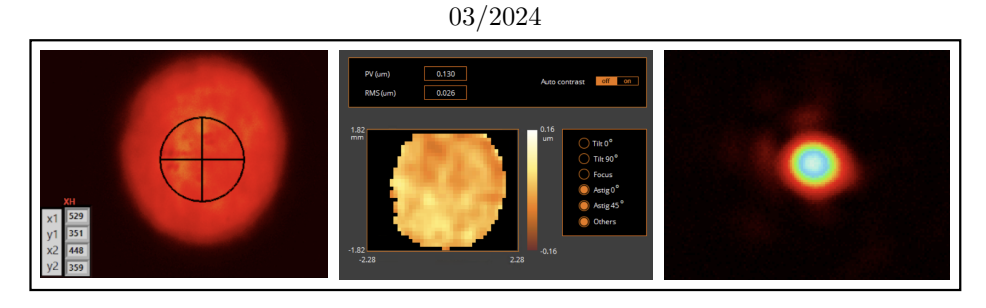


Figure 42: Comparison of transverse beam profile after the final amplifier (left), wavefront quality at DM surface (center), and mode quality at focus (right), between 04/2023 (top) and 03/2024 (bottom).

A much more homogeneous transverse beam profile after the first amplification stage was achieved through a complete re-configuration of the first multi-pass amplifier. The beam path of the GAIA laser was changed to pump the first amplifier crystal (Amp 1 in Fig.5) from both sides, instead of just from one side during previous operation. This allowed a reduction of pump fluence and extracted gain on the subsequent amplifier crystals, which further smoothed the intensity profile after the final amplifier as can be seen when comparing the top and bottom left images of Fig.42. Note that the argument presented here is specifically regarding the quality of the transverse beam profile, and not the alignment with respect to the virtual crosshair in the images.

The deformable mirror (DM in Fig.5) is a crucial tool to achieve the flat wavefront necessary for a high-quality transverse mode at focus. Over time the response of the individual actuators had degraded, leading to a correlated increase in minimum achievable wavefront peak-to-valley (PV) and rms. As can be seen in the top center image of Fig.42, the best beams that could be generated on the HTU system under these conditions had a wavefront PV of 477 nm, and rms of 49 nm. During a service visit from *ImagineOptics* the DM was confirmed to be in need for repair. Fixing this issue required shipping the DM back to the factory in France, and because the beam quality without the DM in the laser system was too poor to generate any stable electron beams, this caused a seven month break in LPA operation.

During this time, a variety of diagnostic upgrades were implemented into the HTU beamline, and significant work went towards ensuring the highest possible energy transmission through the system. For this purpose, all key optics in the beamline were inspected for damage and darkening due to high incident fluence. If possible components were cleaned in situ, otherwise the optics (such as the 40 cm diameter compressor gratings) were removed, cleaned and re-installed. Damaged optics were replaced. Afterwards, a thorough re-alignment and careful update of effectively all references was conducted, specifically with the purpose in mind to make day-to-day alignment in the future easier and more repeatable. After the DM returned fully functional and was re-integrated into the system, the results showed significant improvements of all targeted metrics of laser performance.

A reduction in wavefront rms (increased flatness) by 50%, from previous 49 nm to 26 nm, was measured (center images in Fig.42). The wavefront PV improved by 73%, from 477 nm to 130 nm. This led to a strongly noticeable improvement in mode quality at focus, as can be seen in the right images of Fig.42. The cleaned and replaced optics, as well as elimination of clipping in the beam path during the extensive laser system re-alignment, led to a relative increase in energy transmission by almost 20%, from 55% to 64% total energy transmission (between the energy output after the final amplifier and the value measured on target).

# 7.3 Confirmation of improved Electron Beam Stability and "Turn-Key" LPA Performance

During the very first high power run after the laser system was re-commissioned, which was described in detail in the previous Sec.7.2, the strong impact the discussed additions and improvements to the setup had on the LPA performance became clear.

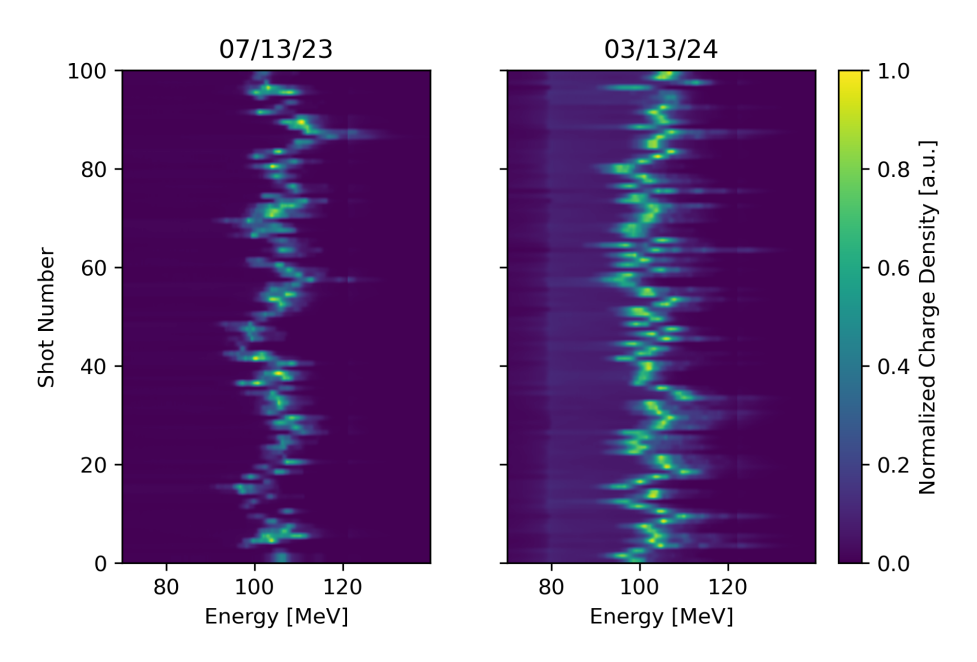


Figure 43: Electron beam spectra recorded on the magnetic spectrometer before the VISA undulator (MagSpec 1 in Fig.46) before (07/13/23) and after (03/13/24) extensive improvements to the laser system. The charge density (intensity) in both plots was normalized individually to allow comparing their relative charge density fluctuations.

It took less than an hour of LPA optimization to generate electron beams of higher quality than anything previously demonstrated on the HTU system, which can be seen in Fig. 43. The beams on 07/13/2023 (before the system improvements) exhibited an rms jitter of 5.1 MeV in central energy, 42% in charge density, and 56% in bunch charge. Eight months later on 03/13/2024, during the first high power run after the work described in Sec.7.2, the electron beams showed a much lower rms jitter of 3.9 MeV in central energy (20% reduction), 17% in charge density (60% reduction), and 11% in total bunch charge (80% reduction). Only the energy spread got slightly worse, see Tab.5 below. This might be explained by the low energy tail present in the right waterfall plot (03/13/2024, Fig.43), which was reduced in later high power runs by specifically optimizing the LPA parameters and adjusting the position and width of the tungsten slit in the magnetic chicane (see Fig.6 in Sec.4.2).

Utilizing these electron beams of unprecedented stability and sending them down-stream towards the VISA undulator, only one hour of electron beam trajectory and focusing optimization was required to recover the generation of coherent undulator radiation. After over eight months without FEL operation, this concluded a highly promising first LPA campaign.

The HTU system went back to regular high power operation after the encouraging first results discussed above. With the extensive improvements to the overall performance and stability of the laser system, turn-key operation of the LPA-driven FEL was effectively demonstrated

**Table 5:** Statistics of the electron beam parameters extracted from the spectra displayed in Fig.43. Note that the charge density was normalized for both spectra individually, affecting charge density and the integrated charge values.

	07/13/2023	03/13/2024
Avg Central Energy [MeV]	$106.5 \pm 5.1$	$99.2 \pm 3.9$
rms Energy Spread $[\%]$	$1.95 \pm 0.85$	$2.50\pm1.55$
Avg Charge Density [a.u.]	$0.52 \pm 0.22$	$0.76 \pm 0.13$
Avg Charge [a.u.]	$11.36 \pm 6.37$	$28.04 \pm 3.16$

for the first time about two months later (06/05/24), after the implementation of the LFS system (described in Sec.6.4). Following the initial alignment of the laser system and optimization of the LPA on Day 1, on Day 2 the activation of all stabilization systems integrated into the HTU setup returned the transverse and longitudinal position of the laser beam to its ideal positions throughout the system. Optimization of the LPA only required scanning the jet blade (see Fig.6) z-position to fine-tune the down-ramp injection (Sec.1.2.2) for electron beam central energy. After a single scan, and no further manual intervention, production of electron beams of comparable parameters (see Tab.6) to the previous day had been restored and enabled immediate return to FEL studies, within 30 mins of fully amplifying the laser beam.

**Table 6:** Electron beam parameters on back-to-back high power runs, demonstrating turn-key operation of the laser system and LPA source on the HTU beamline. On Day 2, only a singular scan of the longitudinal blade position was conducted to produce the stated performance.

	Day 1	Day 2
Avg Central Energy [MeV]	$100.26 \pm 2.90$	$101.84\pm3.02$
RMS Energy Spread [%]	$5.42 \pm 1.38$	$3.77 \pm 1.33$
Peak Charge Density [pC/MeV]	$6.78 \pm 2.09$	$6.57 \pm 2.60$
Avg Bunch Charge [pC]	$63.98 \pm 20.99$	$51.08 \pm 24.99$

The importance of not only the demonstrated stability, but especially the ability for a quick return to operation (turn-key) can not be overstated. It made a tremendous difference in how much time during high-power operations can effectively be dedicated towards FEL optimization and operation, instead of working with the LPA source to produce the electron beams of desired parameters. The demonstrations of high LPA-driven FEL gain and reliability reported in the following chapters, which represent a significant improvement of the technology, would not have been possible without these discussed improvements in laser system stability and performance.

# 7.4 Demonstration of reliable, high-gain FEL operation

The corresponding publication to the results discussed in this section is

S. K. Barber, **F. Kohrell**, C. Doss., K. Jensen, C. Berger, F. Isono, Z. Eisentraut, S. Schröder, A. J. Gonsalves, K. Nakamura, G. R. Plateau, R. A. van Mourik, M. Gracia-Linares, L. Labun, B. M. Hegelich, S. V. Milton, C. G. R. Geddes, J. Osterhoff, C. B. Schroeder, E. H. Esarey, and J. van Tilborg

Greater than 1000-fold gain in a free-electron laser driven by a laser plasma accelerator with >90% reliability, Phys. Rev. Lett. 135, 055001 (2025)

With the HTU system in the state of reliability and performance described in the previous sections, eleven consecutive high power runs were conducted. During each of them, strong undulator radiation signal was observed for many hours, allowing in-depth studies of the LPA-driven FEL process for over a month. The key results of these first studies will be discussed below.

# 7.4.1 Experimental Conditions

For the experiments presented here, the LPA was optimized to produce electron beams with a central energy of  $100 \pm 2.5 \,\text{MeV}$ ,  $2 \pm 1 \,\%$  rms energy spread, and bunch charge of  $90 \pm 30 \,\text{pC}$ . Due to the high level of laser beam and plasma source stability, enabled by the extensive efforts discussed in Sec.6 and 7.2, more than five hours of operation showed less than one percent drift of the bunch central energy.

The electron beams were subsequently sent through the transport line described in Sec.4.2. Set to produce an  $R_{56}$  value of 150 µm, the magnetic chicane, discussed in detail in Sec.2.2, decompresses the bunch and thus reduces its slice energy spread. This  $R_{56}$  value was determined experimentally to produce the most efficient and reliable FEL lasing. Assuming the ultra-short bunches created by the LPA interaction are compressed, the measured FWHM energy spread of  $\sim 4\%$  would cause the full bunch length to get stretched to approximately

$$l_{e^{-}} = \sqrt{(l_{e^{-},0})^{2} + ((\Delta \gamma/\gamma) \cdot R_{56})^{2}}$$

$$= (\Delta \gamma/\gamma) \cdot R_{56} = 4\% \cdot 150 \,\mu\text{m} = 6 \,\mu\text{m} \qquad \text{(for } l_{e^{-},0} \ll (\Delta \gamma/\gamma) \cdot R_{56})$$

with  $l_{e^-,0}$  the electron bunch length at the source. The investigation of undulator radiation presented in this section was conducted in two different operational configurations of the FEL system. In both cases, the EMQ triplet and steering magnets were used to optimize electron beam focusing, position and angle leading up to the VISA undulator. All other parameters connected to the LPA interaction were kept identical between the two experiments. However, different target functions were chosen for the optimization.

In the first configuration (i), the above mentioned controls over the electron beam trajectory and focus were scanned to maximize undulator signal on each of the first three diagnostic port locations. They are located  $0.25\,\mathrm{m},~0.75\,\mathrm{m},~\mathrm{and}~1.25\,\mathrm{m}$  into the  $4\,\mathrm{m}$  long VISA undulator, respectively.

For the second configuration (ii), the optimization was conducted only on the final diagnostic location after the undulator. The reflective pellicle (P 2 in Fig.7) used at this location transmits the electron bunch while reflecting undulator signal to the optical spectrometer. This allows measurement of the charge transmission (using ICT 1 and 2) and electron beam spectra (on MagSpec 2), while recording undulator radiation signal.

The emittance spoiler (P 1 in Fig.7) was used in both configurations to establish the level of incoherent undulator radiation at each analyzed diagnostic port.

# 7.4.2 Analysis of Gain Length

The results from operating in configuration (i) can be seen in Fig.44(a). The undulator signal was taken with the energy calibrated optical spectrometer moved to the respective diagnostic port location. 600 shots were taken at each location without and 200 shots with the emittance spoiler inserted. When the emittance spoiler was removed, the measured undulator radiation pulse energy (blue) exhibits exponential growth over the first three diagnostic locations, matching expectations for the FEL gain process (Eq.3.7 in Sec.3.2).

In comparison, the signal measured with the spoiler inserted (orange) shows no noticeable increase over the same distance. Despite theoretical expectations of linear scaling, this behavior of the incoherent emission can be explained by the experimental configuration for the collection of undulator signal. With the size of the diagnostic probes being only  $3 \, \text{mm} \times 3 \, \text{mm}$  and the incoherent emission expected to show higher divergence than the coherent signal, on the order of a few mrad, only signal from a few tens of centimeters upstream of the probe can effectively be collected. Because the probes are located 50 cm apart, one would expect to measure about the same signal strength on every port, which essentially matches the observed trend in Fig.44(a).

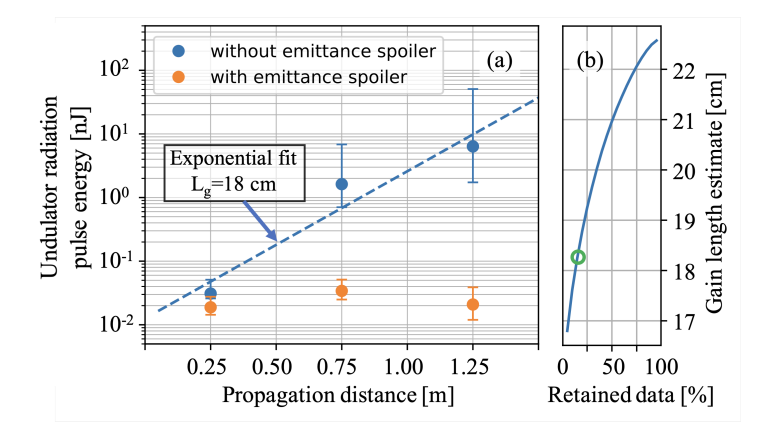


Figure 44: (a): Undulator radiation over propagation distance in the undulator measured in configuration (i). Data taken with the emittance spoiler removed is displayed in blue, with it inserted in orange. (b) The gain length calculated from subsets of the data sorted by measured pulse energy. The green circle at 20% retained data corresponds to the interval matching the data shown in (a) (blue), and the dashed line shows expected exponential scaling for the corresponding gain length.

Detailed analysis of LPA-driven FEL data like this comes with specific inherent challenges, based on the convolution of different sources of FEL signal instability. The two main factors contributing are related to the electron beam parameters (bunch charge, energy, pointing, etc.), and statistical variations in the SASE process (based on shot noise).

As discussed in Sec.6, the LPA process has many potential sources of instability connected to the drive laser, and electron beams generated are prone to relatively high jitter of key

bunch parameters. With the limited amount of diagnostics available, it is extremely difficult to determine if an observed difference in FEL signal for two bunches of identical measured charge is due to jitter of the LPA or SASE process.

To try and account for this issue, an attempt is made of determining a higher and lower boundary for the gain length, matching the experimental data. For this purpose, all shots of FEL signal at a certain diagnostic location were sorted from lowest to highest amount of measured signal. By applying a filter that only includes a certain percentage of the highest energies measured, the impact of LPA and SASE fluctuations on the expected gain length  $L_g$  can then be estimated (discussed more in-depth in Sec.3.2.2, see Eqs.3.7 and 3.8). Fig.44(b) shows the gain length as a function of the part of the retained, energy sorted undulator radiation data. With  $P_0 \stackrel{!}{=} P(z=0)$ , and the interval of  $L_g$  between 16.7 cm and 22.5 cm (extracted from the Fig.44(b)), using Eq.3.7 these values translate to an expected gain over the measured propagation distance of 1.25 m of

$$\begin{split} P(z) &= P_0 \cdot \exp\left(\frac{z}{L_g}\right) \\ \Longrightarrow P_0 \cdot \exp\left(\frac{z}{L_{g,max}}\right) \leq P(1.25\,\mathrm{m}) \leq P_0 \cdot \exp\left(\frac{z}{L_{g,min}}\right) \\ \Longrightarrow 258.7 \cdot P_0 \leq P(1.25\,\mathrm{m}) \leq 1781.2 \cdot P_0 \end{split}$$

The evolution of the highest 20% of FEL signal over the propagation distance in the undulator are represented in Fig.44(a). The mean of the measured signal is shown as blue dots, the error bars represent minimum and maximum signal contained in this subset of the data. The exponential trend corresponding to the gain length expected for the specific retained interval is represented as the blue dashed line. The 20% of the data showing the highest measured FEL signal was chosen empirically due to its clear demonstration of exponential scaling of the un-spoiled signal.

To calculate after which propagation distance through the undulator full FEL saturation would occur, Eq.3.9 can be utilized. Using the undulator radiation pulse energy, as established as the metric for FEL performance in this chapter, instead of the radiation power, the equation can be simplified to

$$\begin{split} E_{sat} &\approx \rho_{\rm FEL} \cdot E_{beam} \\ &= \rho_{\rm FEL} \cdot \frac{\gamma m_e c^2 Q_{beam}}{e} \end{split}$$

with  $Q_{beam}$  the total electron beam charge. Using the electron beam properties discussed in this section and calculating the corresponding Pierce parameter  $\rho_{\rm FEL}$ , this leads to a saturation pulse energy of about  $E_{sat} \approx 9.2 \,\mu \rm J$ . Utilizing Eq.3.7, again equivalent for the undulator radiation energy instead of power, one finds for the distance  $z = z_{sat}$  to reach FEL saturation

$$E_l(z) = E_0 \cdot \exp \frac{z}{L_g}$$

$$\Longrightarrow E_{sat} \approx E_0 \cdot \exp \frac{z_{sat}}{L_g}$$

$$\iff z_{sat} \approx \ln \left(\frac{E_{sat}}{E_0}\right) \cdot L_g$$

Using the values for  $L_g$  and  $E_0$  corresponding to the exponential fit displayed in Fig.44(a), full FEL saturation under the measured conditions would occur after about  $z_{sat} \approx 2.5 \,\mathrm{m}$ , which is well before the end of the 4 m long VISA undulator.

However, after the third diagnostic location the measured signal flattens out substantially. This was attributed to an observed loss of overlap between transverse electron beam and undulator radiation profile. Both can be monitored on the camera imaging the YAG:Ce screens at each port, because the undulator radiation and electron bunch both cause the screen to scintillate. This loss in spatial overlap, showing diverging trajectories of electron beam and undulator radiation, is most likely caused by a misalignment between the 1 m long undulator segments.

# 7.4.3 Statistical Analysis of Electron Bunch and FEL Radiation Parameters

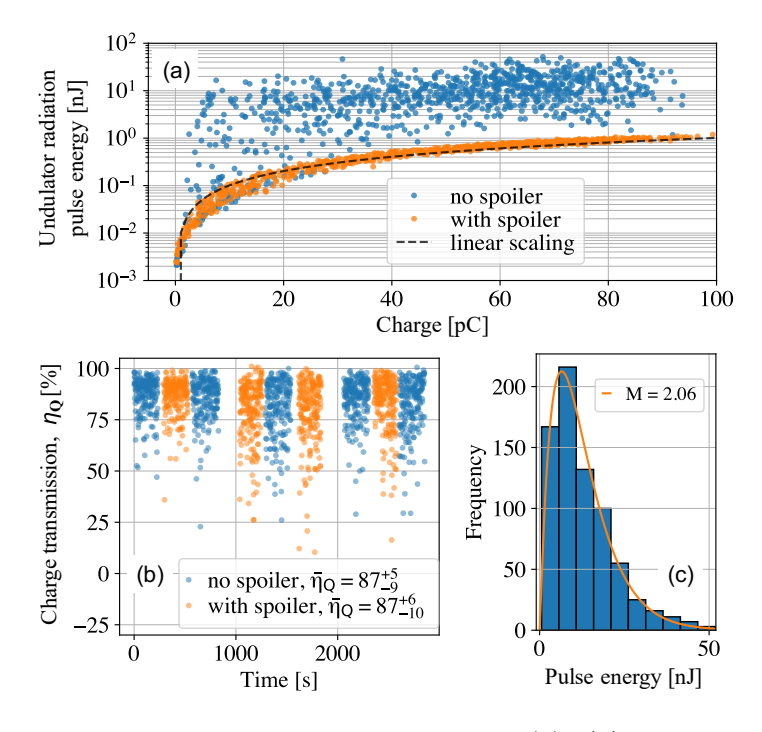


Figure 45: Results of operating the FEL in configuration (ii). (a): Energy calibrated undulator signal as a function of bunch charge, measured after the undulator without (blue) and with the emittance spoiler inserted (orange). The black dashed line represents the expected linear scaling of incoherent undulator radiation. (b): Corresponding charge transmission to (a) measured over operation time. The average charge transmission  $\bar{\eta}_Q$ , displayed with its interquartile range for both cases, shows no significant difference. (c): Histogram of FEL signal pulse energy data shown in (a). A Gamma distribution fit (orange curve) with M=2.06.

The results of operating the system in experimental configuration (ii) are shown in Fig.45. Total undulator signal measured at the final diagnostic port, after the full 4 m length of the VISA undulator, as a function of charge is displayed in Fig.45(a). The displayed data was taken over the course of an hour of operation, during which scans with the emittance spoiler removed (blue) and inserted (orange) were taken in alternating order. Variations in measured bunch charge are a result of LPA instabilities, caused by shot-to-shot variations in the laser and plasma parameters. This is confirmed by quantifying the charge transmission in Fig.45(b), showing an average of 87% charge transmission through the undulator, with no measurable impact of inserting the emittance spoiler.

To quantify the FEL performance, it is helpful to introduce the "coherent enhancement" factor  $F_C$ :

$$F_C = \frac{S_{\text{total}}(q)}{S_{\text{spont}}(q)} \tag{7.1}$$

with  $S_{\text{total}}(q)$  representing the total integrated counts of undulator signal on the optical spectrometer for a given shot of charge q and  $S_{\text{spont}}(q)$  the number of counts of incoherent undulator radiation expected for a beam of charge q. The value  $S_{\text{spont}}(q)$  is calculated based on the linear fit (counts per pC) extracted from the dataset taken using the emittance spoiler.

When comparing the measured undulator signal with the emittance spoiler removed (blue) to the spontaneous emission, as measured when the spoiler is inserted (orange), values of  $F_C$  of up to 1000 can be observed for bunch charge below 20 pC, and about 100 for higher charge values. In addition to these high levels of coherent enhancement, the reliability demonstrated here is unprecedented. Of all of the shots without the emittance spoiler inserted, more than 90% exhibited  $F_C > 2$ , showcasing a never before demonstrated level of performance for LPA-driven FELs.

More specific insight into the FEL dynamics can be gained by investigating the distribution of measured pulse energies. Fundamentally, as discussed in Sec.3.2.2, the SASE FEL process arises from shot noise of the electron bunch. The observed FEL pulse energy varies based on how much of the bunch contributes coherently to the SASE process, which is quantified by the number of coherence lengths, or longitudinal modes, M. Therefor, this factor M is directly connected to the rms fluctuation of FEL pulse energy,  $\sigma_{\text{FEL}} = \frac{1}{\sqrt{M}}$ . The overall probability of observing a certain pulse energy in the exponential gain regime has been shown to follow a Gamma distribution. [99, 100]

To determine the number of coherence lengths contributing to FEL lasing based on the experimental data shown Fig.45(a), the dataset had to be reduced to only include shots exhibiting some level of gain  $(F_C > 1)$ . For this reason, the histogram of measured undulator radiation pulse energies in Fig.45(c) only contains data from the charge interval between 40 and 80 pC.

Fitting a Gamma distribution to the experimental data (orange curve) delivers an rms fluctuation of FEL pulse energy of  $\sigma_{\rm FEL} \approx 0.70$ , which corresponds to  $M \approx 2.04$ . By comparing the length of the bunch contributing to FEL lasing (as predicted by this statistical analysis) to the total length of the bunch (as estimated using the Chicane  $R_{56}$  setpoint), will give an idea how well the statistical results match the experimental reality.

With the gain length  $L_g = 18 \, \mathrm{cm}$ , estimated from the results in the configuration (i) (see Fig.44), undulator period  $\lambda_u = 1.8 \, \mathrm{cm}$  and central wavelength of the undulator radiation at

100 MeV bunch energy of  $\lambda_r = 420$  nm, the value of the coherence length  $L_c$  for the experiments discussed here is  $L_c = \lambda_r \cdot L_g / \lambda_u \approx 4.2 \,\mu\text{m}$ .

These results suggest a bunch length of  $l_{e^-} = M \cdot L_c = 8.6 \,\mu\text{m}$  in comparison to the previous estimate of  $l_{e^-} \ge 6 \,\mu\text{m}$  made in Sec.7.4.1 (based on the assumption of minimum bunch length at the source).

These results can also be expressed analogously in terms of M: the coherence length  $L_c \approx 4.2 \,\mu\text{m}$  (based on the gain length estimated from configuration (i), see Fig.44) suggests  $M = l_{e^-}/L_c \ge 6 \,\mu\text{m}/4.2 \,\mu\text{m} = 1.43$ , whereas the statistical distribution of FEL pulse energies recorded in configuration (ii) (Fig.45) predict  $M \approx 2.04$ .

Given that these two values are derived from experiments conducted on different days and under different experimental conditions, they agree reasonably well. The changed electron beam trajectory in configuration (ii) could affect the gain length, causing different coherence lengths  $L_c$  between the two experiments. Another possible explanation for the difference in electron bunch parameters, calculated based on the two different experimental configurations, could be that the electron bunch is not actually fully compressed at the source. Assuming this already stretched bunch is not ideally up-chirped (higher energies located in the tail of the bunch), this would lead to the chicane further stretching it and therefor lead to the final bunch length being larger than 6  $\mu$ m (only for up-chirped bunches a magnetic chicane acts as a compressor, see Sec.2.2).

Despite the slight differences, the results from configuration (i) and (ii) are in agreement about the beam quality being high enough to enable full FEL saturation over the 4 m of the VISA undulator. However, just as mentioned in the discussion of configuration (i), significant FEL lasing was only observed over a distance of roughly a meter upstream from the final diagnostic location, where the signal had been optimized in configuration (ii). The observation of gain exceeding 1000 over 1 m of propagation, as well as the analysis of M, confirm again this to be most likely related to systematic issues of the undulator alignment. Being unable to sustain the observed level of exponential gain over more than  $\sim 1$  m, either at the front or back of the 4 m undulator, strongly suggests this to be the culprit.

This theory is further supported by observations made during all of the following experiments conducted over the last year. Exponential increase of measured undulator signal with propagation distance was only ever achievable either in the first or second half of the undulator. Theoretical calculations confirm that misalignment of just one section by less than one millimeter can prevent sustained high gain over the full length of the undulator. To reach full FEL saturation, extensive efforts to characterize and and correct the undulator segments alignment will most likely be necessary.

# 7.5 Stable, long-term operation of an LPA-driven FEL

After the many successful consecutive high power runs leading to the results documented in the previous section, a dedicated campaign was planned to test how long the FEL can be operated with the current level of stability of the HTU LPA source. Especially due to the challenges of reaching saturation, despite a demonstrated electron bunch quality with corresponding gain length that should enable saturating the FEL emission over the 4 m of VISA undulator (discussed in Sec.7.4.3), this seemed a valuable demonstration before focusing on solving the suspected undulator alignment issue.

The FEL data presented in this section was gathered during a single day of LPA-driven FEL operation, employing all the active stabilization techniques discussed in Sec.6 and demonstrating full-day ( $> 8\,\mathrm{hrs}$ ) operation of an LPA-driven FEL on the HTU system. The corresponding publication to the results discussed in this section is

**F. Kohrell**, S. K. Barber, C. Doss., K. Jensen, C. Berger, S. Schröder, Z. Eisentraut, K. Nakamura, A. J. Gonsalves, F. Isono, G. R. Plateau, R. A. van Mourik, M. Gracia-Linares, L. Labun, B. M. Hegelich, S. V. Milton, C. G. R. Geddes, J. Osterhoff, E. H. Esarey, C. B. Schroeder, F. Grüner and J. van Tilborg,

Over 8 hours of continuous operation of a free-electron laser driven by a laser-plasma accelerator, Phys. Rev. Accel. Beams - in review

# 7.5.1 Experimental Configuration

Fig.46(a) gives a schematic overview of the entire electron beamline from the LPA source to the VISA undulator, as configured during the experiment discussed in this section. The LPA target is operated using the down-ramp injection technique (discussed in Sec.1.2.2), by supplying helium gas at 200 psi (1.38 MPa) to the gas jet and blade assembly. The electron source was tuned to generate electron beams of 100 MeV central energy and high stability over more than ten hours of continuous accelerator operation, as can be seen in Fig.46(b).

During this campaign, the magnetic chicane, discussed in-depth in Sec.2.2, was set to generate an  $R_{56}$  of 150  $\mu$ m. This value was determined experimentally to deliver the best FEL performance, by scanning the  $R_{56}$  while monitoring the FEL signal on the optical spectrometer for a defined, optimized electron beam trajectory through the VISA undulator.

After the LPA source and magnetic chicane had been optimized, the electron beams were analyzed on the magnetic spectrometer (MagSpec 1 in Fig.46(a)) before being sent to the VISA undulator, exhibiting 105 MeV average central energy, 5% central energy jitter and about  $(5 \pm 1)\%$  energy spread. After more than ten hours without operator input, the measured electron beams average central energy was measured to be 102 MeV with 7% jitter, and  $(5\pm 2)\%$  energy spread. The corresponding electron beam spectra of 100 consecutive shots taken before and after the measurement of FEL performance can be seen in Fig.46(b). The most noticeable decrease in electron beam performance over more than ten hours of LPA operation was the average electron bunch charge, reduced from about  $(80\pm30)$ pC to  $(50\pm25)$ pC.

For a full day of continuous operation, these results represent an unparalleled level of LPA

stability on the HTU system, critical to enable the following long-term FEL studies. This level of reliability was only made possible through the extensive efforts to improve the long-term stability of key LPA parameters discussed in Sec.6, and the improvements to the laser beam quality resulting in turn-key LPA operation (discussed in Sec.7.2).

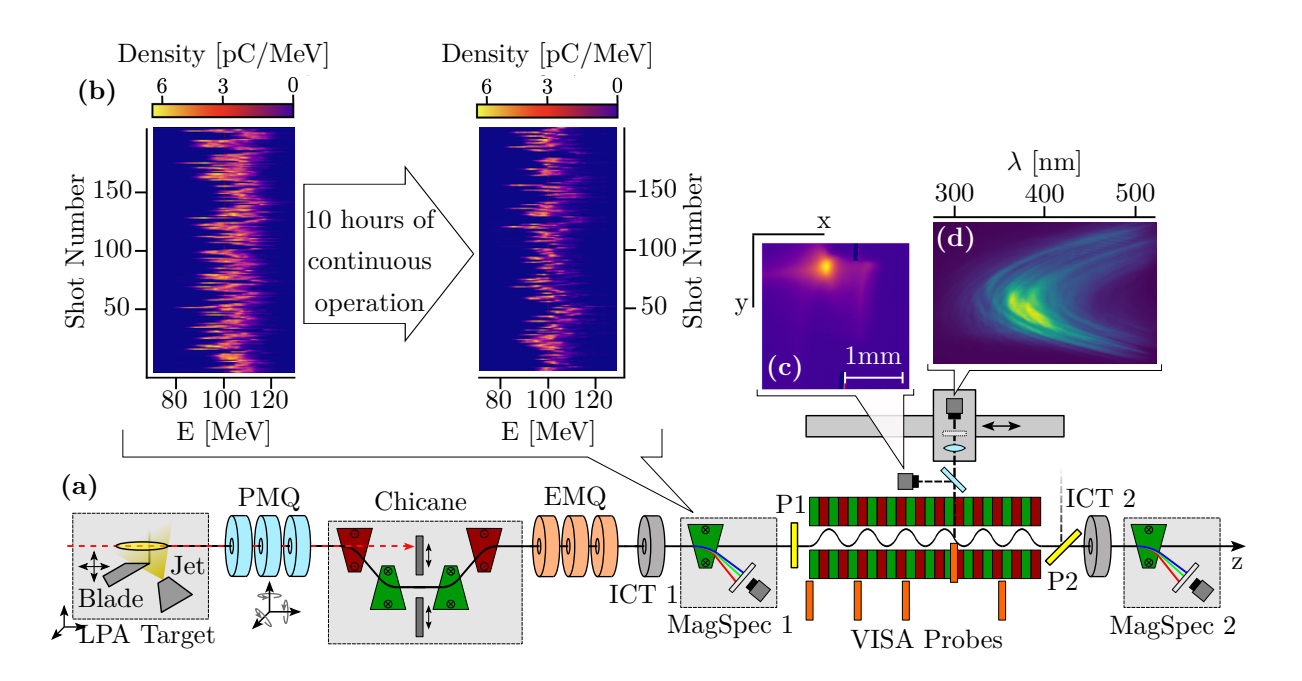


Figure 46: (a): Schematic of the LPA source, and the subsequent electron beamline to the VISA undulator, including diagnostics. The laser pulse (red dashed line, see Sec.4.1) is focused onto the density down-ramp target (Sec.4.2), and the generated electron beam (black solid line) is collimated, longitudinally stretched, and focused before being sent into the undulator (Sec.4.3). (b): 100 consecutive electron beam spectra recorded with the magnetic spectrometer upstream of the undulator (MagSpec 1). The two scans were taken ten hours apart, during which period no changes were made to the laser or plasma target. (c): Example of a transverse electron beam profile, recorded by inserting one of eight probes spaced evenly along the length of the undulator. A dichroic mirror separates the emission from the YAG:Ce screen to an imaging camera. (d): Representative example spectrum of a high gain shot recorded in this dataset. The FEL radiation is transmitted through the dichroic mirror onto an energy calibrated optical spectrometer, and the parabolic shape matches the expected trend due to angular dependence of the coherence condition (see Sec.3.2.1 and Eq.3.3).

# 7.5.2 Results of Long-term Stability Campaign

Because the thin reflective pellicle at the end of the undulator (P2 in Fig.46(a)) enables recording the reflected undulator radiation and transmitted electron beam spectrum at the same time, this location was chosen to monitor the FEL performance in this experiment. It allowed gaining the largest amount of on-shot information during this demonstration of full-day FEL operation. Using a subset of controls including the EMQ triplet and the steering magnets controlling the launch trajectory into the undulator, the undulator radiation signal on the optical spectrometer (as can be seen in Fig.46(d)) was maximized. No further manipulations of the drive laser, plasma target and electron beamline were conducted for the following  $> 8\,\mathrm{hrs}$  of LPA-driven

FEL operation.

Note that the single shot displayed in Fig.46(d) has a slightly asymmetric intensity distribution in the vertical axis. This is not representative of the average recorded undulator radiation spectra, but instead the artifact of a slightly varying angle of the electron beam trajectory with respect to the magnetic axis of the undulator. This shot was chose for display purposes only based on its particularly strong total signal intensity.

Following this optimization, the emittance spoiler pellicle at the undulator entrance (P1 in Fig.46(a)) was inserted and 200 consecutive shots recorded on the optical spectrometer. This reference scan established the linear scaling between incoherent undulator radiation and electron bunch charge, displayed as the black dashed line in Fig.47, and discussed extensively in Sec.5.3.2 and Sec.7.4. This incoherent emission scaling is a crucial tool to quantify the FEL performance. By identifying the shots which show undulator radiation pulse energy values exceeding the linear trend, one finds the shots which exhibit coherent enhancement or FEL lasing (the different scaling of incoherent and coherent undulator emission is discussed in detail in Sec.3.2). The level of coherent over incoherent emission can be quantified through the the "coherent enhancement factor"  $F_C$  introduced previously in Sec.7.4.3. It is defined as the ratio between measured FEL signal and the level of incoherent emission at a certain charge value, see Eq.7.1.

The FEL stability data presented in this section was taken at a repetition rate of 1 Hz and in batches of 200 consecutive shots. Due to small breaks between the scans, dictated by automated post-analysis of the last acquired dataset and control system procedures, about 2000 shots per hour were taken on average.

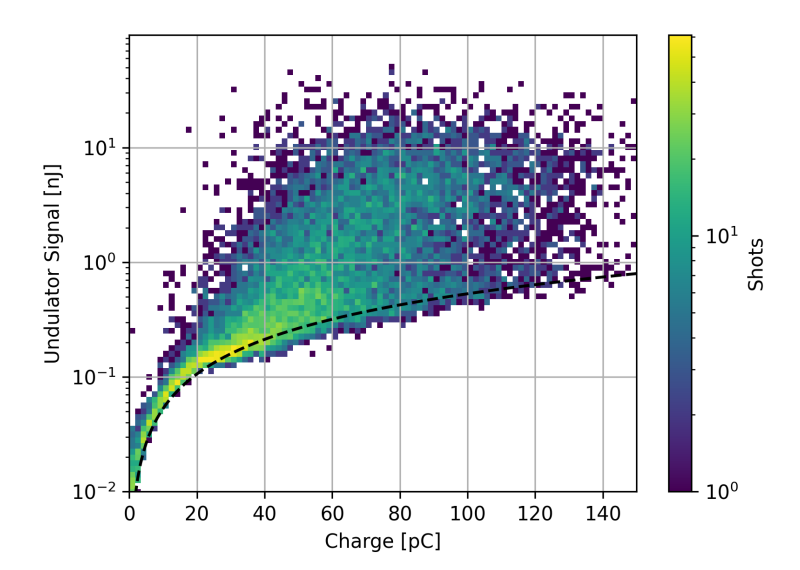


Figure 47: Histogram of the integrated undulator radiation signal for all shots taken over the > 8 hrs of continuous operation, plotted against electron bunch charge. The color shows the number of shots contained in each binned pixel, the black dashed curve represents the experimentally determined scaling of incoherent undulator radiation.

After three hours of uninterrupted FEL operation, the eight probes along the undulator were inserted consecutively to record the electron beam trajectory through the undulator, but no changes were made to the LPA parameters or electron beam steering and focusing. This roughly

one hour interruption was followed by another five hours of monitoring the undulator pulse energy at the VISA exit location (P2).

Analyzing all shots taken on the energy calibrated optical spectrometer enables assessing the performance of the LPA and FEL over the whole duration of the experiment. A plot of undulator radiation signal in nJ versus electron bunch charge, recorded on the ICT after the undulator exit (ICT 2 in Fig.46), can be seen in Fig.47. Of the roughly fifteen thousand shots taken on the spectrometer, 92% show some level of coherent enhancement ( $F_C > 1$ ), and over half of all recorded shots yielded  $F_C > 2$ . When directly comparing the measured undulator radiation signal to the incoherent emission scaling (black dashed line) in Fig.47,  $F_C$  values exceeding 100 can be observed for charge vales below 60 pC, with much more data points in range of  $20 < F_C < 50$ . These results are not far from the level of performance demonstrated in the previous work by Barber et al. [72], which were discussed in Sec.7.4, and displayed in Fig.45(a). However, during the initial demonstration in Sec.7.4, this FEL performance was only sustained for an hour or two without optimization by the operators, whereas the results displayed above in Fig.47 were sustained for an entire day ( $> 8 \, \mathrm{hrs}$ ) of operation.

This data provides the first demonstration of continuous and reliable LPA-driven FEL operation on the many-hour timescale.

Despite the observed general stability and performance, a noticeable drop in average undulator radiation signal over the first three hours of operation ( $\sim 6000$  shots) was observed during the course of the experiment, see Fig.48. After the circa hour long interruption to measure the electron beam trajectory along the full length of the undulator, the undulator emission seemed to have stabilized at a lower signal level than at the beginning of the day. This previously mentioned break in static operation, during which no changes were made to the LPA source or electron beam transport, is represented in Fig.48 by the vertical split in the plot. Over the following roughly five hours of operation the undulator signal appears to remain largely unchanged, showing no further systematic decrease. To quantify this change in FEL performance throughout the measurement period, the average of the coherent enhancement factor  $F_C$  was calculated. During the first thousand shots (roughly 30 mins) after optimization of the LPA source and electron beam trajectory, the average observed coherent enhancement was  $\bar{F}_{C,1} = 9.0$ . The last one thousand shots of the day, after 7.5 hrs of continuous operation, still exhibited an average coherent enhancement of  $\bar{F}_{C,2} = 4.2$ .

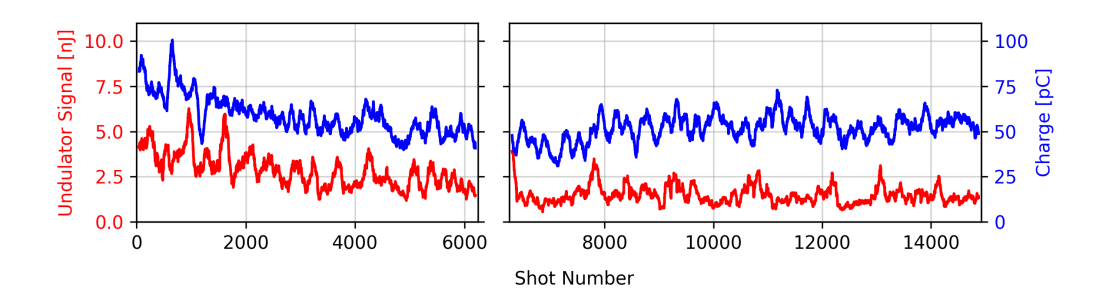


Figure 48: Measured undulator radiation pulse energy (red) and electron bunch charge (blue) over roughly eight hours of continuous operation, displayed as a rolling average over 100 consecutive data points. The gap after 6000 shots represents about a roughly one hour break, during which the electron beam trajectory through the VISA undulator was measured.

Similar to the undulator signal, a reduction in the average bunch charge over time was observed,

as can be seen by the blue curve in Fig.48 and the spectra displayed in Fig.46(b). Directly comparing the trend of average bunch charge to the undulator signal immediately reveals a strong correlation. The charge exhibits a similar, noticeable decrease over the first three hours, or 6000 shots, of operation. From an average of  $\sim 80\,\mathrm{pC}$  to  $\sim 50\,\mathrm{pC}$ , this drop in LPA performance represents the most likely explanation for the observed reduction in undulator signal and average coherent enhancement. However, given the set of active stabilization systems reducing long-term drift of laser parameters crucial to the LPA process, the exact reason for the observed decrease in electron bunch charge is unclear. One parameter of the laser pulse currently not actively stabilized against long-term drift is the laser angle incident on the gas target. A noticeable drift in laser angle, despite fixed transverse and longitudinal position of the laser focus, would be expected to significantly impact the trajectory of the electron beam from the LPA source, as confirmed experimentally on the HTU system by Berger et al. in Ref.[97]. Without continuous adjustments to the electron beam transport system to compensate for this effect, it would affect the alignment of the beam to the undulator axis, reducing the FEL performance and in turn observed signal over time.

Despite the observed reduction in FEL signal, quantified by the averaged coherent enhancement decreasing by about 53% over eight hours of operation, the level of performance and stability of both the LPA source and FEL signal shown in this chapter still represent a higher than previously shown reliability and a crucial step towards a proof-of-concept demonstration of a viable LPA-driven light source at 420 nm. Ultimately, this goal requires to also reach stable, full FEL saturation in the SASE regime. As discussed in detail in Sec.7.4.2, electron bunches at 100 MeV with the charge, energy spread and emittance which can be reproduced reliably on the HTU system, should be able to achieve full FEL saturation in less than the 4 m of the VISA undulator. However, as described in Sec.7.4, sustaining exponential gain over more than about 1.5 m in the undulator remains elusive. To gain the necessary in-depth information about the correlations between observed coherent enhancement and the electron beam and transport parameters, extensive further studies of the LPA-driven FEL will be essential.

Having shown that the HTU system can be used as a reliable platform for FEL gain studies over multi-hour timescales, and has the capability to monitor crucial laser, plasma, electron beam, and FEL radiation parameters on every shot, gives us a unique ability to investigate potential correlations and push towards the realization of reaching FEL saturation.

#### 7.5.3 Study of Parameter Correlations

After gathering about 15k shots of LPA-FEL data, including a wide variety of on-shot diagnostics (discussed in Sec.4 and 5), the goal was to identify the recorded parameters showing the strongest correlation to the FEL signal and gain deeper insight into the dynamics of the HTU system.

For this purpose, the correlation of each of the over one hundred parameters recorded on every shot against the log of integrated undulator signal was calculated. Twelve parameters with a noticeable correlation were identified and isolated for further analysis, and are displayed in Tab.7. The strongest correlations, exceeding  $|\rho|=0.5$ , are all directly connected to electron bunch properties. They include the charge measured up- and down-stream of the undulator with the respective ICTs (see Fig.46), which can be seen in Fig.47 to be naturally correlated to the undulator signal. Furthermore, the electron beam energy after the undulator (measured on every shot using MagSpec 2, see Fig.46) shows similar correlations, and separating the spectra

into individually analyzed regions-of-interest (RoI) even allows to gain insight into which bunch energy distributions correlate to higher measured undulator pulse energies. The laser and plasma properties showed lower correlation factors,  $|\rho| < 0.2$ . Impactful parameters include the laser pulse duration and spectrum (extracted from *GRENOUILLE* images temporal and spectral D2 $\sigma$ ), as well as pulse energy (measured non-invasively after the multi-pass amplifier, see E in Fig.5), and the centroid of the laser beam measured on the ghost line. The angle of the density shock (formed by the blade above the gas jet) with respect to the laser beam, difference in density between the shock and plasma column ( $\Delta n$ ), and gradient (slope) of the density shock were the plasma parameters included in the further analysis.

Electron Bunch		Laser and Plasma	
Parameter	ho	Parameter	ho
Charge (ICT 1)	0.69	Laser Energy (E)	0.09
Charge (ICT 2)	0.79	$D2\sigma_{\mathrm{temp}}$	0.10
Energy (total RoI)	0.76	$D2\sigma_{ m spectr}$	0.15
Energy (low E RoI)	0.68	Shock Density $(\Delta n)$	0.19
Energy (high E RoI)	0.58	Plasma Shock Angle	0.11
		Shock Slope	0.11
		Laser Beam Centroid	0.02

**Table 7:** Measured parameters of the electron bunch, as well as laser pulse and plasma target, and their correlations  $\rho$  to the log of the total measured undulator radiation pulse energy.

The amount of parameters identified that show a noticeable correlation to the undulator radiation signal is an indication of the high capability of the HTU system diagnostics to give valuable insights into the connections between the LPA and FEL process. To showcase some particularly interesting parameters, their correlation to the log of the total undulator radiation pulse energy is plotted in Fig.49.

The correlations of temporal and spectral second moments of the laser pulse, extracted from the raw GRENOUILLE images and discussed in detail in Sec.5.2, are shown in Fig.49(a) and (b), respectively. Of the two only the temporal second moment, strongly correlated to the laser pulse duration (see Fig.29(a)), is actively stabilized. This could explain the lower correlation factor  $\rho$  for  $D2\sigma_{temp}$  of 0.1, compared to the  $\rho = 0.15$  for  $D2\sigma_{spectr}$ . This result motivates further investigations of potential instabilities of the laser pulse spectrum, and another potential avenue to further stabilize the LPA interaction.

Fig.49(c) displays the noticeable correlation between the undulator signal and plasma density difference  $\Delta n$  between the shock feature and plasma column. There is about a 20% variation of this parameter during the experiment, affecting the measured level of undulator signal. Again, this reveals a previously unknown connection between an LPA parameter and the FEL performance, and will inform further studies and potential attempts at stabilization.

The final parameter displayed, as can be seen in Fig.49(d), is the counts measured on the magnetic spectrometer after the VISA undulator (MagSpec 2 in Fig.46). Specifically, the high-energy region-of-interest (RoI) defined based on the averaged electron beam spectra. As can be seen in Tab.7, the counts measured in the low-energy RoI for the same shots display a high correlation factor of  $\rho = 0.68$ . This distinction between different regions of the electron beam

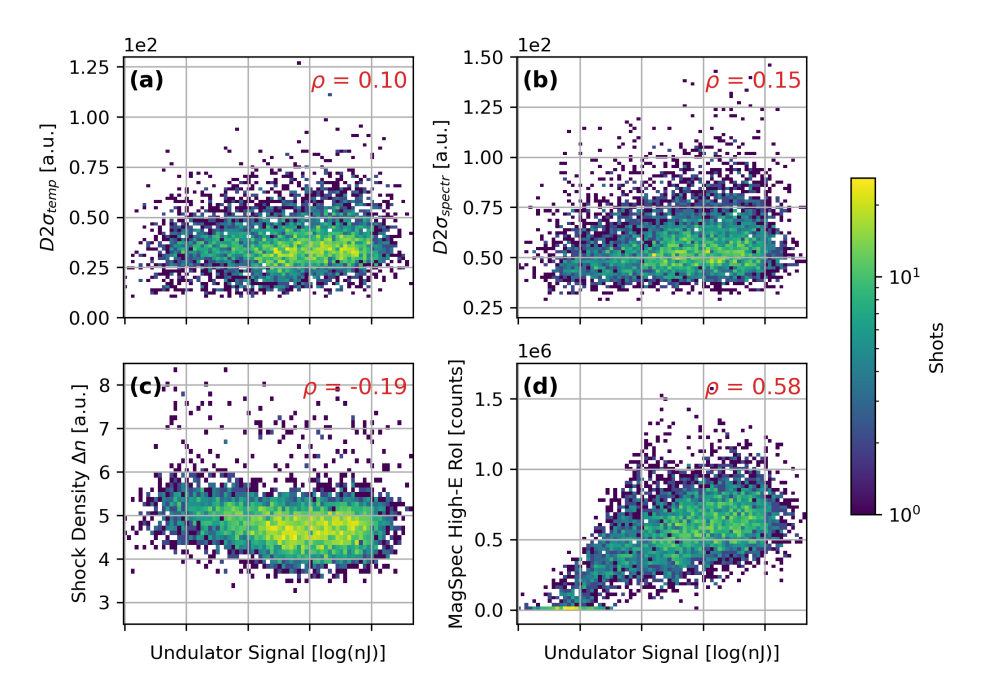


Figure 49: Histogram of correlations for four selected LPA parameters and the undulator radiation signal, and their respective  $\rho$  values: (a) the temporal, (b) the spectral second moment  $D2\sigma$  extracted from the raw GRENOUILLE images, (c) the plasma density difference  $\Delta n$  between the shock and plasma column, and (d) the counts captured on the high energy RoI of the magnetic spectrometer MagSpec 2 (Fig.46).

spectra contributing differently to the undulator signal has not been observed previously on the HTU system and will be investigated further in follow-up campaign.

To investigate if the LPA parameters add any information about the FEL performance not already contained in the electron beam parameters, a dedicated study was conducted. A simple predictive model was developed, based on the least squares method and the electron bunch and LPA parameters introduced above. The goal was to show if an improvement in correlation to the measured FEL signal can be achieved this way, exceeding the highest value exhibited by any individual parameter ( $\rho = 0.79$  for the electron beam charge after the undulator).

By choosing the log of the FEL signal as the dependent variable y and the twelve parameters mentioned above as the dependent variables  $x_j$ , the residual function r for a shot  $i \in N$  (N total number of shots) is defined as

$$r_i = y_i - f(x_{j,i}, \beta_j) \tag{7.2}$$

with  $\beta_j$  the parameters of the predictive function f. For the purpose of simplicity, f was chosen as a linear equation including all parameters  $x_j$ :

$$f = x_{1,i} \cdot \beta_{1,i} + x_{2,i} \cdot \beta_{2,i} + \cdots + x_{12,i} \cdot \beta_{12,i}$$

$$(7.3)$$

This scheme represents the simplest way to model how the experimental parameters could affect the dependent variable. Optimizing now to minimize the target function

$$S = \sum_{i=1}^{N} r_i^2 \tag{7.4}$$

delivers a function f with factors  $\beta_j$ , determining the relative impact of each recorded experimental parameter on the observed FEL signal. By providing the measured values for the experimental parameters  $x_j$  for a certain shot, f can be used to calculate the predicted value for the FEL signal  $y_{pred}$  (dependent variable). Comparing  $y_{pred}$  to the actually measured value of the FEL signal, as can be seen in Fig.50, allows to quantify the quality of the models predictive capability.

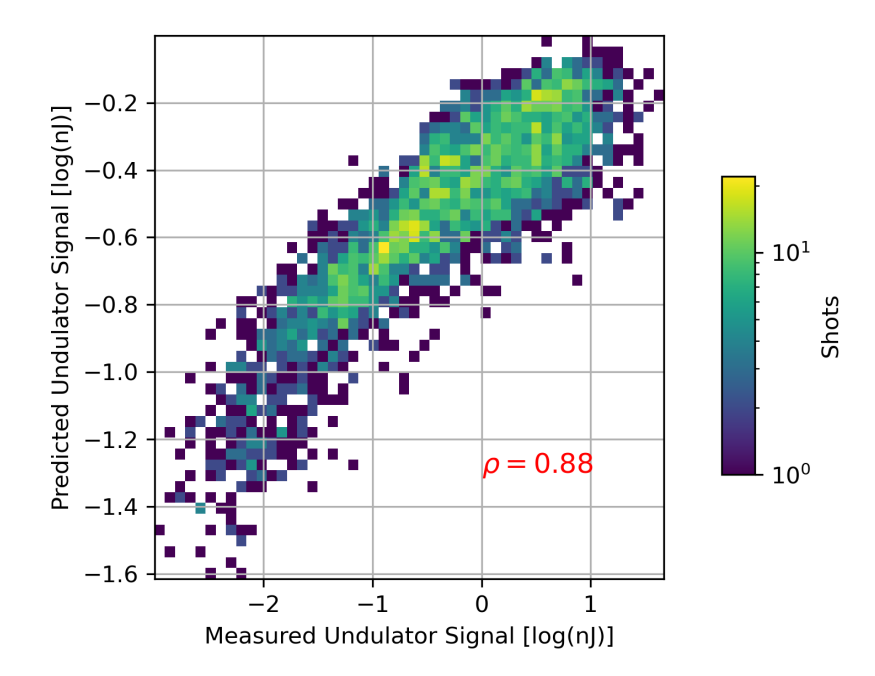


Figure 50: Histogram plot to compare the correlation between log of measured and predicted undulator radiation signal. The twelve experimental parameters identified to have the strongest correlation to the FEL signal were combined to calculate a predictive function f from half of the shots taken during the long-term dataset presented in this work, using the least squares method. The function f was then applied to the second half of the data to calculate the "predicted" undulator signal. The color represents the number of shots included in each binned pixel.

All shots taken during the experiment were randomly divided into two sets. One half was used to "train" the model and determine f, which was in turn applied to the second half of data points. By determining the correlation between the log of the total measured and predicted FEL signal, the effectiveness of the model can be assessed. Adjusting the intervals of values included in the analysis for each parameter (setting boundaries for the parameter space based on reasonable assumptions) allowed further optimization the accuracy of the prediction.

The correlation between the log of predicted and measured FEL signal achieved this way is  $\rho = 0.88$ , as can be seen in Fig.50, which provides a significant improvement over any of the individual experimental parameters correlation to the FEL signal. By including laser and plasma parameters in addition to electron beam data, a more accurate description of the FEL performance on the HTU system has been demonstrated.

Furthermore, the model was to be specifically tested by quantifying how well it can predict if a certain shot will exhibit coherent FEL emission. The ratio between shots with a predicted coherent enhancement factor  $F_{C,pred} > 1$  that actually showed a measured  $F_{C,meas} > 1$  exceeds 90%.

The impressive level of predictive capability demonstrated by such a simplistic model confirms the value of the broad range of on-shot diagnostics on the HTU system. It suggests that more complex modeling techniques will be able to give meaningful new insights and benefit the goal of further increasing FEL performance and reliability.

However, the correlation is not perfect and the model struggles with predicting the level of coherent enhancement accurately. The mean predicted value of  $\bar{F}_{C,pred}=2.6$  is less than half of the mean measured value  $\bar{F}_{C,meas}=5.8$ , which is also represented by the range of the FEL signal values displayed in Fig.50. The fact that the least squares model can predict with high accuracy that a shot will lase, but not the exact level of coherent enhancement, is not too surprising. The statistics of FEL pulse energy, as described in Sec.7.4.3, are heavily impacted by non-deterministic noise of the electron charge distribution, or shot noise, which can not be measured by our diagnostics and included into the model. Previous investigations on the HTU system, discussed by Barber et al. in Ref.[72] and in this work in Sec.7.4, have shown the impact of shot noise on FEL performance to follow the expected trend, and the predicted bunch statistics to match experimental parameters.

## 8 Summary

When I started my PhD project three years ago, work on the HTU system was mainly focused on improving diagnostic and stabilization capabilities for all parameters affecting the LPA interaction, and high power operation was mainly dedicated towards optimizing electron bunch quality. Therefore, Sec.5 focuses on key improvements and additions to the diagnostics suite on the HTU beamline which were implemented during my thesis work.

As a part of this greater effort I upgraded the cameras in the magnetic spectrometers (see Sec.5.1), which led to the incorporation of new hardware with a degree of compatibility with the experimental control system, and a demonstrated increase in sensitivity by about 44%. An extensive effort was made to cross-calibrate the new setup to maintain the precise charge calibration conducted at the ALS by Nakamura et al. [83].

The most substantial diagnostic project I worked on during my thesis work was the design, setup and characterization of an on-shot, non-invasive laser pulse duration diagnostic, documented in Sec.5.2. This setup allowed gaining insight into temporal and spectral dynamics of the laser during high power operations, and immediately demonstrated its meaningful impact by revealing systematic instabilities of the pulse duration that triggered a detailed investigation and effort to stabilize them.

To enhance the capability of undulator diagnostics, I installed and calibrated a UV enhanced optical spectrometer on the 4m translation stage located parallel to the VISA undulator, see Sec.5.3.1. This diagnostic has been used since for the measurement of undulator radiation energy during all the demonstrations of high gain and high reliability of our LPA-driven FEL setup.

The addition of a thin pellicle in front of the undulator discussed in Sec.5.3.2, to spoil the electron beam emittance, has proven to be an invaluable tool to distinguish between coherent and incoherent undulator emission, and quantify the FEL performance by determining the level of coherent enhancement.

Having discussed additions to the diagnostics of the HTU system, Section 6 focuses on the implementation of stabilization systems to improve the robustness and reliability of the LPA interaction.

Through in-depth studies of the laser pulse energy and duration stability under varying conditions in Secs.6.1, 6.2, and 6.3, I traced the observed effects to the multi-pass amplifier and connected them to drift of the beam centroid on the amplifier crystals. The installation of a commercial beam stabilization system allowed me to effectively eliminate drift of the transverse beam position centroid, and thereby stabilize the laser pulse duration as well as energy.

Combined with further efforts by the HTU team, especially to reduce drift of the longitudinal laser focal position, discussed in Sec.6.4 and by Jensen et al. in Ref.[101], these improvements to the stability of key LPA parameters proved crucial to enable the generation of stable electron beams on the many-hour timescale. This paved the way for the following demonstrations of whole-day accelerator and long-term FEL operation.

After improving the diagnostic capabilities and stability of the LPA, Section 7 describes the dedicated effort to achieve reliable LPA-driven FEL operation on the HTU system.

To eliminate time-consuming alignment of the laser system on every day of high power operation, and the associated re-optimization of the LPA target, Sec. 7.2 describes the dedicated

#### 8 Summary

attempt made to enable "turn-key" operation of the high-power laser system and LPA. This goal was successfully achieved through the implementation of active stabilization systems, improved operational procedures, and extensive maintenance of hardware components of the laser system, leading to a demonstrated reduction of time between laser start-up and FEL operation to less than two hours.

The above summarized work on the HTU system during my PhD project has culminated in the production of electron beams with a reliability enabling full-day, stable accelerator operation. This level of source stability is critical for the time-consuming and ultra-precise alignment and matching of the electron beam to the undulator, necessary to achieve high gain through the SASE FEL process.

In Sec.7.4 I describe the demonstrated achievement of sustaining exponential FEL gain over  $\sim 1.25\,\mathrm{m}$  in the VISA undulator, leading to final observed gain levels exceeding 1000. Furthermore, over 90% of the recorded shots exhibited a coherent enhancement of > 2, an unprecedented level of reliability and major improvement of overall performance of LPA-driven FELs.

Sec.7.5 documents the results of a dedicated campaign to show true long-term stability of an LPA-driven FEL, which I successfully demonstrated as a part of my PhD work. Showing highly stable electron beam generation over more than ten hours and FEL operation of more than eight hours without intervention by the operators, these results represent an important step towards achieving full FEL saturation using an LPA source.

A simple model I trained on a subset of the experimental results presented here delivered a high degree (> 90%) of accuracy when predicting if a shot will display coherent FEL emission, based solely on laser, plasma, and electron beam parameters monitored during the experiment. This result serves as another powerful indication of the capabilities of the HTU system as a capable platform for long-term, LPA-driven FEL studies, and the potential to improve the FEL performance based on the existing diagnostic capabilities.

Over the three years of my PhD research on the BELLA Center's HTU system, many milestones have been achieved, including the first demonstration of high-gain LPA-driven FEL operation by Barber et al. [72], and the most recent long-term stability results by Kohrell et al. [98]. Especially the drastic progress on the HTU system development has opened the door for a variety of exciting future projects, making use of the stable, high-quality LPA electron beams.

Also, the recent demonstrations of LPA-generated electron beams exceeding 10 GeV by Picksley et al. [12] opens the possibility of LPA-driven FELs reaching the hard x-ray regime.

## 9 Outlook

The significant improvements made to the stability and performance of the LPA source, as well as the achieved demonstrations of high-gain and reliability of the LPA-driven FEL enabled by it, have paved the way for exciting follow-up campaigns and further progress towards advancing LPA-based light source technology.

Encouraged by the success of demonstrating predictive capabilities, the HTU team plans to deploy more sophisticated modeling techniques in the future to study the complex connections between LPA parameters, the experimental setup, undulator alignment, and the FEL performance more in-depth.

Despite the significant improvements of LPA-driven FEL performance shown in this work, the results of the discussed experiments seem to suggest that further, major studies of electron beam transport to and through the undulator will be required to reach full FEL saturation. We have shown in Sec.7.4 that the quality of electron bunches, which can be reliably generated by the LPA source, should saturate the FEL in noticeably less than the 4 m available in the VISA undulator. But exponential gain could not be sustained for more than about 1.5 m, despite excessive efforts made to increase it. The most recent achievements in long-term LPA-driven FEL operation, and the corresponding ability for in-depth studies of parameter correlations, are giving rise to hope that future electron beam transport, matching, and trajectory studies will reveal important clues as to how to fulfill the potential of saturating the FEL at 420 nm. This would provide another crucial milestone in the effort of establishing LPA-driven FELs as a more compact alternative light source technology.

Ultimately, the goal should be to demonstrate the capabilities of such a light source to reach a wavelength range useful for scientific or industrial applications ( $\lambda_l < 30 \,\mathrm{nm}$ ). The setup and stabilization techniques presented in this thesis are fundamentally capable of delivering stable electron beams at energies up to 500 MeV, which would enable reducing the undulator radiation wavelength to below  $\lambda_l = 20 \, \mathrm{nm}$  (Eq.3.2). However, because the gain length  $L_g$  scales effectively linearly with the electron energy (see Eq. 3.6 and 3.8 in Sec. 3.2), even just increasing the electron energy to  $> 300 \,\mathrm{MeV}$ , which would reduce  $\lambda_l$  to about  $50 \,\mathrm{nm}$ , would render reaching FEL saturation over the 4 m of the VISA undulator impossible, unless order-of-magnitude improvements to electron beam quality could be achieved. For this reason, the HTU system does not aim to serve as a sub 20 nm light source user facility, and instead as a platform for further research and development of LPA-driven light source technology in the future. We have demonstrated its capability of pushing the boundaries of reliable LPA source operation, by advancing the diagnostic capabilities and improving stability of the driving laser system, as well as the ability to use it as a powerful platform for studying the correlations between LPA-parameters and the FEL process. Enabling proof-of-concept results including full saturation at 420 nm, and demonstrating some level of FEL gain at undulator radiation wavelengths approaching sub 50 nm will be the long-term goals for this experiment, while steadily improving LPA-generated electron beam quality and stability, as well as studying transport, shaping, and matching of these beams to the VISA undulator.

## **Acknowledgment**

I would like to thank the following people for their contributions to the work presented (and everything which is not included) in this thesis.

- Sam Barber, without whom non of the results discussed here would have been possible. For his mentorship and guidance, for the always fun and engaging work and time I got to spend under his leadership on the HTU system.
- Curtis Berger, for sharing the joy and the burden of being a PhD student with me. For many great hours of wine tasting, motorcycle riding, and eating good food. For his friendship.
- Sarah Schröder, for valuable scientific input and teaching me how to sail. For many evenings of cooking together and drinking wine, for inspiring me by being the most dedicated and hard-working scientist I have ever met, and an amazing friend.
- Bob Ettelbrick, for sharing his wealth of knowledge on lasers and optics. For the professional and personal discussions while wrenching on our BMWs, shooting pool and late night Harley Davidson rides to get milkshakes at *Denny's*.
- **Axel Huebl**, for general advice on writing papers and a doctoral thesis, scientific careers, life, motorcycles, and countless fun and helpful discussions over burgers at *In-N-Out*.
- Hao Ding, for his advice and assistance in designing the chirped-mirror compressor for
  the pulse duration diagnostic setup, as well as many insightful and extensive discussions
  of experimental results. For giving me confidence when I needed it the most.
- Kyle Jensen and Chris Doss, for their support in the lab and office, especially with all things related to trying to wrap my head around python, github and the HTU control system infrastructure.
- Robert Jacob, for sharing his prototype of the dispersion correction system for the non-invasive, on-shot pulse duration diagnostic, and his insights. They greatly helped during the process of designing and setting up the diagnostic beamline on the HTU system.
- Carl Schroeder, for always having time for me and my questions and concerns. For spending many hours reading and correcting my work, giving helpful feedback and advice, and cheering me up.
- Jeroen van Tilborg, for the many helpful discussions about FROG and beam stabilization, for his insights and advice and giving me the opportunity to work with the great team at BELLA and the HTU system.
- Florian Grüner, for taking me on as a doctoral candidate and making it possible for me to conduct my research with the BELLA team at LBNL. For his support and encouragement, always taking the time to give me feedback and advice on my progress.
- Wolfgang Hillert and Günter Sigl, for agreeing to be a part of the examination committee.

All the plots in this thesis were generated using the *Matplotlib* library for *Python. ChatGPT4-o* was used only to help write some of the code for data analysis and plotting. The schematic displays of scientific principles and the experimental setups were designed in *Inkscape*.

## **List of Acronyms**

ALS	Advanced Light Source	LFS	Longitudinal Focal Stabilization
BELLA	Berkeley Lab Laser Accelerator	LPA	Laser-Plasma Accelerator
CCD	Charge-Coupled Device	NIR	Near Infrared
CMOS	Complementary Metal-Oxide Semiconductor	OAP	Off-Axis Parabola
CMP	Chirped-Mirror Compressor	PA	Paraxial Approximation
CPA	Chirped-Pulse Amplification	$\mathbf{PC}$	Pockels Cell
DESY	Deutsches Elektronen Synchrotron	PID	Proportional-Integral- Derivative
DM	Deformable Mirror	PMQ	Permanent Magnet Quadrupole
$\mathbf{EMQ}$	Electromagnetic Quadrupole	PSD	Position Sensitive Detector
Eu-XFEL	European XFEL	$\mathbf{RF}$	Radio Frequency
FEL	Free-Electron Laser	${ m rms}$	Root Mean Square
FODO	Focusing-Drift-Defocusing- Drift	RoC	Radius of Curvature
FROG	Frequency-Resolved Optical Gating	SASE	Self-Amplified Spontaneous Emission
FWHM	Full Width at Half Maximum	SAT	Spectral Amplitude Threshold
GDD	Group Delay Dispersion	SHG	Second Harmonic Generation
GRENOUILLE	Grating Eliminated No- nonsense Observation of Ultrafast Incident Laser Light E-fields	SLAC	Stanford Linear Accelerator
HR	High Reflective	$\mathbf{U}\mathbf{V}$	Ultraviolet
HTT	Hundred Terawatt Thomson	VISA	Visible to Infrared SASE Amplifier
HTU	Hundred Terawatt Undulator	VIS	Visible Spectrum
HVAC	Heating, Ventilation, and Air Conditioning	WFS	Wavefront Sensor
ICT	Integrating Current Transformer	XFEL	X-ray FEL
LBNL	Lawrence Berkeley National Laboratory	XUV	Extreme Ultraviolet
LCLS	Linac Coherent Light Source	YAG	Yttrium Aluminum Garnet

- <sup>1</sup>W. C. Röntgen, "Ueber eine neue Art von Strahlen", en, Annalen der Physik **300**, \_eprint: https://onlinelibrary.wiley.com/doi/pdf/10.1002/andp.18983000103, 12–17 (1898).
- <sup>2</sup>E. O. Lawrence and M. S. Livingston, "The Production of High Speed Light Ions Without the Use of High Voltages", Physical Review **40**, Publisher: American Physical Society, 19–35 (1932).
- <sup>3</sup>E. F. Haussecker and A. W. Chao, "The Influence of Accelerator Science on Physics Research", en, Physics in Perspective **13**, 146–160 (2011).
- <sup>4</sup>A. D. Cahill, J. B. Rosenzweig, V. A. Dolgashev, S. G. Tantawi, and S. Weathersby, "High gradient experiments with \$X\$-band cryogenic copper accelerating cavities", Physical Review Accelerators and Beams 21, Publisher: American Physical Society, 102002 (2018).
- <sup>5</sup>T. Tajima and J. M. Dawson, "Laser Electron Accelerator", Physical Review Letters **43**, Publisher: American Physical Society, 267–270 (1979).
- <sup>6</sup>O. Lundh, J. Lim, C. Rechatin, L. Ammoura, A. Ben-Ismaïl, X. Davoine, G. Gallot, J.-P. Goddet, E. Lefebvre, V. Malka, and J. Faure, "Few femtosecond, few kiloampere electron bunch produced by a laser-plasma accelerator", Nat. Physics 7, 219–222 (2011).
- <sup>7</sup>J. P. Couperus, R. Pausch, A. Köhler, O. Zarini, J. M. Krämer, M. Garten, A. Huebl, R. Gebhardt, U. Helbig, S. Bock, K. Zeil, A. Debus, M. Bussmann, U. Schramm, and A. Irman, "Demonstration of a beam loaded nanocoulomb-class laser wakefield accelerator", Nat. Commun. 8, 487 (2017).
- <sup>8</sup>R. Weingartner, S. Raith, A. Popp, S. Chou, J. Wenz, K. Khrennikov, M. Heigoldt, A. R. Maier, N. Kajumba, M. Fuchs, B. Zeitler, F. Krausz, S. Karsch, and F. Grüner, "Ultralow emittance electron beams from a laser-wakefield accelerator", Phys. Rev. ST Accel. Beams 15, 111302 (2012).
- <sup>9</sup>L. T. Ke, K. Feng, W. T. Wang, Z. Y. Qin, C. H. Yu, Y. Wu, Y. Chen, R. Qi, Z. J. Zhang, Y. Xu, X. J. Yang, Y. X. Leng, J. S. Liu, R. X. Li, and Z. Z. Xu, "Near-gev electron beams at a few per-mille level from a laser wakefield accelerator via density-tailored plasma", Phys. Rev. Lett. 126, 214801 (2021).
- <sup>10</sup>A. R. Maier, N. M. Delbos, T. Eichner, L. Hübner, S. Jalas, L. Jeppe, S. W. Jolly, M. Kirchen, V. Leroux, P. Messner, M. Schnepp, M. Trunk, P. A. Walker, C. Werle, and P. Winkler, "Decoding Sources of Energy Variability in a Laser-Plasma Accelerator", en, Physical Review X 10, 031039 (2020).
- <sup>11</sup>A. J. Gonsalves, K. Nakamura, J. Daniels, C. Benedetti, C. Pieronek, T. C. H. de Raadt, S. Steinke, J. H. Bin, S. S. Bulanov, J. van Tilborg, C. G. R. Geddes, C. B. Schroeder, C. Tóth, E. Esarey, K. Swanson, L. Fan-Chiang, G. Bagdasarov, N. Bobrova, V. Gasilov, G. Korn, P. Sasorov, and W. P. Leemans, "Petawatt laser guiding and electron beam acceleration to 8 gev in a laser-heated capillary discharge waveguide", Phys. Rev. Lett. 122, 084801 (2019).
- <sup>12</sup>A. Picksley, J. Stackhouse, C. Benedetti, K. Nakamura, H. E. Tsai, R. Li, B. Miao, J. E. Shrock, E. Rockafellow, H. M. Milchberg, C. B. Schroeder, J. van Tilborg, E. Esarey, C. G. R. Geddes, and A. J. Gonsalves, "Matched guiding and controlled injection in dark-current-free, 10-gev-class, channel-guided laser-plasma accelerators", Phys. Rev. Lett. 133, 255001 (2024).

- <sup>13</sup>C. B. Schroeder, W. M. Fawley, E. Esarey, and W. P. Leemans, "Design of an XUV FEL driven by the laser-plasma accelerator at the LBNL LOASIS facility", in 28th International Free Electron Laser Conference (FEL 2006) (Aug. 2006), pp. 455–458.
- <sup>14</sup>F. Grüner, S. Becker, U. Schramm, T. Eichner, M. Fuchs, R. Weingartner, D. Habs, J. Meyer-ter-Vehn, M. Geissler, M. Ferrario, L. Serafini, B. van der Geer, H. Backe, W. Lauth, and S. Reiche, "Design considerations for table-top, laser-based VUV and X-ray free electron lasers", en, Applied Physics B 86, 431–435 (2007).
- <sup>15</sup>M. Fuchs, R. Weingartner, A. Popp, Z. Major, S. Becker, J. Osterhoff, I. Cortrie, B. Zeitler, R. Hörlein, G. D. Tsakiris, U. Schramm, T. P. Rowlands-Rees, S. M. Hooker, D. Habs, F. Krausz, S. Karsch, and F. Grüner, "Laser-driven soft-X-ray undulator source", en, Nature Physics 5, Publisher: Nature Publishing Group, 826–829 (2009).
- <sup>16</sup>W. Wang, K. Feng, L. Ke, C. Yu, Y. Xu, R. Qi, Y. Chen, Z. Qin, Z. Zhang, M. Fang, J. Liu, K. Jiang, H. Wang, C. Wang, X. Yang, F. Wu, Y. Leng, J. Liu, R. Li, and Z. Xu, "Free-electron lasing at 27 nanometres based on a laser wakefield accelerator", en, Nature 595, Number: 7868 Publisher: Nature Publishing Group, 516–520 (2021).
- <sup>17</sup>M. Labat, J. C. Cabada, A. Ghaith, A. Irman, A. Berlioux, P. Berteaud, F. Blache, S. Bock, F. Bouvet, F. Briquez, Y.-Y. Chang, S. Corde, A. Debus, C. D. Oliveira, J.-P. Duval, Y. Dietrich, M. E. Ajjouri, C. Eisenmann, J. Gautier, R. Gebhardt, S. Grams, U. Helbig, C. Herbeaux, N. Hubert, C. Kitegi, O. Kononenko, M. Kuntzsch, M. LaBerge, S. Lê, B. Leluan, A. Loulergue, V. Malka, F. Marteau, M. H. N. Guyen, D. Oumbarek-Espinos, R. Pausch, D. Pereira, T. Püschel, J.-P. Ricaud, P. Rommeluere, E. Roussel, P. Rousseau, S. Schöbel, M. Sebdaoui, K. Steiniger, K. Tavakoli, C. Thaury, P. Ufer, M. Valléau, M. Vandenberghe, J. Vétéran, U. Schramm, and M.-E. Couprie, "Seeded free-electron laser driven by a compact laser plasma accelerator", Nat. Photonics 17, 150–156 (2023).
- <sup>18</sup>E. Esarey, C. B. Schroeder, and W. P. Leemans, "Physics of laser-driven plasma-based electron accelerators", Reviews of Modern Physics 81, Publisher: American Physical Society, 1229–1285 (2009).
- <sup>19</sup>K. K. Swanson, H.-E. Tsai, S. K. Barber, R. Lehe, H.-S. Mao, S. Steinke, J. van Tilborg, K. Nakamura, C. G. R. Geddes, C. B. Schroeder, E. Esarey, and W. P. Leemans, "Control of tunable, monoenergetic laser-plasma-accelerated electron beams using a shock-induced density downramp injector", Physical Review Accelerators and Beams 20, Publisher: American Physical Society, 051301 (2017).
- <sup>20</sup>S. Bulanov, N. Naumova, F. Pegoraro, and J. Sakai, "Particle injection into the wave acceleration phase due to nonlinear wake wave breaking", Phys. Rev. E 58, R5257–R5260 (1998).
- <sup>21</sup>H. Suk, N. Barov, J. B. Rosenzweig, and E. Esarey, "Plasma electron trapping and acceleration in a plasma wake field using a density transition", Phys. Rev. Lett. **86**, 1011–1014 (2001).
- <sup>22</sup>C. G. R. Geddes, K. Nakamura, G. R. Plateau, C. Toth, E. Cormier-Michel, E. Esarey, C. B. Schroeder, J. R. Cary, and W. P. Leemans, "Plasma-density-gradient injection of low absolute-momentum-spread electron bunches", Phys. Rev. Lett. 100, 215004 (2008).
- <sup>23</sup>F. Massimo, A. F. Lifschitz, C. Thaury, and V. Malka, "Numerical study of laser energy effects on density transition injection in laser wakefield acceleration", en, Plasma Physics and Controlled Fusion 60, Publisher: IOP Publishing, 034005 (2018).

- <sup>24</sup>C. S. Hue, Y. Wan, E. Y. Levine, and V. Malka, "Control of electron beam current, charge, and energy spread using density downramp injection in laser wakefield accelerators", Matter and Radiation at Extremes 8, 024401 (2023).
- <sup>25</sup>F. Kohrell, S. Barber, K. Jensen, C. Berger, C. Schroeder, E. Esarey, and J. van Tilborg, "Optimizing Down-Ramp Injection to Generate Stable and Tunable Electron Bunches for an LPA Driven FEL", in 2022 IEEE Advanced Accelerator Concepts Workshop (AAC) (Nov. 2022), pp. 1–4.
- <sup>26</sup>F. Träger, Springer Handbook of Lasers and Optics, 2nd ed. (Springer Berlin, Heidelberg, 2012).
- <sup>27</sup>P. G. Kryukov, "Ultrashort-pulse lasers", en, Quantum Electronics 31, Publisher: IOP Publishing, 95 (2001).
- <sup>28</sup>D. Strickland and G. Mourou, "Compression of amplified chirped optical pulses", Optics Communications 55, 447–449 (1985).
- <sup>29</sup>C. V. Shank, "Generation of ultrashort optical pulses", in *Ultrashort Laser Pulses: Generation and Applications*, edited by W. Kaiser, Topics in Applied Physics (Springer, Berlin, Heidelberg, 1993), pp. 5–34.
- <sup>30</sup>W. Zhang, H. Teng, Z. Wang, Z. Shen, and Z. Wei, "Efficient amplification of a femtosecond Ti:sapphire laser with a ring regenerative amplifier", Applied Optics 52, Publisher: Optical Society of America, 1517–1522 (2013).
- <sup>31</sup>J. Körner, "Laser Engineering, Chapter 4: Seed Sources", Lecture Script, 2019.
- <sup>32</sup>C. Inc., ed., Vitara Modelocked Ti:S Laser Operator's Manual, Sept. 2011.
- <sup>33</sup>C. Inc., Legend Elite Operator's Manual, Jan. 2013.
- <sup>34</sup>K. Gopal, D. N. Gupta, and H. Suk, "Pulse-length Effect on Laser Wakefield Acceleration of Electrons by Skewed Laser Pulses", IEEE Transactions on Plasma Science 49, 1152–1158 (2021).
- <sup>35</sup>A. Permogorov, G. Cantono, D. Guenot, A. Persson, and C.-G. Wahlström, "Effects of pulse chirp on laser-driven proton acceleration", Scientific Reports 12, 3031 (2022).
- <sup>36</sup>M. Sedaghat, A. Amouye Foumani, and A. R. Niknam, "Controlling the characteristics of injected and accelerated electron bunch in corrugated plasma channel by temporally asymmetric laser pulses", en, Scientific Reports 12, Publisher: Nature Publishing Group, 8115 (2022).
- <sup>37</sup>R. Trebino, Frequency-Resolved Optical Gating: The Measurement of Ultrashort Laser Pulses (Springer US, Boston, MA, 2000).
- <sup>38</sup>R. Trebino, K. W. DeLong, D. N. Fittinghoff, J. N. Sweetser, M. A. Krumbügel, B. A. Richman, and D. J. Kane, "Measuring ultrashort laser pulses in the time-frequency domain using frequency-resolved optical gating", Review of Scientific Instruments 68, 3277–3295 (1997).
- <sup>39</sup>S. Akturk, M. Kimmel, P. OShea, and R. Trebino, "Measuring spatial chirp in ultrashort pulses using single-shot Frequency-Resolved Optical Gating", Optics Express 11, Publisher: Optica Publishing Group, 68–78 (2003).
- <sup>40</sup>K. W. DeLong, R. Trebino, J. Hunter, and W. E. White, "Frequency-resolved optical gating with the use of second-harmonic generation", JOSA B 11, Publisher: Optica Publishing Group, 2206–2215 (1994).

- <sup>41</sup>J. B. Rosenzweig, Fundamentals of Beam Physics (Oxford University Press, Oxford, New York, Nov. 2003).
- <sup>42</sup>S. Humphries, *Charged Particle Beams* (John Wiley and Sons, 2002).
- <sup>43</sup>B. Hidding, G. Pretzler, J. B. Rosenzweig, T. Königstein, D. Schiller, and D. L. Bruhwiler, "Ultracold electron bunch generation via plasma photocathode emission and acceleration in a beam-driven plasma blowout", Phys. Rev. Lett. 108, 035001 (2012).
- <sup>44</sup>L.-L. Yu, E. Esarey, C. B. Schroeder, J.-L. Vay, C. Benedetti, C. G. R. Geddes, M. Chen, and W. P. Leemans, "Two-color laser-ionization injection", Phys. Rev. Lett. **112**, 125001 (2014).
- <sup>45</sup>X. Xu, F. Li, F. S. Tsung, K. Miller, V. Yakimenko, M. J. Hogan, C. Joshi, and W. B. Mori, "Generation of ultrahigh-brightness pre-bunched beams from a plasma cathode for x-ray free-electron lasers", Nature Communications 13, 3364 (2022).
- <sup>46</sup>F. J. Grüner, C. B. Schroeder, A. R. Maier, S. Becker, and J. M. Mikhailova, "Space-charge effects in ultrahigh current electron bunches generated by laser-plasma accelerators", Physical Review Special Topics Accelerators and Beams 12, Publisher: American Physical Society, 020701 (2009).
- <sup>47</sup> Parameters | Linac Coherent Light Source.
- <sup>48</sup>P. Schmüser, M. Dohlus, J. Rossbach, and C. Behrens, Free-Electron Lasers in the Ultraviolet and X-Ray Regime: Physical Principles, Experimental Results, Technical Realization, en, Vol. 258, Springer Tracts in Modern Physics (Springer International Publishing, Cham, 2014).
- <sup>49</sup>R. Ischebeck, "Transverse coherence of a VUV free electron laser", eng, PhD thesis (Deutsches Elektronen-Synchrotron, DESY, Hamburg, 2003).
- <sup>50</sup>N. Majernik, S. K. Barber, J. van Tilborg, J. B. Rosenzweig, and W. P. Leemans, "Optimization of low aspect ratio, iron dominated dipole magnets", Phys. Rev. Accel. Beams 22, 032401 (2019).
- <sup>51</sup>C. Pellegrini, A. Marinelli, and S. Reiche, "The physics of x-ray free-electron lasers", Reviews of Modern Physics 88, Publisher: American Physical Society, 015006 (2016).
- <sup>52</sup>C. Bostedt, S. Boutet, D. M. Fritz, Z. Huang, H. J. Lee, H. T. Lemke, A. Robert, W. F. Schlotter, J. J. Turner, and G. J. Williams, "Linac Coherent Light Source: The first five years", Reviews of Modern Physics 88, Publisher: American Physical Society, 015007 (2016).
- <sup>53</sup>K. W. T. b. J. McFall, The Physics of Particle Accelerators: An Introduction (Oxford University Press, Oxford, New York, May 2001).
- <sup>54</sup>T. H. Maiman, "Stimulated Optical Radiation in Ruby", en, Nature 187, Publisher: Nature Publishing Group, 493–494 (1960).
- <sup>55</sup>A. Mitchel and M. Zemansky, "Chapter III: Absorption lines and measurements of the lifetime of the resonance state", in *Resonance Radiation and Excited Atoms* (Cambridge University Press, Cambridge, 1961).
- <sup>56</sup>J. M. J. Madey, "Stimulated Emission of Bremsstrahlung in a Periodic Magnetic Field", Journal of Applied Physics 42, 1906–1913 (1971).
- <sup>57</sup>A. M. Kondratenko and E. L. Saldin, "Generating Of Coherent Radiation By A Relativistic Electron beam In An ondulator", Part. Accel. 10, 207–216 (1980).

- <sup>58</sup>S. V. Milton, E. Gluskin, N. D. Arnold, C. Benson, W. Berg, S. G. Biedron, M. Borland, Y.-C. Chae, R. J. Dejus, P. K. Den Hartog, B. Deriy, M. Erdmann, Y. I. Eidelman, M. W. Hahne, Z. Huang, K.-J. Kim, J. W. Lewellen, Y. Li, A. H. Lumpkin, O. Makarov, E. R. Moog, A. Nassiri, V. Sajaev, R. Soliday, B. J. Tieman, E. M. Trakhtenberg, G. Travish, I. B. Vasserman, N. A. Vinokurov, X. J. Wang, G. Wiemerslage, and B. X. Yang, "Exponential Gain and Saturation of a Self-Amplified Spontaneous Emission Free-Electron Laser", Science 292, Publisher: American Association for the Advancement of Science, 2037–2041 (2001).
- <sup>59</sup>V. Ayvazyan, N. Baboi, I. Bohnet, R. Brinkmann, M. Castellano, P. Castro, L. Catani, S. Choroba, A. Cianchi, M. Dohlus, H. T. Edwards, B. Faatz, A. A. Fateev, J. Feldhaus, K. Flöttmann, A. Gamp, T. Garvey, H. Genz, C. Gerth, V. Gretchko, B. Grigoryan, U. Hahn, C. Hessler, K. Honkavaara, M. Hüning, R. Ischebeck, M. Jablonka, T. Kamps, M. Körfer, M. Krassilnikov, J. Krzywinski, M. Liepe, A. Liero, T. Limberg, H. Loos, M. Luong, C. Magne, J. Menzel, P. Michelato, M. Minty, U.-C. Müller, D. Nölle, A. Novokhatski, C. Pagani, F. Peters, J. Pflüger, P. Piot, L. Plucinski, K. Rehlich, I. Reyzl, A. Richter, J. Rossbach, E. L. Saldin, W. Sandner, H. Schlarb, G. Schmidt, P. Schmüser, J. R. Schneider, E. A. Schneidmiller, H.-J. Schreiber, S. Schreiber, D. Sertore, S. Setzer, S. Simrock, R. Sobierajski, B. Sonntag, B. Steeg, F. Stephan, K. P. Sytchev, K. Tiedtke, M. Tonutti, R. Treusch, D. Trines, D. Türke, V. Verzilov, R. Wanzenberg, T. Weiland, H. Weise, M. Wendt, I. Will, S. Wolff, K. Wittenburg, M. V. Yurkov, and K. Zapfe, "Generation of GW Radiation Pulses from a VUV Free-Electron Laser Operating in the Femtosecond Regime", Physical Review Letters 88, Publisher: American Physical Society, 104802 (2002).
- <sup>60</sup>A. Murokh, R. Agustsson, M. Babzien, I. Ben-Zvi, L. Bertolini, K. van Bibber, R. Carr, M. Cornacchia, P. Frigola, J. Hill, E. Johnson, L. Klaisner, G. Le Sage, M. Libkind, R. Malone, H.-D. Nuhn, C. Pellegrini, S. Reiche, G. Rakowsky, J. Rosenzweig, R. Ruland, J. Skaritka, A. Toor, A. Tremaine, X. Wang, and V. Yakimenko, "Properties of the ultrashort gain length, self-amplified spontaneous emission free-electron laser in the linear regime and saturation", Physical Review E 67, Publisher: American Physical Society, 066501 (2003).
- <sup>61</sup>C. Pellegrini, "A 4 to 0.1-nm FEL based on the SLAC Linac", Conf. Proc. C **920224**, 364–375 (1992).
- <sup>62</sup>P. Emma, R. Akre, J. Arthur, R. Bionta, C. Bostedt, J. Bozek, A. Brachmann, P. Bucksbaum, R. Coffee, F.-J. Decker, Y. Ding, D. Dowell, S. Edstrom, A. Fisher, J. Frisch, S. Gilevich, J. Hastings, G. Hays, P. Hering, Z. Huang, R. Iverson, H. Loos, M. Messerschmidt, A. Miahnahri, S. Moeller, H.-D. Nuhn, G. Pile, D. Ratner, J. Rzepiela, D. Schultz, T. Smith, P. Stefan, H. Tompkins, J. Turner, J. Welch, W. White, J. Wu, G. Yocky, and J. Galayda, "First lasing and operation of an ångstrom-wavelength free-electron laser", en, Nature Photonics 4, Publisher: Nature Publishing Group, 641–647 (2010).
- <sup>63</sup>R. B. Palmer, "Interaction of Relativistic Particles and Free Electromagnetic Waves in the Presence of a Static Helical Magnet", Journal of Applied Physics 43, 3014–3023 (1972).
- <sup>64</sup>R. Bonifacio, C. Pellegrini, and L. M. Narducci, "Collective instabilities and high-gain regime in a free electron laser", Optics Communications 50, 373–378 (1984).
- <sup>65</sup>K.-J. Kim, "Three-Dimensional Analysis of Coherent Amplification and Self-Amplified Spontaneous Emission in Free-Electron Lasers", Physical Review Letters 57, Publisher: American Physical Society, 1871–1874 (1986).

- <sup>66</sup>J.-M. Wang and L.-H. Yu, "A transient analysis of a bunched beam free electron laser", Nuclear Instruments and Methods in Physics Research Section A: Accelerators, Spectrometers, Detectors and Associated Equipment 250, 484–489 (1986).
- $^{67}Https://www.coherent.com/.$
- <sup>68</sup> Https://tem-messtechnik.de/en/.
- $^{69}Https://www.thalesgroup.com/en.$
- $^{70}$  Https://www.mrc-systems.de/en/products/laser-beam-stabilization.
- <sup>71</sup>F. Isono, J. v. Tilborg, S. K. Barber, J. Natal, C. Berger, H.-E. Tsai, T. Ostermayr, A. Gonsalves, C. Geddes, and E. Esarey, "High-power non-perturbative laser delivery diagnostics at the final focus of 100-TW-class laser pulses", en, High Power Laser Science and Engineering 9, e25 (2021).
- <sup>72</sup>S. K. Barber, F. Kohrell, C. Doss, K. Jensen, C. Berger, F. Isono, Z. Eisentraut, S. Schröder, A. J. Gonsalves, K. Nakamura, G. R. Plateau, R. A. van Mourik, M. Gracia-Linares, L. Labun, B. M. Hegelich, S. V. Milton, C. G. R. Geddes, J. Osterhoff, C. B. Schroeder, E. Esarey, and J. van Tilborg, "Greater than 1000-fold gain in a free-electron laser driven by a laser-plasma accelerator with high reliability", en, Physical Review Letters 135, 10.1103/vh62-gz1p (2025).
- <sup>73</sup>M. Migliorati, A. Bacci, C. Benedetti, E. Chiadroni, M. Ferrario, A. Mostacci, L. Palumbo, A. R. Rossi, L. Serafini, and P. Antici, "Intrinsic normalized emittance growth in laser-driven electron accelerators", Physical Review Special Topics Accelerators and Beams 16, Publisher: American Physical Society, 011302 (2013).
- <sup>74</sup>A. R. Maier, A. Meseck, S. Reiche, C. B. Schroeder, T. Seggebrock, and F. Grüner, "Demonstration Scheme for a Laser-Plasma-Driven Free-Electron Laser", Physical Review X 2, Publisher: American Physical Society, 031019 (2012).
- <sup>75</sup>R. Carr, M. Cornacchia, P. Emma, H.-D. Nuhn, B. Poling, R. Ruland, E. Johnson, G. Rakowsky, J. Skaritka, S. Lidia, P. Duffy, M. Libkind, P. Frigola, A. Murokh, C. Pellegrini, J. Rosenzweig, and A. Tremaine, "Visible-infrared self-amplified spontaneous emission amplifier free electron laser undulator", Physical Review Special Topics Accelerators and Beams 4, Publisher: American Physical Society, 122402 (2001).
- <sup>76</sup>A. Tremaine, X. J. Wang, M. Babzien, I. Ben-Zvi, M. Cornacchia, H.-D. Nuhn, R. Malone, A. Murokh, C. Pellegrini, S. Reiche, J. Rosenzweig, and V. Yakimenko, "Experimental characterization of nonlinear harmonic radiation from a visible self-amplified spontaneous emission free-electron laser at saturation", Phys. Rev. Lett. 88, 204801 (2002).
- <sup>77</sup>H.-D. Nuhn, FEL Trajectory Analysis for the VISA Experiment, tech. rep. SLAC-PUB-7913, 9912 (Oct. 1998), SLAC-PUB-7913, 9912.
- <sup>78</sup>P. Frigola, A. Murokh, P. Musumeci, C. Pellegrini, S. Reiche, J. Rosenzweig, A. Tremaine, M. Babzien, I. Ben-Zvi, E. Johnson, R. Malone, G. Rakowsky, J. Skaritka, X. J. Wang, K. A. Van Bibber, L. Bertolini, J. M. Hill, G. P. Le Sage, M. Libkind, A. Toor, R. Carr, M. Cornacchia, L. Klaisner, H. .-. Nuhn, R. Ruland, and D. C. Nguyen, "Initial gain measurements of an 800 ă nm SASE FEL, VISA", Nuclear Instruments and Methods in Physics Research Section A: Accelerators, Spectrometers, Detectors and Associated Equipment, FEL2000: Proc. 22nd Int. Free Electron Laser Conference and 7th F EL Users Workshop 475, 339–342 (2001).

- <sup>79</sup>R. Trebino, P. OShea, M. Kimmel, and X. Gu, "Very Simple FROG Apparatus: GRENOUILLE", in *Frequency-Resolved Optical Gating: The Measurement of Ultrashort Laser Pulses*, edited by R. Trebino (Springer US, Boston, MA, 2000), pp. 229–236.
- $^{80} Https://www.swampoptics.com/.$
- $^{81}$  Https://www.kodak.com/en/.
- 82 Https://www.baslerweb.com/en-us/shop/aca720-290gm/.
- <sup>83</sup>K. Nakamura, A. J. Gonsalves, C. Lin, A. Smith, D. Rodgers, R. Donahue, W. Byrne, and W. P. Leemans, "Electron beam charge diagnostics for laser plasma accelerators", Physical Review Special Topics Accelerators and Beams 14, Publisher: American Physical Society, 062801 (2011).
- <sup>84</sup>I. H. Malitson, "Interspecimen Comparison of the Refractive Index of Fused Silica\*,", EN, JOSA 55, Publisher: Optica Publishing Group, 1205–1209 (1965).
- <sup>85</sup>I. Walmsley, L. Waxer, and C. Dorrer, "The role of dispersion in ultrafast optics", en, Review of Scientific Instruments 72, 1–29 (2001).
- <sup>86</sup>A. Guggenmos, Https://www.ultrafast-innovations.com/optics/HD2012.html, en, Collection, Publisher: Alexander Guggenmos, May 2021.
- <sup>87</sup>H. Moseley and D. Allan, "Intensity of the flash associated with laser-induced plasma in the eye", en, Physics in Medicine & Biology 32, 1159 (1987).
- <sup>88</sup>M. R. Edwards, N. J. Fisch, and J. M. Mikhailova, "Laser-driven plasma sources of intense, ultrafast, and coherent radiation", Physics of Plasmas 28, 013105 (2021).
- <sup>89</sup>K. Nakamura, H.-S. Mao, A. J. Gonsalves, H. Vincenti, D. E. Mittelberger, J. Daniels, A. Magana, C. Toth, and W. P. Leemans, "Diagnostics, Control and Performance Parameters for the BELLA High Repetition Rate Petawatt Class Laser", IEEE Journal of Quantum Electronics 53, Conference Name: IEEE Journal of Quantum Electronics, 1–21 (2017).
- <sup>90</sup>S. Backus, C. G. Durfee III, M. M. Murnane, and H. C. Kapteyn, "High power ultrafast lasers", Review of Scientific Instruments 69, 1207–1223 (1998).
- <sup>91</sup>S. Bock, F. M. Herrmann, T. Püschel, U. Helbig, R. Gebhardt, J. J. Lötfering, R. Pausch, K. Zeil, T. Ziegler, A. Irman, T. Oksenhendler, A. Kon, M. Nishuishi, H. Kiriyama, K. Kondo, T. Toncian, and U. Schramm, "Characterization of Accumulated B-Integral of Regenerative Amplifier Based CPA Systems", en, Crystals 10, Number: 9 Publisher: Multidisciplinary Digital Publishing Institute, 847 (2020).
- $^{92}\mathrm{D.~R.~Paschotta},\,B\,\mathit{Integral},\,\mathrm{en}.$
- <sup>93</sup>T. R. Ensley and N. K. Bambha, "Ultrafast nonlinear refraction measurements of infrared transmitting materials in the mid-wave infrared", EN, Optics Express 27, Publisher: Optica Publishing Group, 37940–37951 (2019).
- <sup>94</sup>P. A. Carpeggiani, G. Coccia, G. Fan, E. Kaksis, A. Puglys, A. Baltuka, R. Piccoli, Y.-G. Jeong, A. Rovere, R. Morandotti, L. Razzari, B. E. Schmidt, A. A. Voronin, and A. M. Zheltikov, "Extreme Raman red shift: ultrafast multimode nonlinear space-time dynamics, pulse compression, and broadly tunable frequency conversion", EN, Optica 7, Publisher: Optica Publishing Group, 1349–1354 (2020).
- $^{95}$  acA2000-165um | Basler Product Documentation.
- <sup>96</sup>M. B. Reid, "Electron beam emittance growth in thin foils: A betatron function analysis", Journal of Applied Physics **70**, 7185–7187 (1991).

- <sup>97</sup>C. Berger, S. Barber, F. Isono, K. Jensen, J. Natal, A. Gonsalves, and J. van Tilborg, "Active nonperturbative stabilization of the laser-plasma-accelerated electron beam source", Physical Review Accelerators and Beams 26, Publisher: American Physical Society, 032801 (2023).
- <sup>98</sup>F. Kohrell, S. K. Barber, C. E. Doss, K. Jensen, C. Berger, S. Schröder, Z. Eisentraut, K. Nakamura, A. J. Gonsalves, F. Isono, G. R. Plateau, R. A. Van Mourik, M. Gracia-Linares, L. Labun, B. M. Hegelich, S. V. Milton, C. G. R. Geddes, J. Osterhoff, E. H. Esarey, C. B. Schroeder, F. Grüner, and J. van Tilborg, "Over 8 hours of continuous operation of a free-electron laser driven by a laser-plasma accelerator", Physical Review Accelerators and Beams (submitted), (submitted) (2025).
- <sup>99</sup>E. Saldin, E. Schneidmiller, and M. Yurkov, "Statistical properties of the radiation from sase fel operating in the linear regime", Nucl. Instrum. Methods Phys. Res., Sect. A 407, 291–295 (1998).
- <sup>100</sup>P. Schmüser, M. Dohlus, J. Rossbach, and C. Behrens, Free-electron lasers in the ultraviolet and X-ray regime: Physical principles, experimental results, technical realization; 2nd ed. Vol. 258, Springer tracts in modern physics (Springer, Cham, 2014), 231 pages.
- <sup>101</sup>K. Jensen, N. Cook, J. Einstein-Curtis, C. Doss, F. Kohrell, C. Berger, S. Coleman, J. Edelen, S. K. Barber, A. J. Gonsalves, and J. van Tilborg, "Longitudinal focal stabilization", in preparation (2024).

## 10 Appendix

HTGs, Procedures that I wrote (documenting the path to turn-key operation) TAU BELLA reports (after removing all sensitive information, to document monthly progress) In-depths analysis of the polynomial fit optimization for FROG traces (in case that gets too detailed for the main chapter)

### 10.1 GRENOUILLE Diagnostic: Linear Chirp Retrieval

Continuing the discussion from Sec.5.2.5, Fig.51 studies the impact of changing the spectral amplitude threshold (SAT) value on the  $\bar{\beta}$  retrieval. For the retrieval, three fits of different polynomial order are used to approximate the spectral phase of the laser pulse in a wavelength interval defined by the SAT.

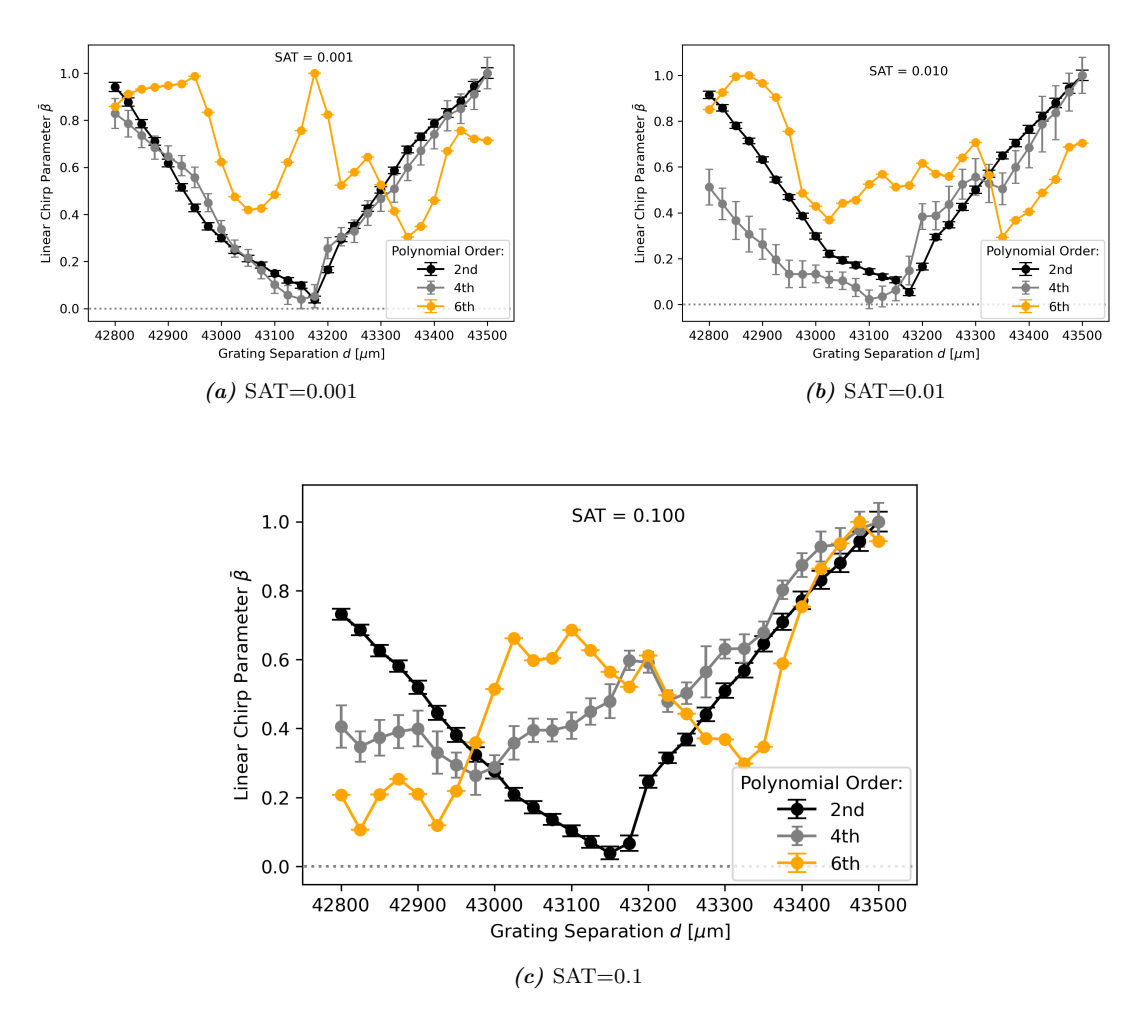


Figure 51: Change in normalized, absolute linear chirp parameter  $\bar{\beta}$  of the low power laser pulse with the compressor grating separation d. Polynomial fits of three different orders were used to extract the  $\bar{\beta}$  from the spectral phase, and the behavior of the chirp parameters of different origin are being compared. The spectral phase traces fitted were retrieved from SHG FROG images taken on the HTU GRENOUILLE diagnostic line. The spectral amplitude threshold (SAT) value was changed to study its effect on the accuracy of the  $\bar{\beta}$  retrieval, depending on the polynomial fit order.

#### 10 Appendix

As can be seen when comparing Fig.51(a),(b) and (c), the trend of  $\bar{\beta}$  values from the 2<sup>nd</sup> order polynomial fit show only a weak dependence when changing the SAT value. The absolute linear trend seems almost unaffected, showing an intersection with the x-axis (grating position of ideal compression  $d_0$ , for which  $\bar{\beta}(d_0) = 0$ ) of close to  $d_0 = 43\,150\,\mu\text{m}$  in all three cases.

The behavior of  $\bar{\beta}$  from the 4<sup>th</sup> order polynomial fit is much more sensitive, showing an increasing deviation from the expected trend with higher SAT values. A noticeable change can be observed when going from SAT = 0.001 to 0.01, and in the case of SAT = 0.1, the trend does not resemble an absolute linear trend at all.

For the 4<sup>th</sup> order, no clear evaluation of the dependence between the  $\bar{\beta}$  trend and SAT value is possible. Even at the smallest SAT value, it does not show any similarities to the expected relation. And even though it is significantly affected when further increasing the SAT value, no reasonable statement can be made if that is increasing or further decreasing the deviation from the expected trend.

#### 10.2 HTU System Operation Procedures ("How-to Guides")

## **How to: HTU Laser Startup**

Purpose: Record of current general startup procedure.

Area used: Rm 148

#### A) Vitara/Legend (aka, "frontend", "regen") Startup Procedure

- 1. Arm interlock on the inside of 148 next to the door
- 2. In HTW utilities room (aka 148B, "chiller room", "power supply room"), turn on HTU revolution chiller (middle right, labeled "HTU REVO LEGEND")
- 3. Turn keys on Vitara and right revolution power supply box on the rack above amp table
  - a. Vitara power supply is labeled "Verdi"
- 4. Turn on pockel cell, dial to 8.5 kV
- 5. Check that the Legend Beam Dump is flipped up
- 6. Use laser PC, remote desktop to 192.168.6.71 (using LOASIS\loasis account) for laser software (shortcuts on desktop)
  - a. VITARA
    - i. Start labview software
    - ii. Hit REMOTE
    - iii. DIODE ON
    - iv. Wait for modelocking
  - b. SDG
    - i. Start labview software using desktop shortcut
    - ii. Note, need to select com port manually (com5) and baud rate to 19200
    - iii. After Vitara is started, click "reset" button on "channel delays" tab (can also manually press reset button on SDG box)
  - c. REVOLUTION
    - i. Reset timing box if not already done above (software or on the SDG elite in the
    - ii. Start labview software "Revo 1.0 Legend". Note, Legend revolution is on comport 4.
    - iii. Click "evolution settings" to display settings
    - iv. Under SYSTEMS tab, make sure to switch Q-switch mode to EXTERNAL
    - v. Before starting revolution, ensure Legend beam dump inserted.
    - vi. Hold RUN button until you hear loud beeping noise
    - vii. When power stabilizes on analog power meter, can remove Legend beam dump. If everything is functioning well, this should occur in ~1 min.
- 7. Check the power meter next to Legend box and take notes in "Vitara-RevolutionLOG.txt" file about the performance

#### **B) GAIA Startup Procedure**

1. Arm interlock on the inside of 148 next to the door

#### 10 Appendix

- 2. In HTW utilities room (aka 148B, "chiller room", "power supply room"), enable key switch on GAIA controller, turn on all power supplies in power supply rack
- 3. Start Gaia software (on desktop to of 192.168.6.71). If it software displays faults, click "reset"
- 4. If all faults are cleared, click "start". Verify software indicator switches to "lasing".
- 5. Allow lamps to flash for ~1hr before next steps
- 6. After lamp warmup, enable pockels cell q-switch for both lines, wait 2 mins.
- 7. Verify GAIA PPS shutters and 1Wire Gaia shutters are all inserted
- 8. Before sending gaia beam to amplifier table, send beam to 1Wire Gaia shutters for 1 min by opening gaia internal shutters.

#### C) Summarize the most critical 'DO'-s and 'DO-NOT's

#### DO-s:

- 1. Make sure low power shutter is closed (on touchscreen box in the rack)
- 2. If VITARA or REVOLUTION wont turn on, check chillers, interlock and shutters
- 3. Always wear goggles and be especially careful when flipping up/down the mirror directing the pulsed beam onto the powerhead, your hand might be in the beampath!

#### DONT-s:

1. Never change any of the current or voltage settings for any of the lasers. If the lasers wont start, contact Art or Joe

==========

#### Version History:

version #	date	writer(s)/contributor(s)	notes
01	01/18/2023	Finn Kohrell	Original issue

# How to: HTU Daily Procedure (Startup, Alignment, Shut-Down)

Purpose: Record of current general alignment procedure.

Precedents: laser start up Area used: Rm 148, B-cave

#### A) See 'startup procedure'

#### **B)** Laser preparation

- 1. Check that Amp4 dump is INSERTED
- 2. Enable and open low power shutter (in)

  Location: touchscreen on box in the rack, under SDG elite
- 3. Enable and open high power shutter (out)

  Location: touchscreen on box in the rack, under SDG elite
- 4. Check that flip mirror is down, so that beam will be sent to the stretcher

DETERMINE which set of GEECS devices needed for planned operations and ensure they are on. For basic laser operations (no e-beams planned), using the groups "HTULaserCams" and "HTUAuxiliaryHardware"

#### ONLY REQUIRED ROUGHLY ONCE PER MONTH

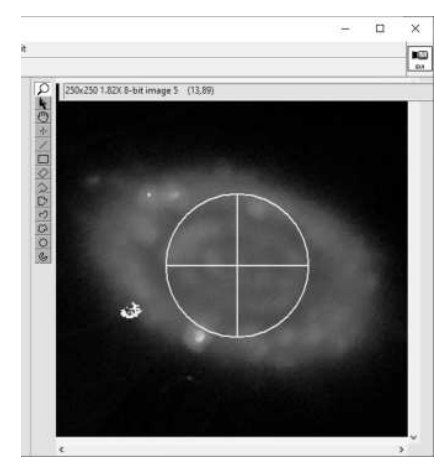
## B) Blue diode alignment (Check Target chamber references correspond to straight line through undulator)

- 5. Turn on the blue diode laser
  - Location: B-cave by first turbo pump of compressor chamber
- 6. Send camera presets for diode operation (HTU\_148DiodeAlignment)
- 7. Steer blue beam onto Visa1 and Visa8 (or Visa2 and Visa7), use "big blu" references
  - a. If Visa1 is not roi'd, use the right of the two screens
  - b. U BlueDiodePicos for the picomotor controller
  - c. Position.Axis 1 and 2 correspond to X and Y for first mirror, use for Visa1 (or Visa2) alignment
  - d. Position.Axis 3 and 4 correspond to X and Y for second mirror, use for Visa 8 (or Visa7) alignment
- 8. Move in Modelmager wedge
- 9. Use the U\_TCAlignStages device to move in "Target Out" stage (73mm). Look at

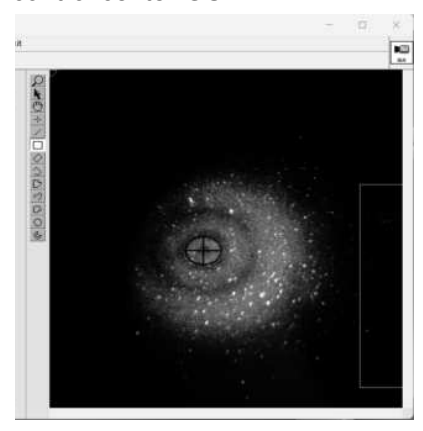
- UC\_TC\_Output to update blue beam crosshair position
- 10. Move "Target In" stage from 0 to 73mm and update blue beam reference position
- 11. Remove both "Target In" and "Target Out" stages (from 75 back to 0mm)
- 12. Set mode imager position in control center to focus of pulsed beam, near "-24"
- 13. update virtual crosshair position on MI such that it correctly represents master axis
- 14. leave MI wedge inserted to avoid losing reference (non-repeatable due to plunger inaccuracy)
- 15. Turn off the blue diode laser

#### E) Pulsed beam alignment

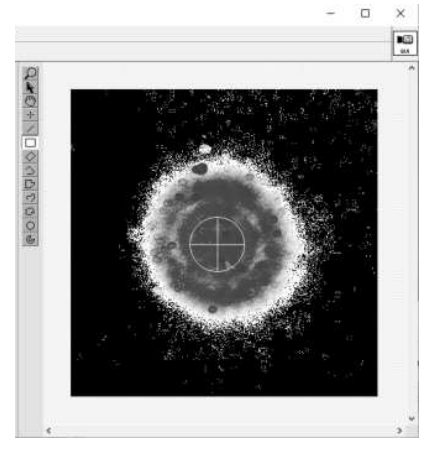
- 16. Check that Amp 4 dump and MI wedge are inserted. (Extra Flippers panel of Control Center)
- 17. Send presets for HTU\_PulsedAlignmentAmpTableOnly in MC
- 18. Open GUI\_HTU\_MutliCamAplifiers
- 19. Open front end (low power) and high power shutter and send the beam to amplifier table by flipping down the mirror that directs pulsed beam onto powerhead
- 20. Run stretcher exit Aligna (from computer 6.93, located by stretcher)
- 21. Run HTU\_diode\_alignment GUI
  - a. Load HTU stretcher out.cfg in Beampointing.vi
  - b. Suggested settings:
    - i. Update speed: 1000 ms
    - ii. img to avg: 5 for initial startup to get coarse alignment
  - c. Set to 'Align' mode and enable feedback
  - d. Once aligned, disable feedback, change to 'Stabilize' mode
    - change update speed to 2000ms
    - ii. enable feedback.
  - e. Leave running.
- 22. MRC setup see procedure here
  - a. Turn MRC trigger on, wait a few seconds, turn back off
- 23. Send presets for HTU PulsedAlignment148PlusBCave
- 24. Close Iris after amp4 output periscope
- 25. Open Amp4 dump
- 26. Check **UC\_TubeIn** and steer beam to irised pulse reference using TubeIn mirror in control center GUI



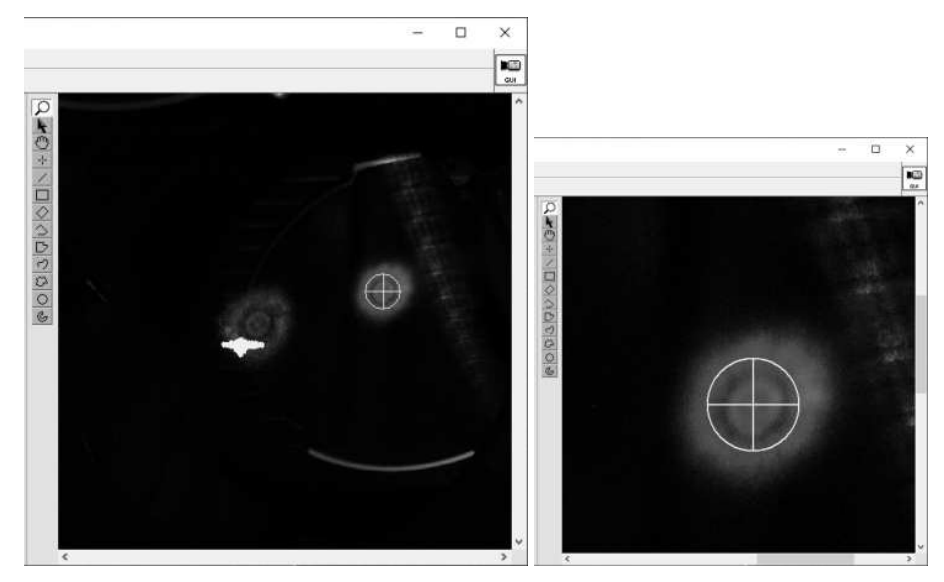
27. Check **UC\_GratingMode** and steer beam to irised pulse reference using Compln mirror in control center GUI



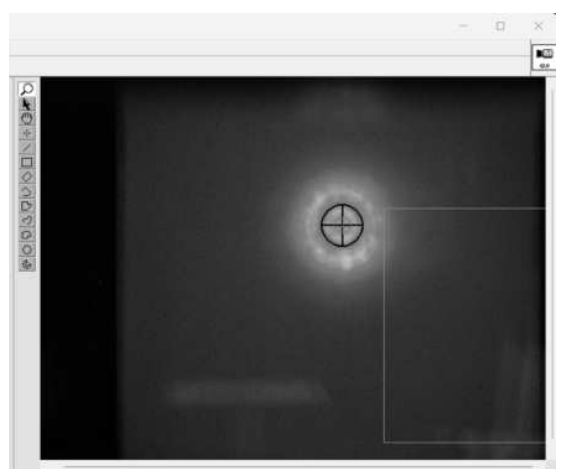
28. Check **UC\_DMSurface** and steer beam to irised pulse reference using DM Surface mirror in control center GUI



29. Check **UC\_OPAIn1** and steer beam to irised pulse reference using OAPIn1 mirror in control center GUI



30. Check **UC\_OPAIn2** and steer beam to irised pulse reference using OAPIn2 mirror in control center GUI



- 31. Close Amp4 dump and open Iris back up
- 32. Send beam to the TC, use U\_TC In Stage (Step No.9,10) to align pulsed beam to **blue beam** reference on TC\_Input, using BeamlineIn mirror, and to TC exit by centering the halo on TC\_Output using BeamlineOut mirror, in control center GUI
- 33. remove both TC stages and check the MI camera update reference crosshair to current beam position (only necessary if significantly off)
- 34. From the control room, pull up a beampointing.vi GUI, load the HTU-TC\_Focus configuration
- 35. Update the alignment target crosshair to the current beam position (check if both motors say "No Move required") and update default in master control. Now this can be used to stabilize beam on target against longterm drift

#### F) Shutdown

- 36. Turn off stabilization
  - a. Aligna (8.207), RegOn = False
  - b. Blue beam off
  - c. Feedback off in beampointing.vi
  - d. Aigna (rm 148), RegOn = False
- 37. Insert amplifier dump (HTU CC)
- 38. Turn off (out) all valves in HTU CC
- 39. Insert all GAIA flippers
- 40. Insert high & low power shutters
- 41. Insert Regen powermeter mirror

  Note: will be permanently up in near future
- 42. Disable high & low power shutters (HMI in laser bay)
- 43. Stop Revolution (GUI)
- 44. Vitara diode off, and "local"
- 45. Turn key switches off for the Revo, and the Verdi (Vitara)
- 46. Power off GAIA power supplies and turn key switch off
- 47. Turn off Revo Legend chiller off
- 48. Turn off interlock

#### G) Summarize the most critical 'DO'-s and 'DO-NOT's

#### DO-s:

- 1. Double check camera presets.
- 2. Always be aware of where you are blocking and/or sending the laser. Especially the pulsed beam.

=========

### Version History:

version #	date	writer(s)/contributor(s)	notes	
01	12/20/2022	Kyle Jensen	Original issue	
02	01/18/2023	Finn Kohrell	Updated after detailed walkthrough	
03	03/01/2023	Finn Kohrell	Updated alignment procedure	

#### 10 Appendix

04	03/05/2023	Guillaume Plateau	Updated sections B, C, D. Added shutdown procedure (E)	
05	03/06/2023	Finn Kohrell	Added Laser Startup, change to "Daily Procedure"	
06	01/11/2024	Curtis, Finn,Kyle, Chris	Complete overhaul, up-to-date after long downtime	
07	04/04/2024	Finn Kohrell	removed IR diode, since it has been decommissioned, and updated pulsed beam procedure	
08	09/18/2024	Finn Kohrell	update TC alignment procedure	

## **How to: Amplifier Table Alignment + MRC**

Purpose: Record of current amplifier table alignment after extensive laser work

with Bob in 07/2023

Precedents: daily alignment procedure

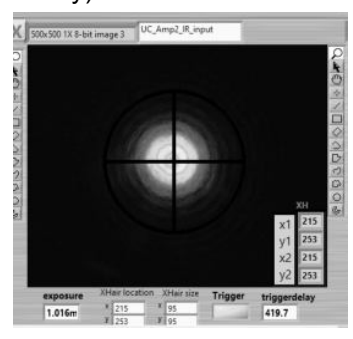
Area used: Rm 148

!!!LOOK!!! BEFORE ADJUSTING ANYTHING IN THE AMPLIFIER TABLE THAT WOULD RESULT IN NEW MRC SET POINTS, YOU MUST <u>Turn MRC</u> off, MRC trigger ON. IF YOU DO NOT, YOU WILL NEED TO REPEAT YOUR MANUAL ALIGNMENT BEFORE MOVING ON TO THE MRC SET UP GUIDE.

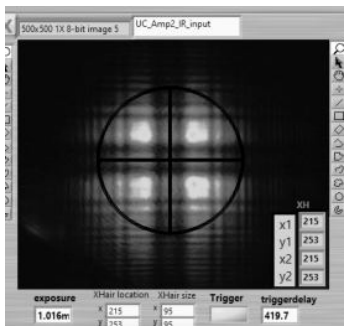
## A) Documentation of all physical alignment targets and their respective camera references

#### Amp2\_In:

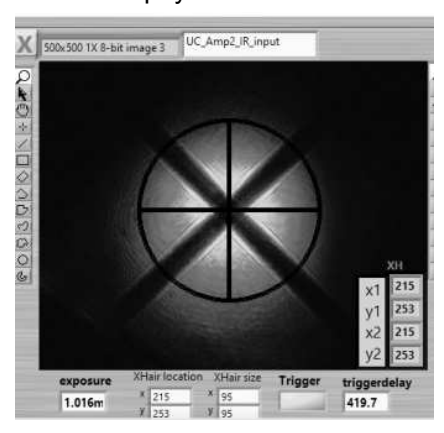
 First pinhole I1 Symmetrize the iris. handled by beam pointing gui and aligna (in theory)



o first crosshair: C1 handled by beam pointing gui and aligna (in theory)



• **Amp2 C1** look at Amp2 ir input for alignment. Adjust using Amp2 M1 Overlap the virtual and physical crosshair.



**Amp2 C2**: No camera reference. Instead, stick red ir paper after and adjust alignment using Amp2 M2

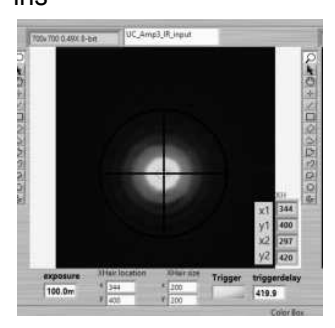
**Amp2 C3**: No camera reference. Instead, stick red ir paper after and adjust alignment using Amp2 M3

**Amp2 C4**: No camera reference. Instead, stick red ir paper after and adjust alignment using Amp2 M4

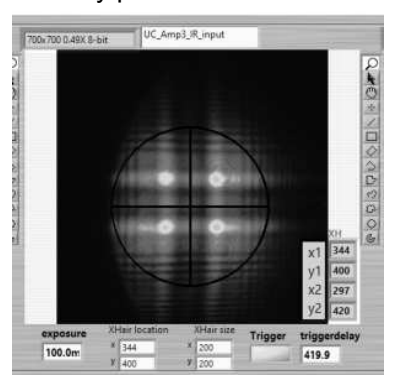
#### • Amp3\_In:



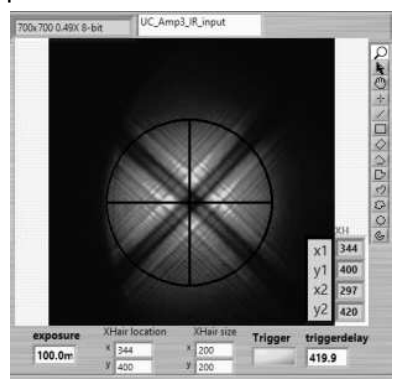
 Amp3 I2 look at Amp3 ir input for alignment. Adjust using Amp 2 M5. Symmetrize the iris



 Amp3 C1 look at Amp3 ir input for alignment. Adjust using Amp 3 M0 Center the Intensity profile



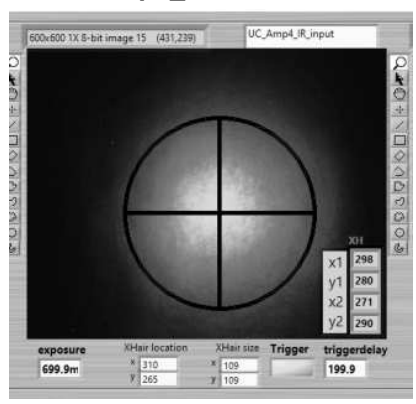
 Amp3 C2 look at Amp3 ir input for alignment. Adjust using MRC2 Center the Intensity profile



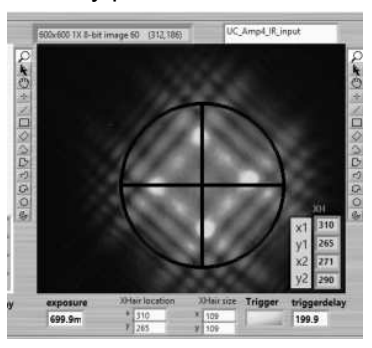
 Amp3 C3 look at Amp3 ir input for alignment. Adjust using Amp3 M1 Overlap the virtual and physical crosshair



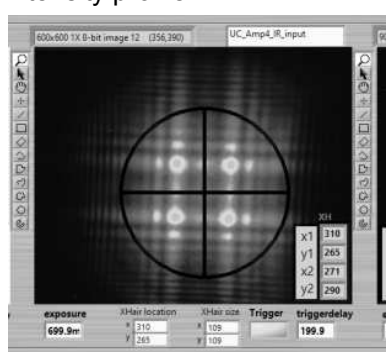
• Amp4\_In:



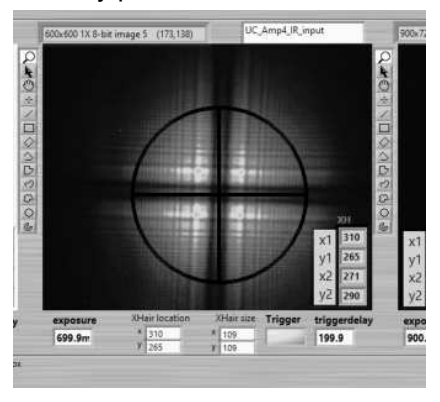
 Amp3 C4 look at Amp4 ir input for alignment. Adjust using Amp3 M2 Center the Intensity profile



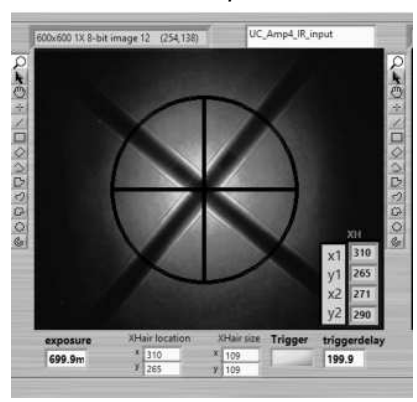
 Amp3 C5 look at Amp4 ir input for alignment. Adjust using Amp3 M3 Center the Intensity profile



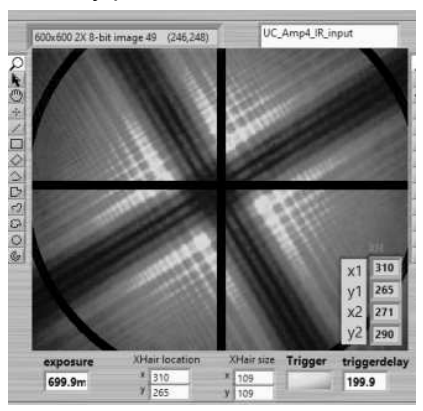
 Amp3 C6 look at Amp4 ir input for alignment. Adjust using Amp3 M4 Center the Intensity profile



 Amp3 C7 look at Amp4 ir input for alignment. Adjust using Amp3 M5. Overlap the virtual and physical crosshair. Note:(this should probably be "center intensity pattern" rather than "overlap crosshairs", 2/3/25)

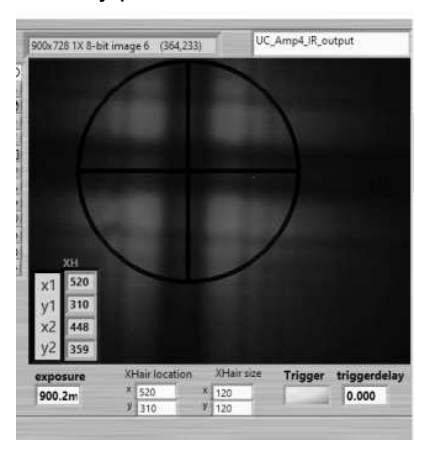


 Amp4 C1 look at Amp4 ir input for alignment. Adjust using Amp4 M1. Center the Intensity profile

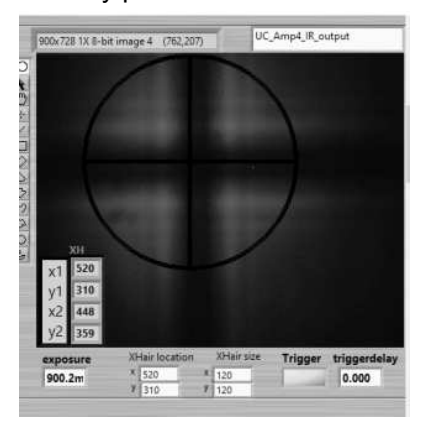


#### Amp4\_Out:

 Amp4 C2 look at Amp4 ir output for alignment. Adjust using Amp4 M2. Center the intensity profile



 Amp4 C3 look at Amp4 ir output for alignment. Adjust using Amp4 M3. Center the intensity profile.



Step-by-Step instructions to MRC setup:

1. Turn MRC off, MRC trigger ON

- 2. make sure alignment on the amplifier table is at the desired positions
- close lids on amp table AND MAKE SURE ALL CROSSHAIRS AND IRISES ARE FLIPPED DOWN!
- 4. open PARAMETERS tab on MRC software, set detector type to PSD and hit REFRESH

#### 10 Appendix

- 5. Hit SET on Stage1 (this will automatically refresh voltage values on stage2, dont worry about that).
- 6. Make sure the P-Factor for Stage 1 doesnt automatically get set to 0.01. If it does, change to 3.5 and hit apply
- 7. Hit SET on Stage 2
- 8. Now check the beam position on your virtual crosshairs. If its visibly off, you want to change the adjust-In values. In the process of setting the new set&hold it will automatically set the adjust in vales. make sure SOFTWARE is selected for both P-factor as well as ADJUST-IN values on both STAGE1 and 2.
- 9. With the stabilization and MRC trigger ON, slightly **change one value at a time** (stepsize <0.1) and hit apply after each change.
- 10. Once you are happy with the virtual crosshair overlap, turn MRC trigger OFF
- 11. now you can flip in physical crosshairs and check position on the cameras, just **make sure to** flip them down before turning MRC trigger back ON
- 12. iterations of this (trigger off, check position on physical crosshair, flip down, trigger On, slight tweak to Adjust-In, repeat) until youre satisfied
- 13. Leave stabilization on and always make sure to practice good trigger discipline

#### G) Summarize the most critical 'DO'-s and 'DO-NOT's

#### DO-s:

1. Make sure to look at the right camera for a given crosshair

#### DO NOT:

- 1. leave the MRC trigger ON while performing any work on the amp table, even if its just checking a reference downstream from it. PSDs are super sensitive to stray light!
- 2. change any of the virtual or physical crosshair locations!

=========

#### Version History:

version #	date	writer(s)/contributor(s)	notes
01	31/07/2023	Finn Kohrell	Original issue

# How to pump down the entire HTU vacuum line incl. VISA undulator

Purpose: This guide is providing step-by-step instructions on how to walk through the entire process, to learn operating it and avoid mistakes Area used: 148. B- and A-cave

#### A) Preparing for roughing

- 1. Start in 148 and work your way downstream into B-cave, make sure all:
  - 1.1. Parts of the system are at atmospheric pressure
  - 1.2. turbos are turned off and spun down
  - 1.3. Gates to the turbos are **CLOSED**
  - 1.4. Roughing pumps are off
  - 1.5. Venting ports are closed
  - 1.6. Roughing lines are **OPEN**
- 2. Go to A-cave, make sure that
  - 2.1. everything is at atmospheric pressure
  - 2.2. venting ports are closed
  - 2.3. Turbos are off and spun down
  - 2.4. Roughing lines are **CLOSED**
  - 2.5. Backing lines are **OPEN**
  - 2.6. Check pump station outside to make sure the clamp connecting both roughing pums is ON (meaning the lines are combined) before turning roughing pumps on (the two pumps outside A-cave are only used to back the turbos in A-cave, roughing the undulator will be done using the roughing pumps in B-cave!)
- 3. Back to 148 and B-cave
  - 3.1. Now that all parts of the system are under atmosphere, vents and gates to turbos closed and roughing lines open (with pumps still off), we can connect all the chambers and the undulator by opening the respective gates
  - 3.2. Double-check that all turbos and the roughing pumps are off, then put on clamp to combine both roughing lines
  - 3.3. Now you can spin up both roughings, they are now evacuating the entire vacuum system all the way from the beam tube in 148 to the undulator, so

- it will take a while for them to spin up and pump down
- 3.4. Meanwhile, because the clamp is on, they will also back the turbos in 148 and B-cave and the turbos in A-cave are backed by their roughing line (double-check that all backing-switches are OPEN)
- 3.5. You can start to spin up the turbos while chambers are being pumped down by roughing, they are backed and the gates to the chambers still closed
- 4. When pressure of entire system reaches 10^-2 Torr regime
  - 4.1. Start in 148 and work your way downstream, close all roughing ports (to make sure turbos will not fight against roughing pumps). This is only necessary in 148 and B-cave, because the A-cave roughing pumps have only been used to back their turbos
  - 4.2. Make sure turbos are fully spun up and the current is below 1A (this means they are not still fighting against pressure in the backing line, which we want to make sure before opening gates to chambers)
  - 4.3. Now open gate valves to turbo pumps (turbos are pumping down vacuum system, roughing pumps are only used to back the turbos and keep the roughing line evacuated)
  - 4.4. Go to A-cave and open gates to turbos as well
- 5. This concludes the pump-down procedure

#### B) Most critical 'DO'-s and 'DO-NOT's

#### DO-s:

- 1. Make sure all venting ports are CLOSED
- 2. Always work your way through the entire system, 148 to A-cave
- 3. Before venting a part of the system, always make sure the turbos are protected (either turned off or backed and backing+roughing line separated by taking off clamp)

#### DO NOT-s:

- 1. NEVER open gate between chamber and running turbo if turbo isnt fully spun up or current still over 1A
- 2. Don't turn on turbos without double-checking that they are backed by running roughing lines and gates to chamber are closed

#### 10 Appendix

## Version History:

version #	date	writer(s)/contributor(s)	notes
01	12/01/2022	Finn Kohrell	Original issue

## Training History (if applicable):

name	status	date	notes
Tyler	Trainer	12/01/2022	Gave us the detailed walk-through of the entire procedure
Kyle, Finn	Were instructed by Tyler	12/01/2022	

## Eidesstattliche Erklärung / Declaration on Oath

Hiermit versichere ich an Eides statt, die vorliegende Dissertationsschrift selbst verfasst und keine anderen als die angegebenen Hilfsmittel und Quellen benutzt zu haben. Sofern im Zuge der Erstellung der vorliegenden Dissertationsschrift generative Künstliche Intelligenz (gKI) basierte elektronische Hilfsmittel verwendet wurden, versichere ich, dass meine eigene Leistung im Vordergrund stand und dass eine vollständige Dokumentation aller verwendeten Hilfsmittel gemäss der Guten wissenschaftlichen Praxis vorliegt. Ich trage die Verantwortung für eventuell durch die gKI generierte fehlerhafte oder verzerrte Inhalte, fehlerhafte Referenzen, Verstösse gegen das Datenschutz- und Urheberrecht oder Plagiate.

I hereby declare that the presented thesis was written autonomously and only under usage of the mentioned sources and tools. Wherever generative artificial intelligence (AI) was used as a part of the process of compiling this thesis, I affirm that my own accomplishments stand at the center of the work, and that all tools used are documented following good scientific practice. I am responsible for potentially incorrect contents, faulty references, violations of copyright, or plagiarism generated by the AI.

Ort und Datum (Location and Date)

Unterschrift (Signature)